Master of Science Thesis

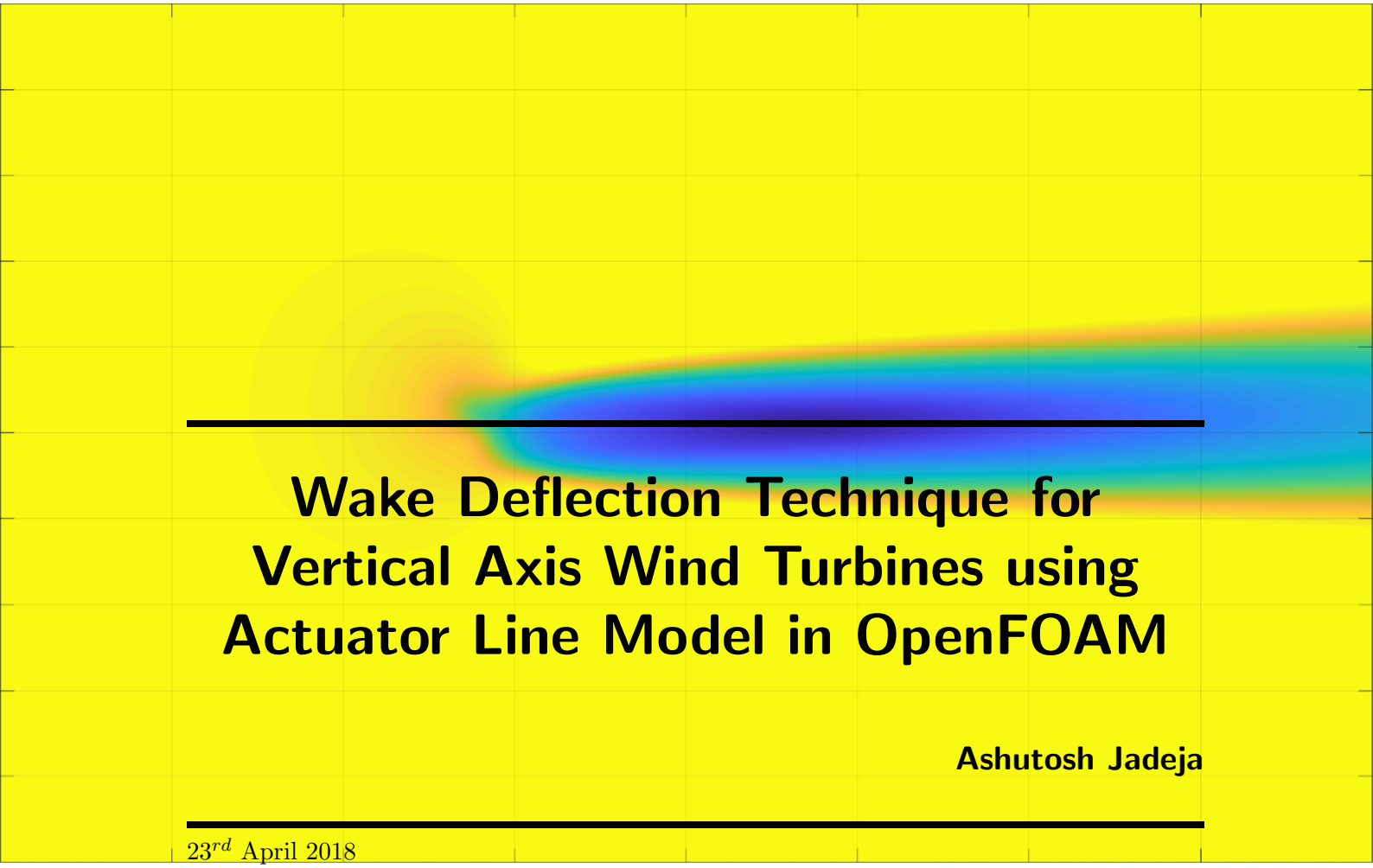

Wake Deflection Technique for Vertical Axis Wind Turbines using Actuator Line Model in OpenFOAM

Ashutosh Jadeja

23^{rd} April 2018

Aerodynamics

TU Delft

Faculty of Aerospace Engineering

Delft University of Technology

Wake Deflection Technique for Vertical Axis Wind Turbines using Actuator Line Model in OpenFOAM

Master of Science Thesis

For obtaining the degree of Master of Science in Aerospace Engineering
at Delft University of Technology

Ashutosh Jadeja

23^{rd} April 2018

Faculty of Aerospace Engineering · Delft University of Technology

Delft University of Technology

DELFT UNIVERSITY OF TECHNOLOGY
DEPARTMENT OF AERODYNAMICS

The undersigned hereby certify that they have read and recommend to the Faculty of Aerospace Engineering for acceptance the thesis entitled **"Wake Deflection Technique for Vertical Axis Wind Turbines using Actuator Line Model in OpenFOAM"** by **Ashutosh Jadeja** in fulfillment of the requirements for the degree of **Master of Science**.

Dated: 23^{rd} April 2018

Supervisors:

Dr. Ir. C. J. Ferriera

Ir. T. J. Berdowski

Ir. V. Mendoza

Committee:

Prof. Dr. Ir. L. L. M. Veldhuis

Dr. Ir. A. H. van Zuijlen

Prof. Dr. Anders Goude

Acknowledgements

As this chapter comes to an end, I would like to acknowledge a few from the many without whose encouragement and support, this journey would hot have be as special and memorable. Firstly, I would like to convey my deepest gratitude to my brother and my parents for motivating me to follow my dreams despite of all the tantrums that I could throw at them for a quarter of a century (and forth...).

I would like to express my gratitude to Dr. Carlos for giving me the opportunity to work on this project and for guiding me at every step of the way. In fact, I have grown so attached to this topic that I still have a couple of simulations running with varying parameters. I would also like to thank Victor and Tom for their continuous guidance and for their help with every small issue that I faced with my thesis. I would like to especially thank them for tolerating about 100 pages of bad grammar in my report.

I would like to convey a special thanks to Dr. Goude, whose inputs helped me identify the source of the problems in the model, and for his contribution in correcting the same in short notice.

Having pursued Mechanical Engineering in my Bachelor's programme, a Master's programme in Aerospace Engineering was a little hard to keep up to. If not for Oriol, Anna, and Marc, who had the patience, and were kind enough to help me with the basics of aerodynamics and mathematics, this day would never have arrived.

I would like to thank Andi, Cantika, and Raunak for adopting me and for matching my level of insane. The last two years would not have been remotely as fun without them. Last but not the least, I would like to thank Aarav and Gerson for their continuous support through the last 7 years, to them I say, "We're Engineers, finally!".

Table of Contents

List of Figures

List of Tables

Chapter 1

Introduction

Since the increase in demand for renewable energy infrastructure, the wind energy sector has had its share of up-scaling the energy output. This is primarily done by installing offshore wind farms, which are arrays of wind farms with a certain distance between them. Wind farms are densely spaced due to available floor area and cost constraints. Having a densely spaced wind farm creates close interaction between wind turbines and wakes. The upstream turbines experience a clean and free flow, however, as the turbine extracts kinetic energy from the wind and leaves a turbulent wake, the inflow for the subsequent turbine has a flow deficient in kinetic energy. It has been observed that the downstream wind turbines, which do not receive an undisturbed flow, often underperform compared to their rated power output. As the spacing between the turbines cannot be increased due to limited floor area and cost constraints, one of the ways to optimise the wind farm power output is by actively optimising a compromise in the power extracted from each turbine to have a minimal effect on the subsequent turbines. There are two approaches to this problem, the first one is to reduce the power extracted from the upwind wind turbine to reduce the velocity deficit for the subsequent downstream turbines, and the second solution is to deflect the wake away from the downstream turbines. The methods for wake deflection already exist for Horizontal Axis Wind Turbines (HAWT) and are also discussed in this report, however, with the increasing popularity of the Vertical Axis Wind Turbines (VAWT), a similar technique is required to address the issue of reduced power performance of the downstream turbines. This report discusses the basic aerodynamics of the HAWTs and the VAWTs, and the yawed configuration for a HAWT by which the wake is deflected. The guiding principle behind wake deflection is then tested for a VAWT using the Actuator Line Model.

1.1 Document Structure

This report is structured to give the reader a systematic approach to understanding the scope, methodology and the results of the thesis. Chapter 1 provides a brief introduction into the

wind energy sector in general as well as the scope of this thesis. The research objectives and questions are clearly defined in the section 1.2. Section 2 gives an insight into the workings of the wind turbines. In the section 2.1, the working of the HAWT is discussed as well as the wake properties in different yaw configurations of the turbine. Section 2.3 discusses the working and the aerodynamics of the VAWT.

Section 3 deals with various flow and the rotor modelling techniques. Chapter 4 provides the results and the work done in the scope of this thesis. First, the simulation setup is described. Next, the results from the turbinesFoam simulation are compared to other models and the reason for the deviation of the results is discussed. Once the limitations of the model are acknowledged, the focus is then set on the definition of wake deflection. A reference case for wake deflection is simulated. The simulation results for wake deflection cases using fixed blade pitch angles are then presented and compared to those from the reference case. Then the results from the simulation with active pitch control are discussed. Finally, the conclusions are drawn and the answers to the research questions are summarized in Chapter 5.

1.2 Objective and Hypothesis

The wake deflections have shown a promising advantage for wind farm applications. In the case of a HAWT, the wake deflection occurs due to the deflection of the thrust vector when the turbine is in yawed configuration. Hypothesis: The basic principle behind the wake deflection in a HAWT, the deflection of the thrust vector on turbine blades, is the same principle that will guide the wake deflection in a VAWT.

Questions that are needed to be addressed are:

1. What is the relation between the wake deflection and its corresponding blade loading in a VAWT?
    - How does the blade loading asymmetry behave due to the cyclic loading nature for VAWTs?
    - How does active pitch control of the blades impact the required asymmetric loading in the cross flow direction and thrust vector deflection?
2. How does wake deflection in a VAWT affect its power and thrust coefficient?
    - As the VAWT is omnidirectional, will the prescribed asymmetry in loading create a deficiency in the performance of the turbine?
3. How do the wake deflection characteristics in a HAWT compare to those of a VAWT?
    - What is the relation between the pitch and yaw angles of the corresponding turbines to their wake deflection?
    - How does the blade loading on a VAWT compare to that of a HAWT in the case of wake deflection?

The following section discusses the aerodynamics of wind turbines and their wake properties which should help the reader get an insight into the behaviour of the wake of wind turbines.

Chapter 2

Wind Turbines

The main purpose of wind turbines is to convert the wind's kinetic energy into useful electrical energy (Micallef, 2015). The blades of the wind turbine have a cross-section of an aerofoil. When wind flows through the blades, the aerofoil generates lift and drag. These forces drive the rotation of the turbine and extract kinetic energy from the flow.

The maximum aerodynamic power that can be extracted from a HAWT is approximately 59% of the net energy in the flow and is derived by Albert Betz (Betz, 1919). This is called the Betz limit. This optimum value, however, is not achieved in the real world scenario due to various factors such as non-uniform inflow condition due to turbulence, mechanical limitations, and so on. The aerodynamics power extracted from the wind is calculated by,

$$P = \frac{1}{2}\rho A U_\infty^3 C_P \tag{2.1}$$

where, A is the area swept by the rotor, ρ is the density of the wind, U_∞ is the free stream velocity of the flow, and C_P is the power conversion efficiency or coefficient of power. It is seen that the power extracted from the wind is proportional to U_∞^3. If there is a velocity deficit in the inflow of the turbine, the power extracted from the turbine would be reduced. The velocity deficit in question is caused by the wake of the upstream turbine. It is, therefore, important to minimize the effect of velocity deficit in the wake of the upstream turbine on the downstream turbine. One of the methods adopted to do so is by deflecting the wake. To control the behaviour of the turbine wake, first, the basics of aerodynamics involved, and the related mathematical models must be understood.

2.1 Horizontal Axis Wind Turbines

In this section, the aerodynamics of the flow across the wind turbine and the characteristic flow properties in its wake are reviewed. Horizontal wind turbines have been prevalent in

Figure 2.1: Spiral tip vortex line in the wake of a HAWT (Hand et al., 2001).

the wind energy sector due to their relatively simpler aerodynamics when compared to the vertical axis wind turbines, and the available research, which has helped in improving their performance over the years. The basic aerodynamics of the HAWT are classified into the inflow, power extraction by the turbine, and the wake. The inflow conditions depend on the terrain, position of the turbine in the wind farm and several other factors. The power extracted by the turbine is dependent on the dynamic characteristics of the aerofoil, blade geometry (twist, chord, and span), relative heading of the turbine with respect to the flow vector, and more importantly, the magnitude of wind velocity.

As the main point of discussion in this study is the control of wake behaviour, it is crucial to gain a better understanding of this topic. The wind turbines are designed to extract power from the kinetic energy of the wind. This results in the downstream flow to have considerably lower kinetic energy than the upstream region. The drop in velocity results in an increase in pressure in the velocity deficit regions. As velocity on the blades and the wake are a result of mutual induction between circulation from the lifting body and the wake, it is important to understand the role of vortices in the wake and on the blade geometry.

The vortices created by the lifting blade comprises of three components; the bound vortex, which is created by the lifting body, the trailing vortex, which is shed at blade discontinuities from the tip and the root (see figure 2.1), and the starting vortex, which is created the moment the blade starts generating lift (see figure 2.2). The blade, just like any lifting body, creates a bound circulation proportional to its lift, expressed by Equation 2.2.

$$L = \rho V_\infty \Gamma \tag{2.2}$$

where, V_∞ is the stream transport velocity and Γ is the circulation created by the lifting

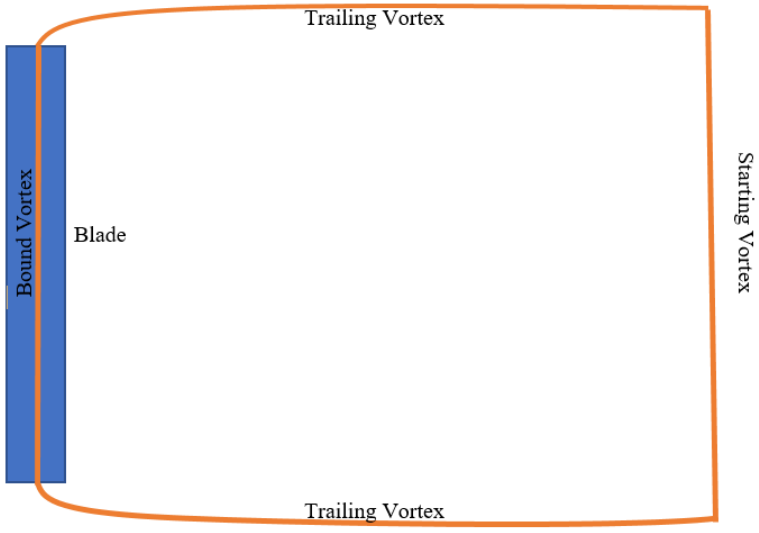

Figure 2.2: The vortex domain: the bound vortex on the blade, the trailing vortices at the tips and the starting vortex.

body. According to Helmholtz's 2^{nd} theorem, the vortex line cannot end in space and must be a closed loop. The total closed vortex domain can be seen in figure 2.2.

Velocity of the fluid within the bounds of the vorticity domain is lower when compared to the free stream, this forms a region of increasing pressure in the domain. This, in turn, causes the wake to expand, pushing the trailing vortices outwards. This region of higher pressure is defined as the wake of the turbine and it can be further decomposed into near wake and the far wake.

The near wake is described as the downstream region of the turbine where the blade geometry and the turbine configuration dictates the flow conditions such as stalled flow, tip vortices, and 3-D flow (Vermeer et al., 2003). It extends to approximately one rotor diameter downstream. Further downstream, the viscous and diffusive forces begin to have a stronger influence on the flow.

The far wake is defined as the downstream region of the turbine where guiding principles for the flow field are convection and turbulent diffusion (Vermeer et al., 2003). The far wake becomes very important in the study of wind farms.

As the near wake is closely governed by the turbine configuration, when the attitude of the turbine is maintained in line with the freestream velocity, the inflow velocity experienced by the blade sections remains constant through the rotation. The inflow velocity vectors and the tip speed ratio are used to compute the angle of attack, which remains constant for a constant tip speed ratio as seen in figure 2.3. The uniform loading on the turbine blade section in a HAWT produces a uniform wake and the wake is symmetric along the axis of the turbine, which is explained in section 2.2.1. This is due to the uniform loading and axisymmetric thrust on the blades. The angle of attack of the blade sections remains constant as the blade

changes its azimuthal position. This ensures that the lift distribution across the blade remains constant and hence the loading of the blade does not change through its azimuthal sweep.

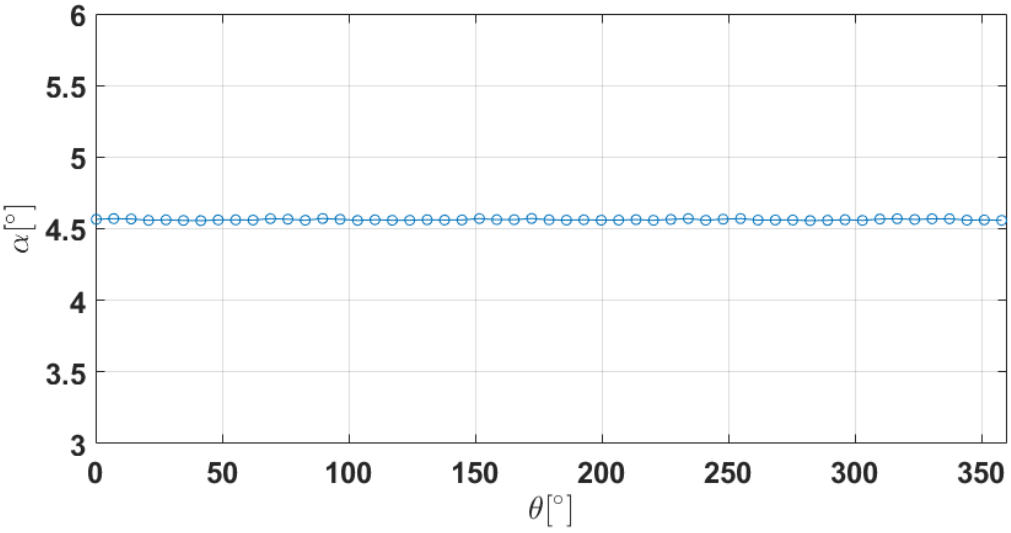

Figure 2.3: Variation of the angle of attack of the central blade section as a function of azimuthal angle for a HAWT (Radius = 0.45 m) at TSR of 6 and free stream velocity of 10 m/s.

When the turbine is yawed at an angle to the incoming freestream it causes a thrust vector reorientation, which results in an interesting behaviour of the wake. This is discussed in section 2.2.

2.2 Wake Deflection with a HAWT in Yaw

The HAWTs used today have a control system that helps them to orient their rotation axis along the freestream velocity vector. However, due to the rapid variation in inflow velocity direction, it is very difficult to keep the turbine oriented exactly along the velocity vector at all times. The wind turbine is considered to be yawed when the freestream velocity is not normal to the rotor plane of the horizontal axis turbine. Therefore, the wind turbine is mostly operating in a yawed configuration (Madsen et al., 2003), as the turbine cannot keep up with the rate of change in the direction of inflow.

This makes it very important to study its behaviour in yawed condition. Eggleston and Starcher (Eggleston and Starcher, 1990), show the variation of the wind direction with time in figure 2.5.

Figure 2.5 shows that the variation in yaw angle is too quick for the yaw control system to be able to accurately maintain the turbines heading against the wind. The maximum amplitude of the flow direction variation is noticed to be $\pm 30^\circ$.

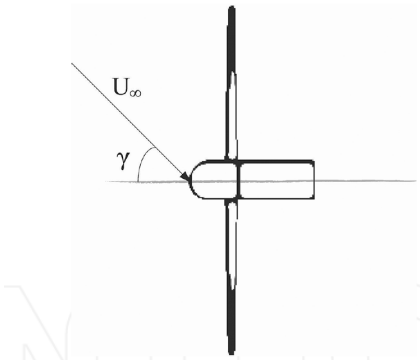

Figure 2.4: Wind turbine operating in yawed configuration as seen from top view (Micallef, 2015). The symbol γ denotes the yaw angle of the turbine with respect to the wind direction.

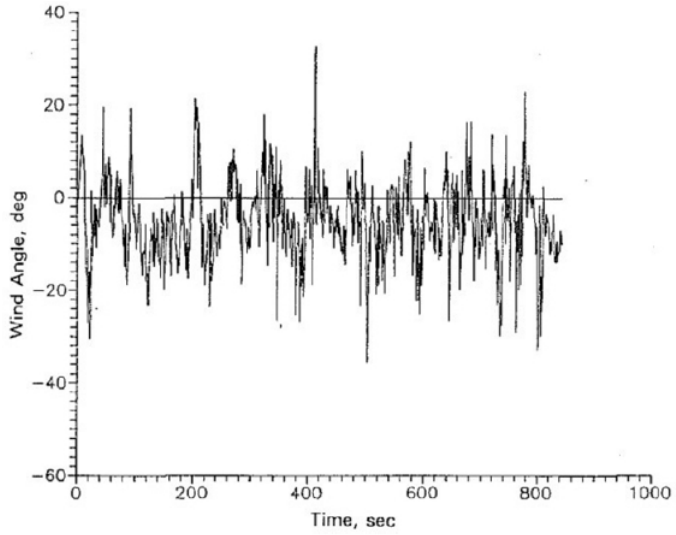

Figure 2.5: Variation of yaw angle with time experienced by Carter 25 turbine (Eggleston and Starcher, 1990).

The skewed inflow angle results in periodically varying inflow and the oscillation of the blade over a range of induced angles of attack. With the induced angle of attack, the loading on the blade will vary periodically. This leads to unsteady loading on the blades. The change in blade loading as a function of azimuthal angle is shown in figure 2.6.

The wake of the wind turbine contains helical vortices that originate from individual rotating blades. As the loading at the root and tip drops to almost zero, they can be treated as discontinuities. According to Helmholtz's 2^{nd} theorem, a vortex is shed from the root and tip that are consistent with the bound vortex on the blade. The geometry of the vortex sheet from the blade will roll up towards the root and the tip (Micallef, 2015).

The wake of the turbine expands due to an increase in pressure in the wake, as a result of velocity deficit. The wake expands more as more kinetic energy is extracted from the flow.

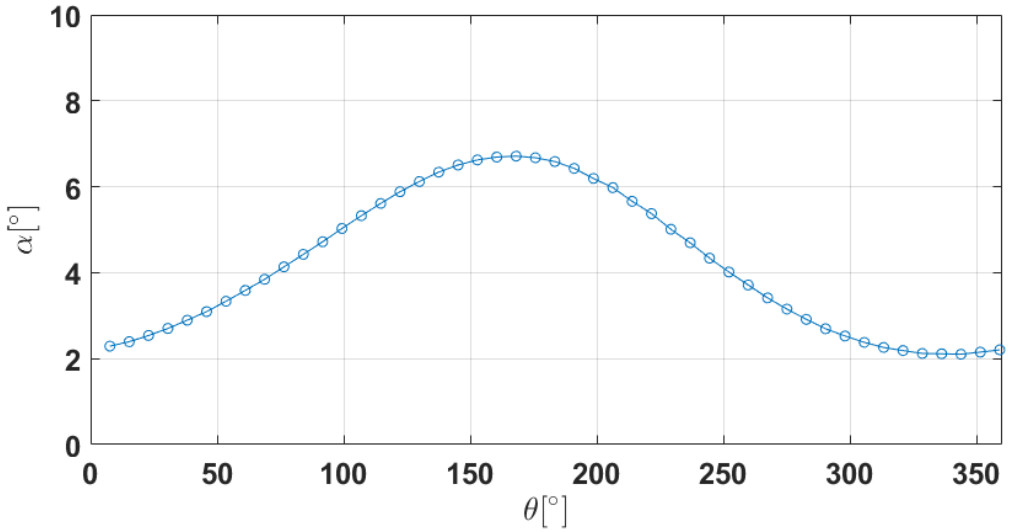

Figure 2.6: Variation of the angle of attack as a function of azimuthal angle for a HAWT in yawed configuration at TSR of 6 and free stream velocity of 10 m/s.

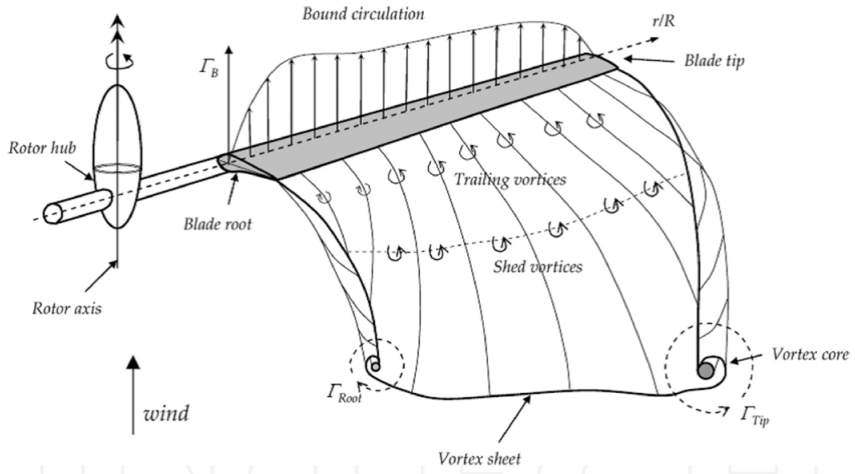

Figure 2.7: Formation of helical vortex sheet by a rotating blade (Micallef, 2015).

This corresponds to an increase in the thrust coefficient of the turbine, shown by Alfredsson and Dahlberg (Alfredsson and Dahlberg, 1979).

The yawed configuration inflicts a velocity component of the blade in the direction of freestream which results in a periodic advancing and retreating effect (Micallef, 2015). The inflicted velocity component due to the yaw configuration also induces a periodicity in the angle of attack experienced by the blade sections. The maximum velocity is experienced by the advancing blade and the minimum, by the retreating blade. This creates a difference in the energy extracted from the flow during the advancing and retreating sweep. The deflection of the thrust vector, results in the wake to be skewed. From figure 2.8, it can be seen that

the direction of total thrust has an axial and a spanwise component. The thrust, T, shown in figure 2.8 is the force acting on the turbine by the freestream. For the conventional frame of reference, the force of the turbine acting on the flow is represented by the same T vector in the opposite direction. Reversing the direction shows a component of thrust along the direction of wake deflection.

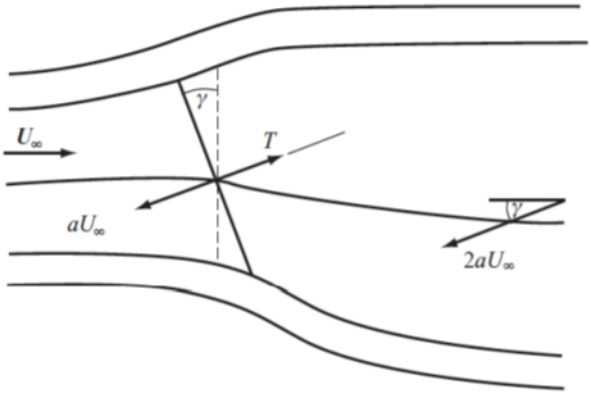

Figure 2.8: Yawed inflow with skewed wake and induced velocities (Burton et al., 2011). The thrust component is the resultant force acting on the turbine by the freestream.

In order to gain a deeper insight into the wake characteristics for a deflected wake, a coarse mesh simulation is carried out by the author to compare the velocity field with existing data from Howland et al., 2016 (Howland et al., 2016). This is seen in section 2.2.1.

2.2.1 Insight into wake deflection using the ALM for a HAWT in yaw

A coarse mesh simulation is carried out to gain a qualitative understanding of wake behaviour in the case of a deflected wake. The simulation is carried out using an ALM-RANS model (discussed in section 3.1.1 and section 3.2.3) implemented through the TurbinesFoam library of OpenFOAM (Bachant)(OpenFOAM, 2013). The wind turbine is simulated at 0° and 30° yaw angle. The velocity field and turbulence KE field are used to compare the wake between the deflected and the non-deflected case. The turbine used is the default HAWT configured in the TurbinesFoam library.

Figure 2.9 shows the wake of a HAWT in the un-yawed configuration. It is clear that the wake is axisymmetric. A velocity deficit is noticed in the wake. When the HAWTs are set in close proximity to each other such as within 5 rotor diameters from the upstream turbine, they would be subjected to lower inflow velocity as seen from figure 2.9. The loss of momentum and increased turbulence in the flow field caused by the up-stream turbine increases the unsteady loads on the subsequent turbines, in turn disturbing their optimal inflow condition, which results in reduced power extraction from the flow.

The results that are shown in figure 2.10 and figure 2.11 depict the wake deflection at 30° yaw

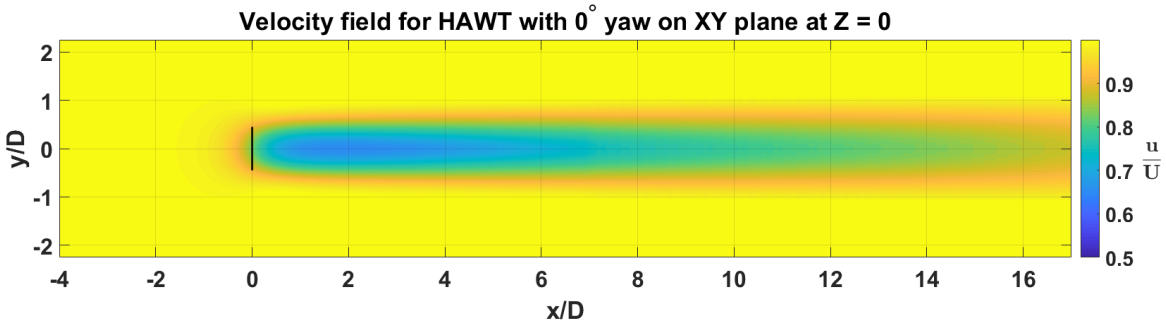

Figure 2.9: The wake of a HAWT at TSR of 6 and free stream velocity of 10 m/s turbinesFoam. The turbinesFoam simulation results are obtained by ALM-RANS at TU Delft by the author.

angle from Howland et al., (Howland et al., 2016) and turbinesFoam (Bachant) simulation respectively.

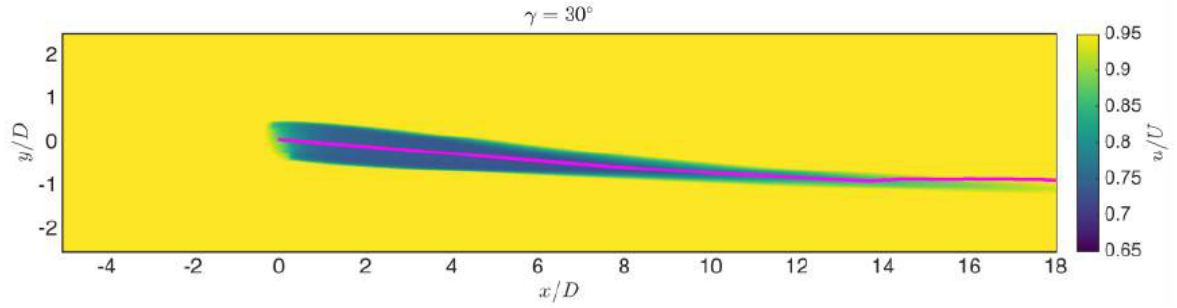

Figure 2.10: Time-averaged mean velocity contours normalised by the free stream velocity on a horizontal plane at hub height z/D = 0 obtained from the ADM-LES. The centre of the wake is shown in magenta (Howland et al., 2016).

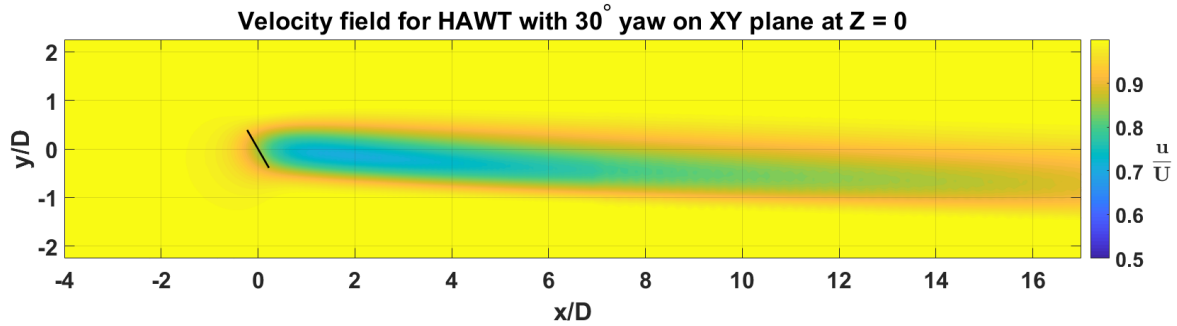

Figure 2.11: The velocity field of the wake of a HAWT in yawed configuration at TSR of 6 and free stream velocity of 10 m/s from turbinesFoam. The turbinesFoam simulation results are obtained using the ALM-RANS model at TU Delft by the author.

Figure 2.12 and figure 2.13 compare the turbulent kinetic energy for a HAWT in yawed and un-yawed configuration. In the case of un-yawed configuration, figure 2.12 shows the axisymmetric distribution of the turbulent kinetic energy in the wake. This is due to the constant blade loading through one rotation. The constant loading sheds vortices of consistent strength, proportional to the change in its sectional bound circulation, which causes uniform diffusion of the vortices in the wake. However, in the case of yawed configuration, figure 2.13 shows that the turbulent kinetic energy in the wake is no longer axisymmetric, as the loading on the blade section is now a function of its azimuthal position due to the advancing and retreating effects. The non-uniform loading causes the vortices shed in the wake to be a function of the azimuthal position of the wake. Vortices shed from the advancing sweep have a greater bound circulation due to the increased lift which results in an increased flow mixing in the wake. The turbulence wake profile is also skewed by the net cross force component in the wake.

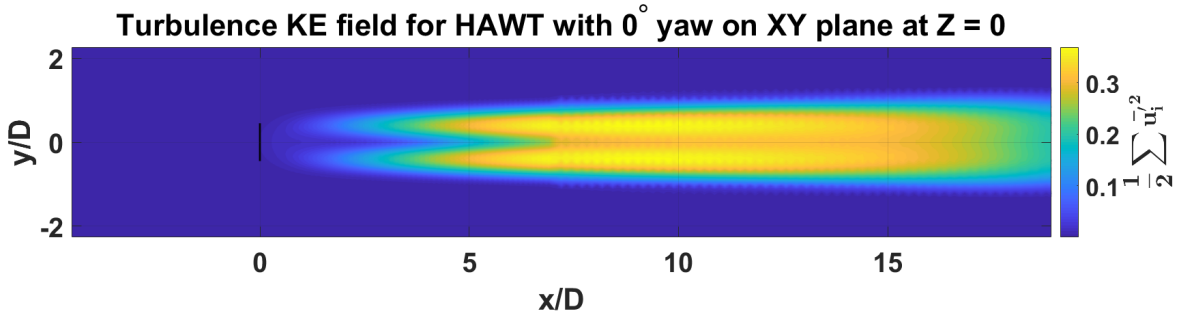

Figure 2.12: Turbulence kinetic energy for a HAWT in un-yawed configuration at TSR of 6 and free stream velocity of 10 m/s from turbinesFoam. The turbinesFoam simulation results are obtained using the ALM-RANS model at TU Delft by the author.

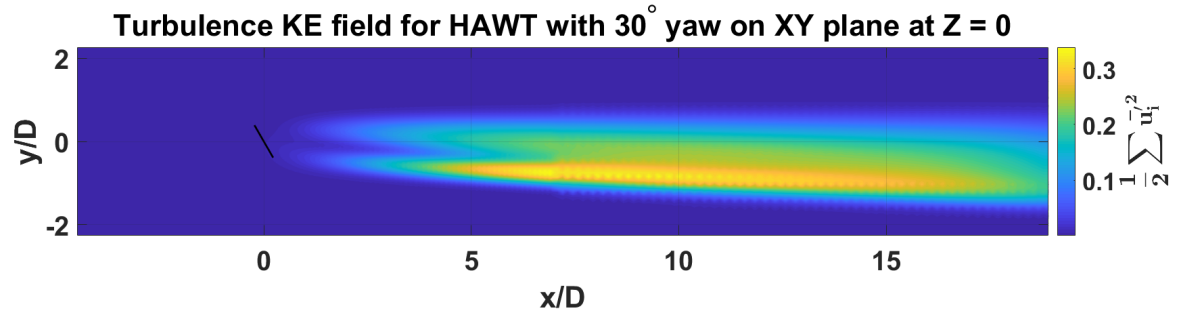

Figure 2.13: Turbulence kinetic energy for a HAWT in yawed configuration at TSR of 6 and free stream velocity of 10 m/s from turbinesFoam. The turbinesFoam simulation results are obtained using the ALM-RANS model at TU Delft by the author.

The yawing of the wake also contributes a feedback phenomenon that creates a yaw restoring moment. According to Schepers and Schreck, 2013, the turbines in yawed configuration

experience an opposing yawing moment (Schepers and Schreck, 2013). It is explained that this moment is generated by the skewed wake geometry and not by advancing and retreating action of the blades. The deflected wake causes the trailing tip vortices to move closer to the downwind side of the rotor due to which the induced velocities on the upwind side are lower. The asymmetric induction produces an axial thrust on the blade section on the upwind side, creating an opposing moment (see figure 2.14).

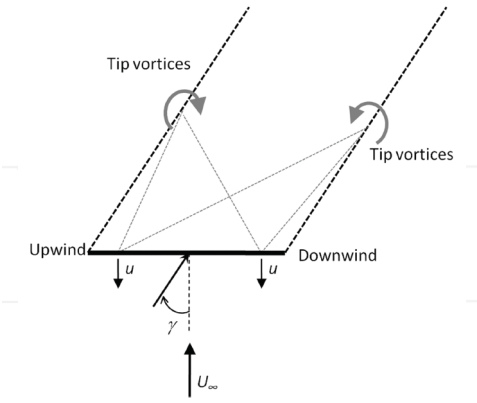

Figure 2.14: Asymmetric induced velocities in the case of a skewed wake for a HAWT in a yawed configuration (Schepers and Schreck, 2013).

It is important to understand that as the yaw angle increases, the turbine performance reduces. Therefore. an optimal compromise between the performance reduction of one turbine in yawed configuration and the total performance of the farm has to be met. Bastankhah and Porte-Agel show the trend in reduction of power with an increase in yaw angle (Bastankhah and Porte-Agle, 2016).

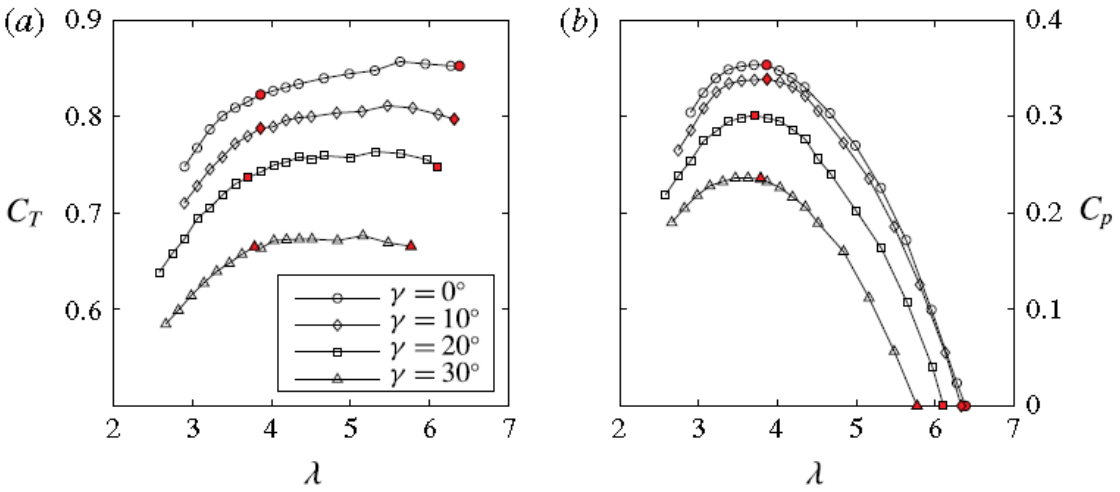

Figure 2.15: Turbine performance versus tip speed ratio (Thrust Coefficient C_T (a) and power coefficient C_P (b)) for different yaw angles (Bastankhah and Porte-Agle, 2016).

It is observed from figure 2.15, that the performance drops sharply with an increase in yaw

angle, however, figure 2.16 shows that the change in wake deflection angle reduces with an increase in yaw angle. A fair compromise is reached with an optimum yaw angle of 30°. This is due to the fact that further yawing the turbine would not result in significant wake deflection but the performance of the turbine would drop considerably.

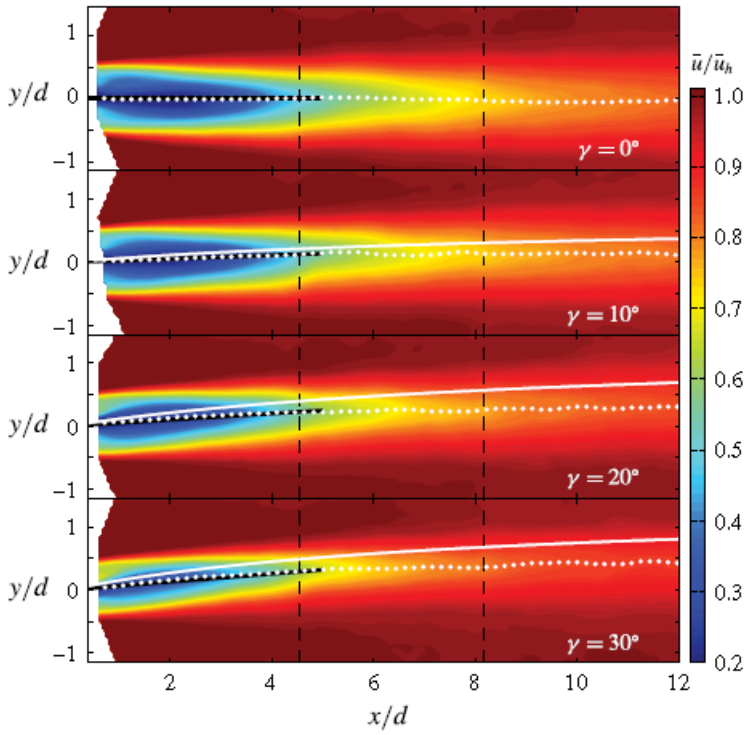

Figure 2.16: Contour of normalised mean streamwise velocity for different yaw angle. The white dots and lines represent the wake trajectories (Bastankhah and Porte-Agle, 2016).

The wake deflection by turbines in yawed configuration has proved to be effective for which a simple relation between yaw angle and wake skew angle is derived Jimenez et al. They developed a relation by assuming a top hat velocity deficit profile (Jimenez et al., 2009). They assume that the velocity deficit in the wake is negligible and the velocity in the wake is uniform. Additionally, they also assume that the wake deflection angle is small. The relation they obtain is,

$$\Theta = \frac{\cos^2\gamma \sin\gamma C_T}{2(1+\varsigma\frac{x}{D})^2} \tag{2.3}$$

where Θ is the wake skew angle, γ is the turbine yaw angle, C_T is the turbine thrust coefficient, ς is the wake growth rate and $\frac{x}{d}$ is the distance downwind in terms of rotor diameter.

The deflection of wake under yawed condition occurs due to the cross-component of the thrust vector with the asymmetric loading of the blades along azimuthal positions. This provides the basis to derive methods for wake deflection in VAWT. To do this, first, the aerodynamics of the VAWT must be understood.

2.3 Vertical Axis Wind Turbines

Vertical axis wind turbines (VAWT), as the names suggests, are wind turbines whose axis are normal to the ground or sea. There are two types of vertical axis turbines, drag driven and lift driven turbines. For this thesis, the focus is solely on the lift driven turbines. Lift driven turbines are so called as they derive torque from the lift force. The VAWTs hold numerous advantages over the HAWTs. They have a low initiation wind speed. They are omnidirectional and therefore do not require yaw control which is a very important advantage as a lot of failures in the HAWT are due to errors in the yawing system (Arabian-Hoseynabadi et al., 2010). Presence of the generator at ground level reduces the design, installation and maintenance cost of the turbine. VAWTs have a low centre of gravity, which makes them ideal for off-shore installations. However, one major disadvantage that is faced by VAWTs when compared to HAWTs is that the blades of VAWTs undergo cyclic loading as the lift force produces torque only for a section of the azimuthal sweep (see figure 2.17 for the variation of α with azimuthal angle). Figure 2.17 shows that the blade advances towards the wind in

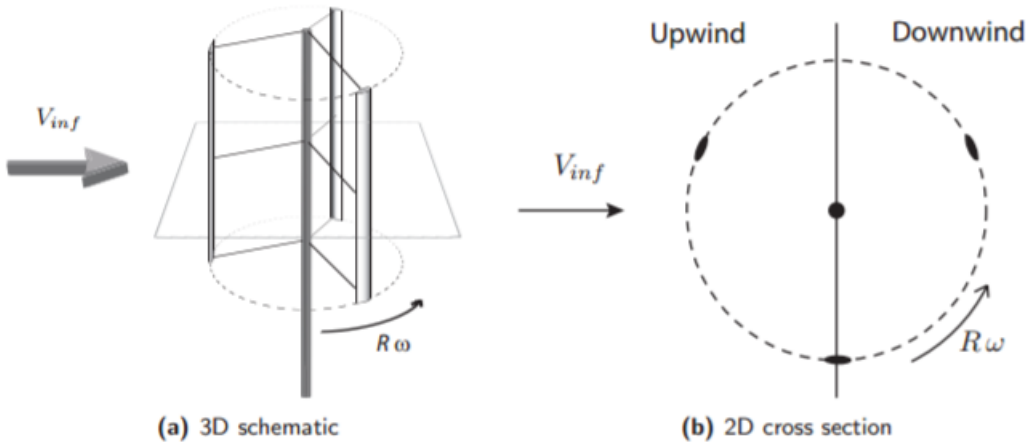

Figure 2.17: : Cross-section of the turbine (Claessens, 2006).

one-half of the blade sweep and retreats during the other half. The relative velocity and the angle of attack experienced by the blade are therefore not constant over its azimuthal sweep. This induces cyclic effects on the blade.

It is very important to understand the aerodynamics of such a dynamic model. The most important parameter for the performance of a blade in a wind turbine is its angle of attack. The orientation of the vertical axis turbine subjects the blade to a wide range of angle of attacks. The angle of attack is a function of free stream velocity and rotation velocity of the turbine, i.e. tip speed ratio, and the azimuthal position of the blade. The tip speed ratio is given by

$$\lambda = \frac{\Omega R}{V_\infty} \tag{2.4}$$

where Ω is the rotation rate of the turbine, R is the turbine radius and V_∞ is the free stream

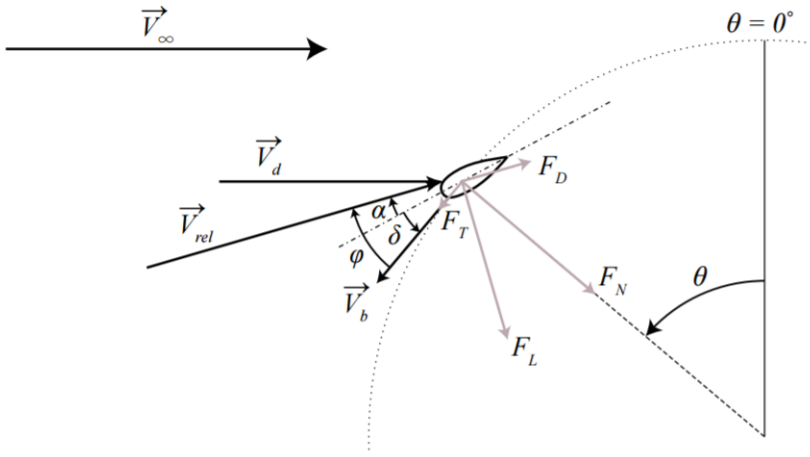

Figure 2.18: The reference orientation of a VAWT blade and its parameters (Dyachuk, 2015).

velocity. The angle of attack changes with the relative velocity experienced by the blade.

$$V_{rel} = V_d \sqrt{\left(\frac{\Omega R}{V_d} + \sin\theta\right)^2 + (\cos\theta)^2} \tag{2.5}$$

Then the angle of attack varies as

$$\alpha = \tan^{-1}\left(\frac{\sin\theta}{\lambda + \cos\theta}\right) \tag{2.6}$$

This, however, is only valid for a quasi-static case. In the case of a continuous rotation, more effects come into play that influence the angles of attack.

The first of these effects is the flow curvature effect. Usually, the angle of attack experienced by the turbine blade is assumed to be the same along its chord. However, a study by Migliore et al. (Migliore et al., 1980) showed that due to the rotation of the VAWT, the blade does not have a constant angle of attack along its chord. The curvilinear flow field subjects the blade to a different angle of attack at different $\frac{x}{c}$.

As a symmetric aerofoil rotates in a curved flow field, its behaviour changes to that of a cambered aerofoil when immersed in a linear flow field. The transformation of curved flow field to linear flow field virtually bends the aerofoil to achieve a virtual camber. The influence of flow curvature is directly proportional to the chord to radius ratio of the turbine.

The HAWT in yawed configuration is subjected to a variation of the angle of attack with the azimuthal position of the blade. When comparing the behaviour of a HAWT in yawed configuration (figure 2.6) with that of a VAWT (figure 2.20), an important observation made is that the angle of attack in the case of HAWT in yaw does not become negative as the leading edge of the blade always faces the incident flow. However, in the case of VAWT, as the rotation axis is perpendicular to the flow, the blade sections are subjected to negative angles of attack.

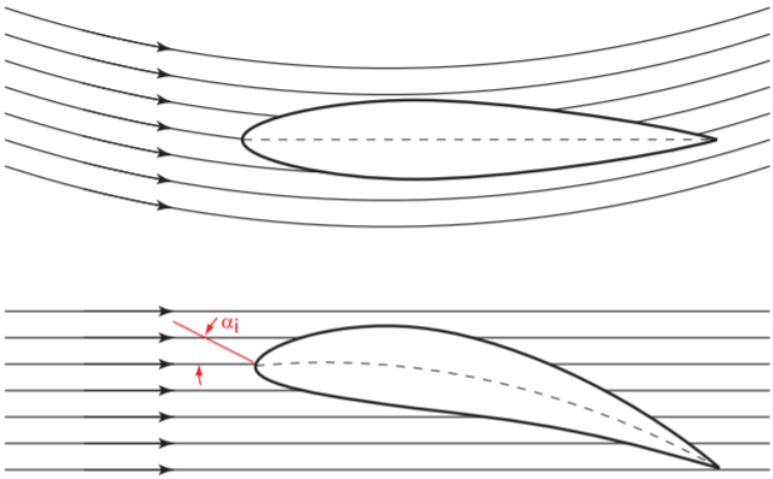

Figure 2.19: The curvilinear field results in a virtual camber (Migliore et al., 1980).

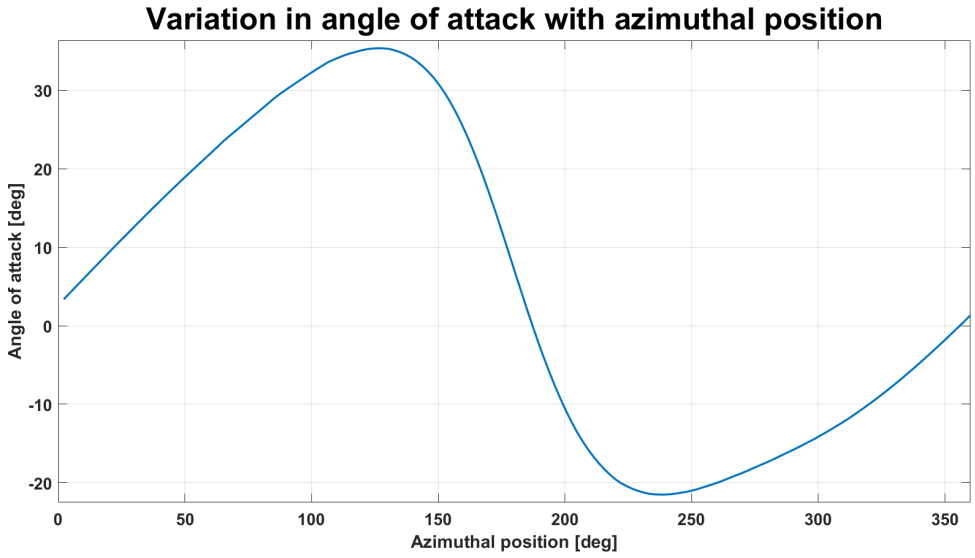

Figure 2.20: Variation of the angle of attack as a function of the azimuthal angle for a VAWT at TSR of 1.9 and free stream velocity of 1 m/s.

Now, as the aerofoil experiences a wide range of angles of attack, (see figure 2.20) the lift characteristics of the blade takes on a dynamic nature. As the blade traverses through its azimuthal position, the angle of attack increases and the blade section begins to stall as the flow begins to separate at the trailing edge. As the angle of attack further increases, the flow separation point begins to move towards the leading edge. This is called deep stall. The flow, however, does not reattach upon reducing the angle of attack to its pre-stall angle. The angle of attack has to be further reduced for the flow to reattach, this phenomenon is referred to as hysteresis.

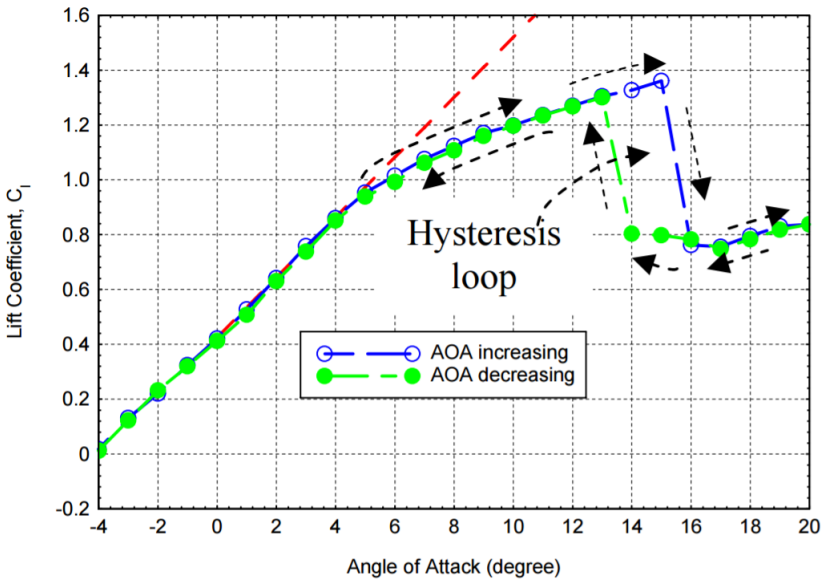

Figure 2.21: Hysteresis loop of an aerofoil's lift coefficient (Yang et al., 2008).

The power generated by vertical axis turbines is directly proportional to the tip speed ratio, i.e. the rotational speed, which is accompanied by unsteady aerodynamics on the blades. As the tip speed ratio increases, so does the rate of change of angle of attack. This results in a hysteresis effect of its lift, drag and moment characteristics. This, in turn, results in shedding of vortices from the suction side of the aerofoil. These vortices pass over the leading edge and trailing edge, into the wake. This is called dynamic stall. The main contribution to induce dynamic stall is due to the moving aerofoil and the flow separation over its surface.

The visualisation of the dynamic stall was carried out by Fraunie et al. in 1986 (Fraunie et al., 1986) using a Laser Doppler Velocimetry in a water channel. The leading edge vortex is shed at the position 1 in figure 2.22 (b) with the corresponding trailing edge vortex shed at position 2. The two counter-rotating vortices are shed into the wake which interacts with the blade downstream.

Figure 2.23 shows the wake of a VAWT. Comparing the wake from the HAWT in an un-yawed configuration and the wake from the VAWT from figure 2.9 and figure 2.23 respectively, it is clearly seen that the wake profile for the two cases is very similar. This is expected as the overall function of the turbines is to extract the energy from the flow velocity. The turbulent kinetic energy profile for a VAWT distinctly shows the increased turbulence level due to the shed vortices.

Comparing the turbulent kinetic energy profile (ignore the magnitude as the flow conditions are vastly different) for the case of a HAWT in the un-yawed configuration (figure 2.12) and VAWT (figure 2.24), it is observed that the vortices shed from the blade tips in the case of a HAWT, take longer to merge when compared to those from a VAWT. The wake of the

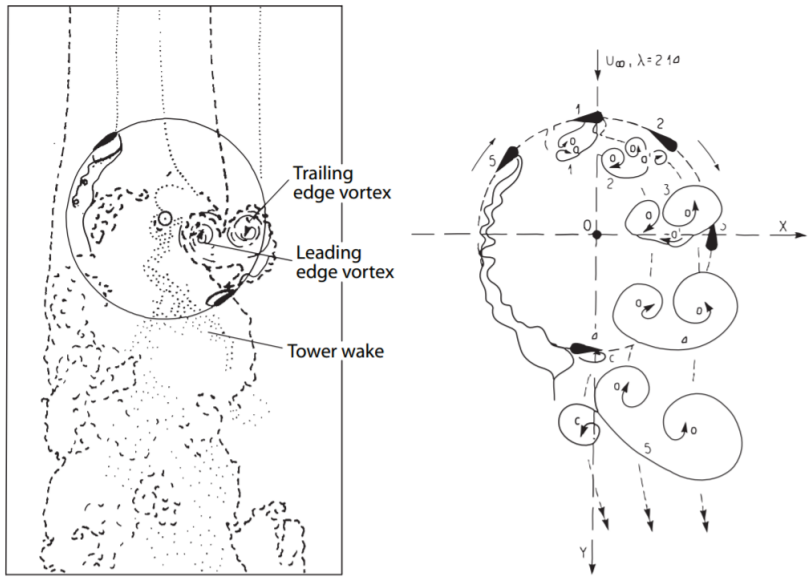

(a) Flow visualization **(b)** Schematic diagram

Figure 2.22: Visualisation of dynamic stall (Fraunie et al., 1986). The illustration is that of a 2-blade (NACA 0018) Darrieus turbine in a water channel at Re = 10,000 at $\lambda = 2.14$.

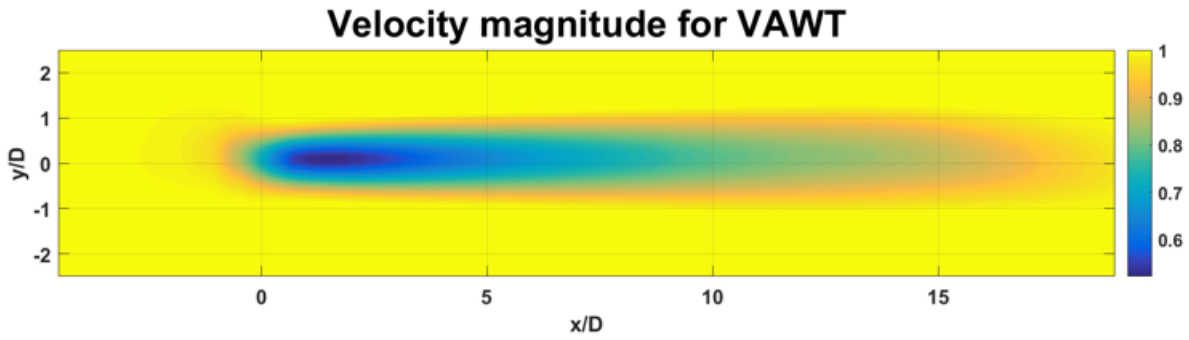

Figure 2.23: The velocity field of the wake of VAWT at TSR of 1.9 and free stream velocity of 1 m/s from turbinesFoam. The turbinesFoam simulation results are obtained using the ALM-RANS model at TU Delft by the author.

VAWT has high turbulence intensity as each blade passes through the wake of the previous blades. The increased blade-wake interaction and the mutual interaction of the wakes of each turbine blade results in higher turbulent dissipation and flow mixing. Work by Ferreira et al. (Ferreira et al., 2010) provides a detailed insight into 3D wake dynamics using a two-bladed H-Darrieus VAWT. They use a 3D unsteady panel method to model the blades and the wake, and stereo PIV measurements to validate the results. Hezaveh et al. (Hezaveh et al., 2016) provide an insight into the effects of the tip speed ratio, solidity, and the aspect ratio, D/L, in the wake of the VAWT.

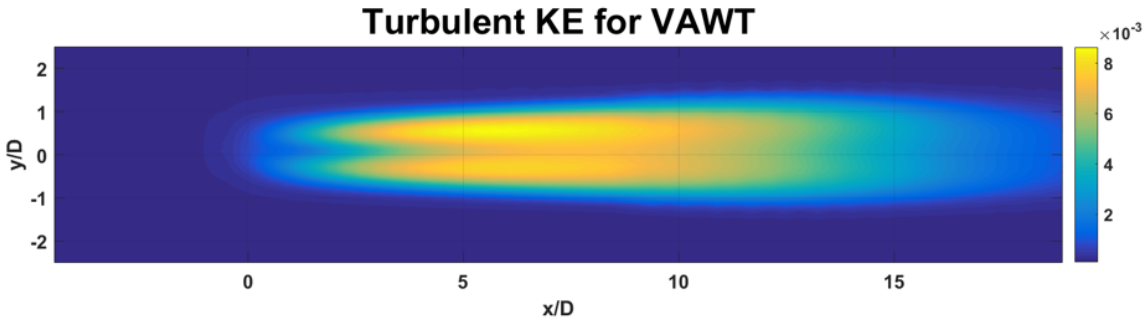

Figure 2.24: Turbulence kinetic energy for a VAWT at TSR of 1.9 and free stream velocity of 1 m/s from turbinesFoam. The turbinesFoam simulation results are obtained using the ALM-RANS model at TU Delft by the author.

When comparing the turbulent kinetic energy profile for the case of a HAWT in yawed condition (figure 2.13) and VAWT (figure 2.24), a common trait observed is that in both the cases the turbulent kinetic energy is higher, on the side of higher blade loading for the HAWT and the blade sweep for VAWT. However, almost no wake deflection is seen in the VAWT as from figure 2.23 it can be seen that the difference in turbulent kinetic energy on the advancing and the retreating sweep is very small when compared to that of the HAWT in yaw (figure 2.13).

Seyed Hossein Hezaveh et al. (Hezaveh et al., 2016) simulated various cases of a VAWT with different configurations. The various cases provided in figure 2.25, are done by simulating different rotor parameters for a constant frontal turbine area. The aspect ratio is modified by varying the blade length and the rotor diameter for a constant frontal area. It is evident that the velocity deficit in the wake is greater for the cases involving higher aspect ratios as it extracts more momentum from the flow due to its larger azimuthal sweep area. The cross-section of the wake reduces in Y direction with an increase in tip speed ratio and a decrease in solidity.

In order to develop a method for wake deflection, it is important to simulate the cases for various rotor parameters and flow conditions. To do so, the modelling techniques involved need to be reviewed.

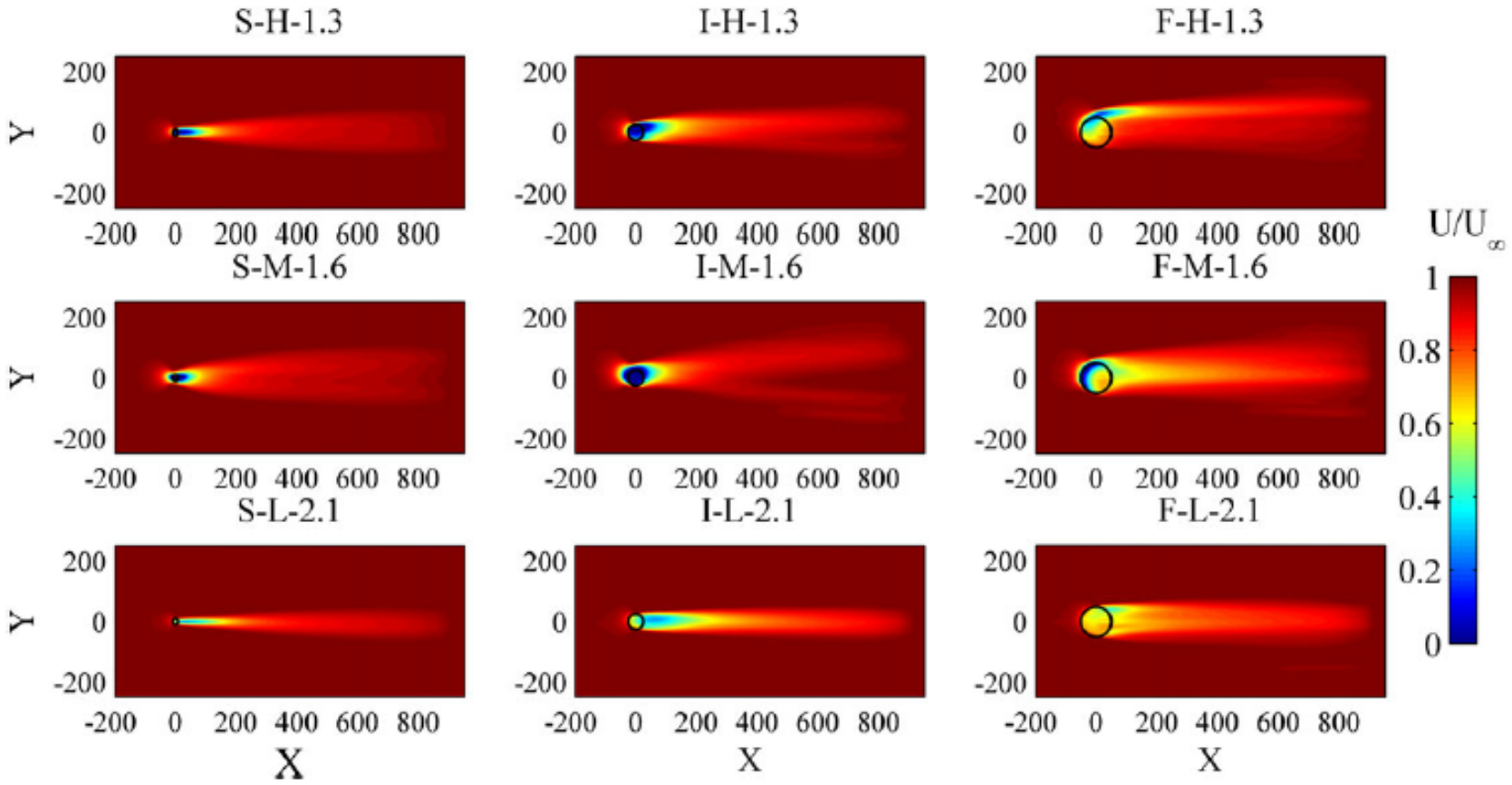

Figure 2.25: Time-averaged normalised streamwise velocity averaged in Z over the length of the blades. The notation over the represented flow fields is as follows. The first letter denotes the aspect ratio, S is when D/L = 0.2, I when D/L = 1.25 and F when D/L = 5. The second letter denotes the solidity, L when solidity = 0.08, M when solidity = 0.15 and H when solidity = 0.25. The digits denote the tip speed ratio (Hezaveh et al., 2016).

Chapter 3

Flow and Rotor Modelling

Having reviewed the aerodynamics of wind turbines, it is crucial to look into modelling the behaviour of the flow around the turbine. For the thesis, the focus is primarily on understanding the wake behaviour and not on the flow over the geometry of the turbine. Modelling the flow around a wind turbine can be divided into two parts, modelling of the flow and modelling of the turbines. The focus of this study is on the behaviour of the far wake. The far wake, as discussed in section 2.1, is guided by turbulent mixing and dissipation. This requires the thesis to focus on the turbulence models. These are discussed in section 3.1.

3.1 Flow Modelling

In general, the flow through wind turbines is an incompressible and an unsteady flow. This flow is represented by the incompressible unsteady Navier-Stoke's continuity and momentum equations (Sanderse et al., 2011). Neglecting the buoyancy effects and thermal exchanges, the Navier-Stoke's equations are,

$$\nabla \cdot u = 0 \tag{3.1}$$

$$\frac{\partial u}{\partial t} + (u \cdot \nabla)u = -\frac{1}{\rho}\Delta p + \nu \nabla^2 u \tag{3.2}$$

These equations can be solved in diverse ways, each compromising between the accuracy in capturing the turbulence in the flow and computation time. The most accurate method of solving these equations is by using Direct Numerical Simulation (DNS). This method solves for all scales of turbulence but is computationally very expensive. The computation expense can be reduced by resolving the turbulence up to a certain length scale and only considering the overall effects of the smaller turbulence scales. This method is called a Large Eddy Simulation (LES) and it is computationally less heavy when compared to DNS with a compromise in

the turbulence resolution. However, the quality of the results depends heavily on the mesh resolution, which may increase the computation load.

Another technique of resolving turbulent flows is by decomposing the velocity field into its steady and unsteady component, called Reynolds Averaging. LES and Reynolds-Averaged Navier-Stokes (RANS) are most popular methods adopted to solve the Navier-Stokes equations.

3.1.1 Reynold's Averaged Navier-Stokes equations

RANS provides the flow solution in a statistical manner by decomposing the basic flow properties of pressure and velocity into a fluctuation and an averaged component. This splitting of the properties is called Reynolds decomposition, as shown below

$$u(x,t) = \bar{u}(x,t) + u'(x,t) \tag{3.3}$$

where, $\bar{u}$ is the time averaged (steady) component and u' is the fluctuating component. The averaging of the steady component is guided by $\bar{\bar{u}} = \bar{u}(x)$ and that of the fluctuating component is guided by $\bar{u'}(x,t) = 0$. Applying the Reynolds decomposition to the Navier-Stokes equations results in,

$$\frac{\partial \bar{u}}{\partial t} + (\bar{u} \cdot \nabla)\bar{u} = -\frac{1}{\rho}\Delta\bar{p} + \nu\nabla^2\bar{u} - \nabla \cdot \overline{u'u'} \tag{3.4}$$

where $\nu\nabla^2\bar{u} - \nabla \cdot \overline{u'u'}$ is the total diffusion term. $\overline{u'u'}$ is the Reynolds stress tensor which appears from the non-linearity in the Reynolds-Averaged convective term. The Reynolds stress tensor represents the diffusion due to the turbulence. The $\nu\nabla^2\bar{u}$ component of diffusion is the molecular diffusion term. This leaves the equation in terms of averaged and fluctuating quantities. To solve the equation, the Reynolds stress tensor needs to be represented in terms of the averaged velocity. This is done by using the Boussinesq hypothesis (Boussinesq, 1877) (Schmitt, 2007). The Boussinesq hypothesis introduces an eddy viscosity ν_T, which represents the Reynold stress tensor as a function of mean velocity gradients and eddy viscosity.

$$\overline{u'u'} = \nu_T(\nabla\bar{u} + (\nabla\bar{u})^T) \tag{3.5}$$

The resulting RANS equation to be solved is,

$$\frac{\partial \bar{u}}{\partial t} + (\bar{u} \cdot \nabla)\bar{u} = -\frac{1}{\rho}\Delta\bar{p} + \nabla((\nu + \nu_T)(\nabla\bar{u} + (\nabla\bar{u})^T)) \tag{3.6}$$

The Boussinesq approximation does not physically hold true as viscosity due to eddies is not related to the molecular viscosity (Schmitt, 2007). The Boussinesqs hypothesis only reduces the dependency of computation load on Reynolds number. The determination of ν_T is often done using a $k-\epsilon$ model, where additional equations are solved for turbulent kinetic energy (k) and turbulent diffusion rate (ϵ) (Launder and Spalding, 1974).

3.1.2 Large Eddy Simulations

In order to accurately capture the large-scale eddy structures in the turbulent wake of the wind turbine, LES is an increasingly popular solver used in wake aerodynamics. This method is significantly more accurate in capturing anisotropic turbulent flows (Sanderse et al., 2011). This method accurately models the eddies that are of the length scale of mesh grid whereas a length scale smaller than the mesh grid are considered to have a more general behaviour and assumed to not depend on the geometry. The LES model was first developed by Joseph Smagorinsky in 1963 to study the atmospheric eddies (Smagorinsky, 1963). The selection and separation of length scale to distinguish between the large eddies and the smaller ones are carried out by spatial filtration of velocity. This filters the field velocity into a large eddy component and a filtered (small eddy) component. The filtration is done using a convolution integral,

$$\tilde{u}(x,t) = \int u(\xi,t)G(x-\xi,\Delta)d\xi \tag{3.7}$$

Here $G(x-\xi,\Delta)$ is the convolution kernel and Δ is the filtration width and $\tilde{u}$ is the velocity corresponding to the large eddies, filtered velocities (Sanderse et al., 2011).

The small eddies are smaller than the grid size and hence the corresponding velocities are called subgrid velocities, and defined by,

$$u'(x,t) = u(x,t) - \tilde{u}(x,t) \tag{3.8}$$

Applying the filtration to the Navier-Stokes momentum equation,

$$\frac{\partial \tilde{u}}{\partial t} + (\tilde{u}\cdot\nabla)\tilde{u} = -\frac{1}{\rho}\Delta\tilde{p} + \nu\nabla^2\tilde{u} - \nabla\cdot(\widetilde{uu} - \tilde{u}\tilde{u}) \tag{3.9}$$

The $(\widetilde{uu} - \tilde{u}\tilde{u})$ component covers the subgrid-scale stresses which represent the effects of the smaller eddies that are filtered. Smagorinskys subgrid model is most widely used to compute the subgrid-scale stresses (Smagorinsky, 1963). The Smagorinsky's subgrid-scale model applies Boussinesq's hypothesis to relate the subgrid-scale stresses to the velocity gradients corresponding to large eddies.

$$\tau_{SGS} = (\widetilde{uu} - \tilde{u}\tilde{u}) = -\nu_{SGS}(\nabla\tilde{u} + (\nabla\tilde{u})^T) \tag{3.10}$$

The calculation of the subgrid-scale viscosity, ν_{SGS} is done using $k-\epsilon$ models. This model is used by Jimenez et al. in 2007 (Jimenez et al., 2007) with periodic boundary conditions to study the turbulent properties of the flow in the wind turbine wake. The model is used again by Jimenez et al. in 2008 (Jimenez et al., 2008) to identify the spectral coherence of turbulent fluctuations. This model is yet again used for the study of wake deflection by Jimenez et al. in 2010 (Jimenez et al., 2009).

Although the LES models are more suited for capturing the behaviour of eddies in the flow, they are still applied to flows with moderate Reynolds numbers due to computational constraints. Carrying out LES to study separation in a true-time sense continues to be unaffordable (Vermeer et al., 2003). A hybrid RANS/LES model provides a good compromise

between the computational ease of RANS and capturing the eddy behaviour of eddies. Such models are called Detached Eddy Simulations (DES).

3.2 Rotor Modelling

The simulation of the flow across the wind turbine is carried out using a variety of models developed over time. These can be classified into two sections. The first is where the geometry of the turbine is accurately depicted by the mesh and the flow is solved using traditional Navier-Stokes solvers (RANS, LES, DNS) and the second where the turbine's influence is inherently modelled into the Navier-Stokes equation. In the first option, the accuracy of the load prediction on the blades is highly dependent on the quality of the geometric representation of the aerofoil, and the mesh is very complex around the turbine body.

The projection of forces of the blades, on the fluid results, requires fewer grid points to simulate the effect of the blades on the flow in contrast to simulating a geometrical body. This also allows for a more simple mesh of the flow domain (Mikkelsen et al., 2007). This is done by applying the forces exerted by the turbine on the flow, onto the mesh points by means of the body force term in the Navier-Stokes equations. The resulting Navier-Stokes equation,

$$\frac{\partial u}{\partial t} + (u \cdot \nabla)u = -\frac{1}{\rho}\Delta p + \nu\nabla^2 u + f_{body} \tag{3.11}$$

where, f_{body} is the body force applied as the effect of the rotor on the flow. This technique does not require complex geometric modelling of the turbine. Instead, it requires the accurate computation of the forces exerted by the turbine on the flow. There are various models for computing these forces with various approximations. A few of the models are described in the following subsections.

3.2.1 Actuator Disc Model (ADM)

The wind turbine rotor is designed to convert the kinetic energy in the flow to electric energy by creating a velocity deficit in the wake. The body forces exerted in the Navier-Stokes equation are imparted by the thrust and torque, and balanced with the inflow kinetic energy (Mikkelsen, 2003). The Actuator Disc Model (ADM) is a model that approximates the rotor of the axial flow turbine as a disc with a finite pressure jump across it. This is approximated by a constant axial induction factor, a, over the disc. This assumption gives the approximate velocity in the wake downwind of the disc.

$$a = \frac{U_\infty - U_W}{U_\infty} \tag{3.12}$$

where, U_∞ is the free stream velocity and U_W is the velocity downstream of the turbine. This constant induction factor is related to the uniform pressure, velocity and loading over the disc

along the stream tube. The ADM assumes an infinitely thin disc in an inviscid flow. There is no flow in and out of the control volume along the defined upper and lower boundaries (wake edges). The flow is steady and incompressible. The rotation of the wake continues far downstream and therefore the differential pressure balancing the rotation does not cause a change in axial momentum. This model computes the forces by attaining momentum balance across the disc using the constant axial induction factor.

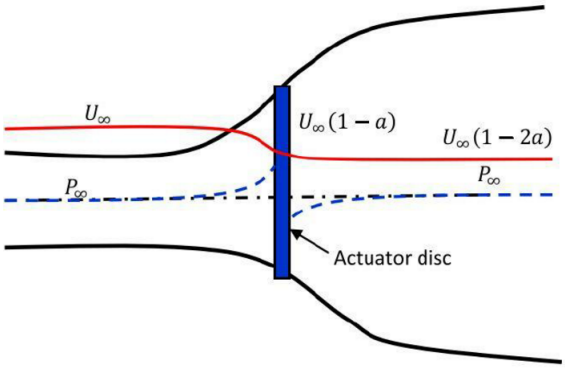

Figure 3.1: Actuator Disc Model (Ashrafi et al., 2015).

Figure 3.1 shows the approximation of the rotor as a disc and the flow conditions assumed upwind and downwind of the rotor. This is a low fidelity model and therefore is suited for computing the overall turbine performance and simulating wake expansion after the actuator disc.

The thrust can be calculated using momentum balance,

$$T = \dot{m}(U_\infty - U_W) \tag{3.13}$$

where, $\dot{m}$ is the mass flow through the upstream stream tube, $\dot{m} = \rho U_W A_W$. Here A_W is the wake area downstream and ρ is the density. The continuity equation at the rotor gives the relation, $uA_R = U_W A_W$, where, u is the velocity at the rotor, A_R is the area swept by the rotor. The power extracted by the disc is,

$$P = \frac{1}{2}\dot{m}(U_\infty^2 - U_W^2) = \frac{1}{2}(U_\infty - U_W)T = uT \tag{3.14}$$

From Equation 3.14 it can be concluded that $u = \frac{1}{2}(U_\infty - U_W)$. It is know that thrust, $T = C_T \frac{1}{2}\rho U_\infty^2 A_R$. Then, from Equations 3.12 and 3.13,

$$C_T = \frac{\rho u A_R (U_\infty - U_W)}{\frac{1}{2}\rho U_\infty^2 A_R} = 4a(1-a) \tag{3.15}$$

Similarly, the power extracted,

$$P = C_P \frac{1}{2} U_\infty^2 A_R \tag{3.16}$$

From Equations 3.12, 3.14, and 3.16,

$$C_P = \frac{\frac{1}{2}\rho u A_R (U_\infty^2 - U_W^2)}{\frac{1}{2}\rho U_\infty^2 A_R} = 4a(1-a)^2 \tag{3.17}$$

3.2.2 Blade Element Moment (BEM) Model

To improve the fidelity of the ADM, a variation of the properties on the plane has to be taken into account. For this, the stream tube is divided into smaller annular stream tubes which are assumed to not interact with each other (figure 3.2). Therefore, no mass flow or momentum exchange over the surface of the stream tube is possible. Each azimuthal section is influenced by its own local axial and tangential induction factor, which relates to the exerted thrust and torque, respectively. Besides the annular division, neither the force nor the induction factor distribution is known. For a closed-form solution, the blade element theory is applied. The induced velocity on the rotor disc determines the angle of attack of each blade section which in return provides the rotor forces. These should match the ones calculated by the ADM in order to have a physical model.

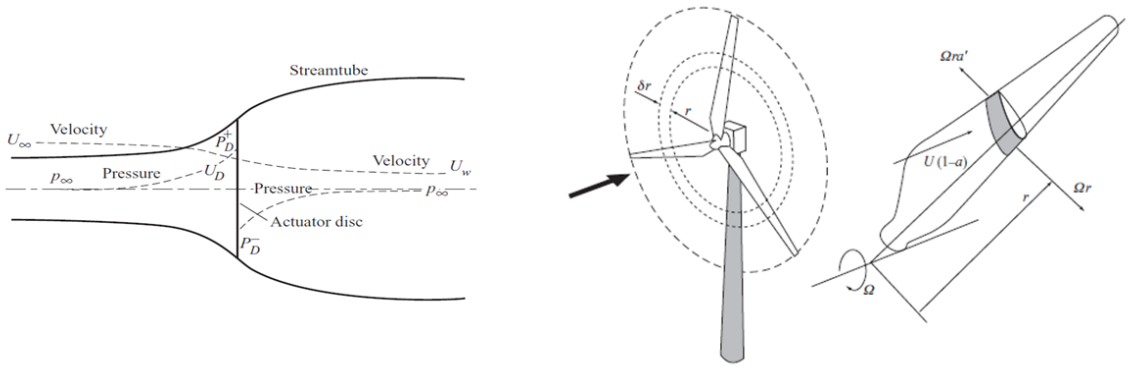

Figure 3.2: Blade Element Momentum approximation.

The BEM model assumes static incompressible inflow. The assumption that the force on the elements is only responsible for axial momentum change, there is no radial interaction of the flows between adjacent annuli, is only true when the tangential induction factor does not vary radially.

The relation between the AD (Actuator Disc) induction factors and the forces on the blade are determined through geometry and the provided aerofoil data (figure 3.3).

It must be noted that these induction factors are local to the blade. Due to the finite span of the blade, vortices are formed at the root and tip. These tip vortices introduce downwash to the blade and change the effective angle of attack. The angle of attack can be determined

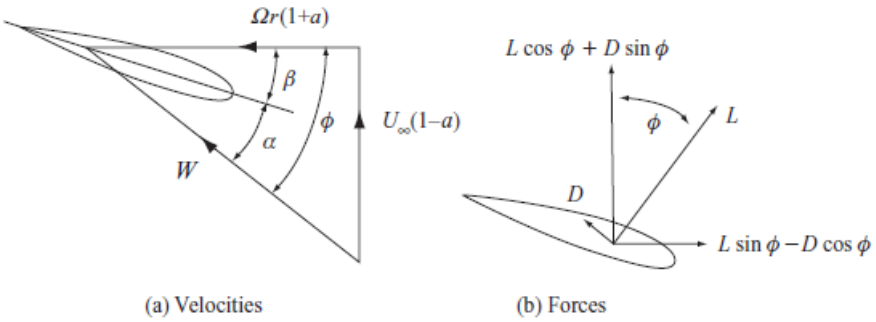

Figure 3.3: Velocities and forces acting on the aerofoil.

by the inflow angle. The last is defined as:

$$\phi(r) = \arctan\left(\frac{1}{\lambda r}\frac{1-a_b(r)}{1+a'_b(r)}\right) \tag{3.18}$$

λ is the tip speed ratio, r is the local radius of the annulus, $a_b(r)$ is the axial induction factor of the local annulus, and $a'_b(r)$ is the tangential induction factor of the annulus. The angle of attack is then given by:

$$\alpha(r) = \phi(r) - \beta - \Theta(r) \tag{3.19}$$

Here, α is the angle of attack, ϕ is the inflow angle, β is the blade pitch angle, and Θ is the twist distribution. From Equation 3.18 it is apparent that the induction coefficients are defined at the blade element. Due to the finite number of blades with a finite span, a momentum loss is encountered at the tip (and here also considered at the root of the blades), leading to a change of the particle velocity and trajectory and, as a result, the induction coefficient. This is caused by the formation of vortices at the tips. In order to account for this, Ludwig Prandtl developed a simple model of positioning a number of discs behind each other and developing a correction factor (Prandtl, 1923)(figure 3.4). The definition of the tip and root loss factors are:

$$f_t(r) = \frac{2}{\pi}e^{-\frac{B}{2}\left(\frac{1-\mu}{\mu}\sqrt{1+\frac{(\lambda u)^2}{(1-a)^2}}\right)} \tag{3.20}$$

$$f_r(r) = \frac{2}{\pi}e^{-\frac{B}{2}\left(\frac{\mu-\mu_t}{\mu}\sqrt{1+\frac{(\lambda u)^2}{(1-a)^2}}\right)} \tag{3.21}$$

The total factor is then,

$$f(r) = f_r(r)f_t(r) \tag{3.22}$$

The coefficients that are defined are the azimuthally averaged coefficients, as the particles close to the blade are influenced by it. In order to get the local coefficient of the blade used for the angle of attack calculation, the local blade induction factor is required. The azimuthally averaged coefficients can then be defined as (Burton et al., 2011):

$$a(r) = a_b(r)f(r) \tag{3.23}$$

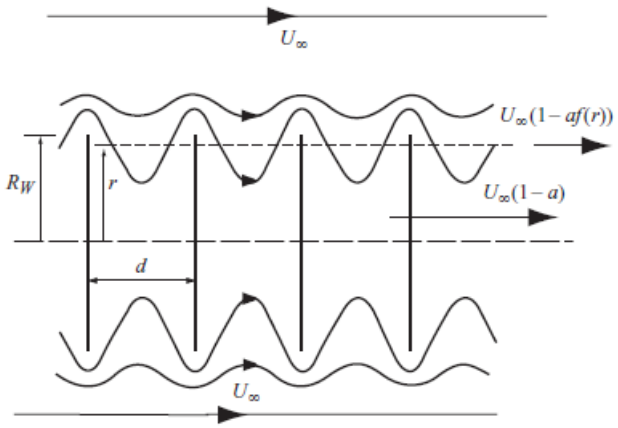

Figure 3.4: Prandtls tip loss model (Burton et al., 2011).

$$a'(r) = a'_b(r)f(r) \tag{3.24}$$

To determine the new induction coefficient, one must balance the forces of the blades and the forces of the actuator disc. This is to equate the change of axial thrust and tangential torque of the elements with the change of axial and angular momentum passing through the annulus. Here C_x denotes the axial and C_y the tangential force coefficients.

$$\frac{a}{1-a} = \frac{\sigma_r}{4\sin^2\varphi}C_x \tag{3.25}$$

$$\frac{a'}{1-a'} = \frac{\sigma_r}{4\sin\varphi\cos\varphi}C_y \tag{3.26}$$

In Equation 3.26, on the right-hand side are the previously calculated data and on the left-hand side, the new coefficients are found. Furthermore, for high tip speed ratios, the wake may become turbulent. Consequently, the actuator disc theory will fail. From the actuator disk theory, a maximum thrust coefficient is found at $a = 0.5$. However, experiments proved higher thrust coefficients being possible above $a > 0.5$. For heavily loaded stream tubes a correction is therefore needed. Glauert approximated a correction for the thrust of a single actuator disc through a line fitting with experimental results. A comparison between the theory and measurements can be seen in figure 3.5.

The transition thrust coefficient and transition induction factor are defined as:

$$C_{Tl} = 1.816 \tag{3.27}$$

$$a_{Tl} = 1 - \frac{\sqrt{C_{Tl}}}{2} \tag{3.28}$$

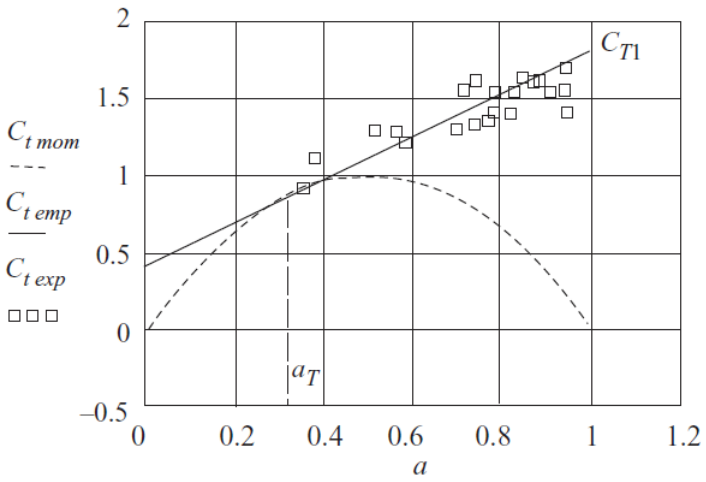

Figure 3.5: Comparison between the theoretical (Glauerts) and the measured C_T (Burton et al., 2011).

Then the new coefficient can be found through the C_T values calculated through the blade element forces and the following equation:

$$C_T = C_{Tl} - 4(\sqrt{C_{Tl}} - 1)(1 - a) \tag{3.29}$$

The induction factors are updated with the inflow angles and subsequent parameters until the convergence criteria are met.

3.2.3 Actuator Line Model (ALM)

The actuator line model is a model that captures the effects of each blade of the turbine individually while maintaining the simplicity of the BEM model. Unlike the BEM model, the actuator line model does not project the body forces of the turbine per annulus, rather it separates the forces per blade with a given azimuthal offset. This method is established by Jens Norkr Sørensen and Wen Zhong Shen (Sørensen and Shen, 2002). This method is vastly used in rotor aerodynamics to solve the 3-D unsteady flow fields.

The forces acting on the blades are computed using the blade element approach. The forces are projected on the $\theta - z$ plane (figure 3.6), where θ is the azimuthal position and z is the axial position. The basis for force calculation is 2-D aerofoil characteristics (Mikkelsen et al., 2007). These 2-D aerofoil characteristics often have to be corrected for 3-D implementation (Sørensen and Shen, 2002).

Figure 3.6, provides the orientation and the reference frame for a blade element of the rotor. The inflow velocity, i.e. relative velocity experienced by the rotating element, is given by,

$$V_{rel} = \sqrt{V_z^2 + (V_\theta - \Omega r)^2} \tag{3.30}$$

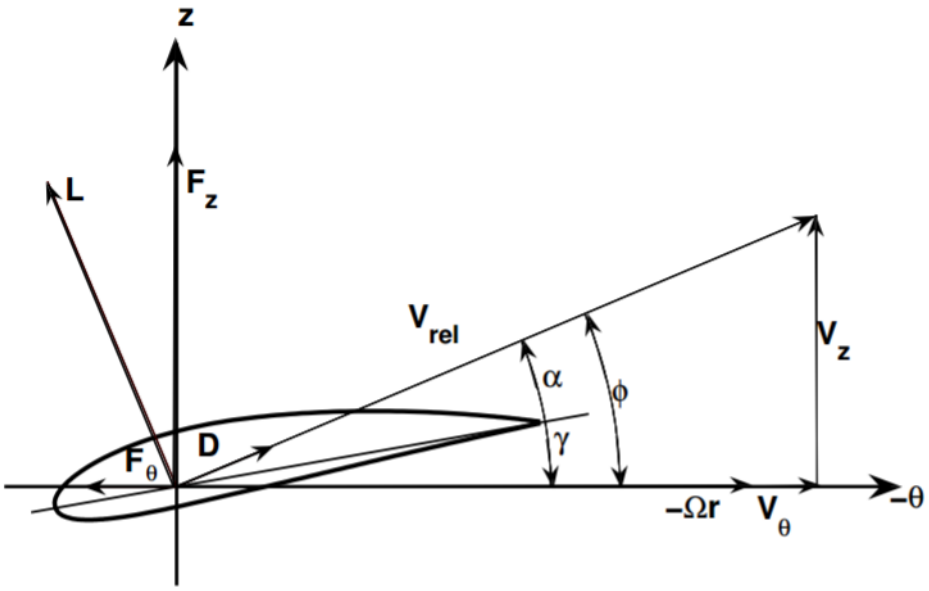

Figure 3.6: The orientation of velocity components for a blade element (Mikkelsen et al., 2007).

where, V_z is the axial velocity, Ω is the angular velocity, r is the local radius of the element, V_θ is the tangential velocity. The inflow angle between the relative velocity, V_{rel} and the plane of rotation is computed by,

$$\varphi = \tan^{-1}\left(\frac{V_Z}{\Omega r - V_\theta}\right) \tag{3.31}$$

Assuming the element has a geometric pitch of angle, γ, the angle of attack experienced by the blade is then,

$$\alpha = \varphi - \gamma \tag{3.32}$$

The angle of attack computed here is not corrected for induction from bound vortices (Mikkelsen et al., 2007). With the obtained angle of attack and the aerofoils characteristic data, the tangential and normal forces, for a unit span of the element with the local chord, c, can be computed.

$$f_{tan} = \frac{1}{2}\rho v_{rel}^2 c(C_L \sin\varphi - C_D \cos\varphi) \tag{3.33}$$

$$f_{norm} = \frac{1}{2}\rho v_{rel}^2 c(C_L \sin\varphi + C_D \cos\varphi) \tag{3.34}$$

The calculated forces are then applied to the mesh grid. Projection of the forces on to a single mesh point leads to singular behaviour (Sørensen and Shen, 2002). To avoid this behaviour, the blade forces are distributed away from the line elements in a 3-D Gaussian manner (Mikkelsen et al., 2007). This is done by taking the convolution of the computed forces and the regularisation kernel, η_ϵ.

$$f_\epsilon = f\eta_\epsilon \tag{3.35}$$

where, η_ϵ is defined by,

$$\eta_\epsilon(d) = \frac{1}{\epsilon^2 \pi^{\frac{3}{2}}} \exp\left[-\left(\frac{d}{\epsilon}\right)^2\right] \tag{3.36}$$

where, $d = |x - s\epsilon_i|$, is the distance between the grid centres and the position of the i^{th} line element. The concentration of the load is controlled by parameter ϵ. The final force distribution is represented by,

$$f_\epsilon(x) = \sum_{i=1}^{B} \int_0^R f(s)\eta_\epsilon(|x - s\epsilon_i|)ds \tag{3.37}$$

The regularisation is necessary to avoid singular behaviour by providing a smooth distribution of forces.

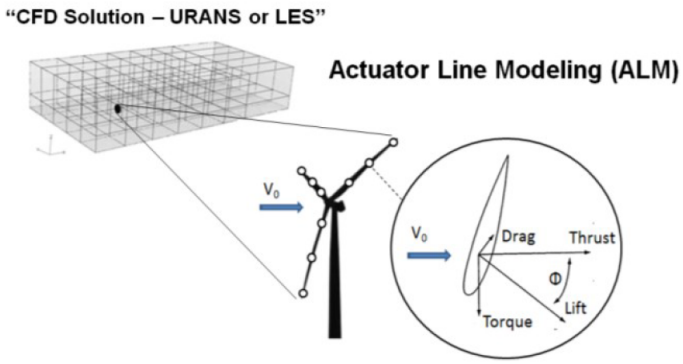

Figure 3.7: : Actuator-Line Method for modelling a wind turbine wake (Schmitz and Jha, 2015).

Schmitz and Jha, 2013, (Schmitz and Jha, 2015) applied the Actuator Line Model to an LES solver to model the wake of wind turbines and rotorcrafts. It is concluded that the ALM LES models reduced the costs of solving grids around Computer Aided Design (CAD) model (Schmitz and Jha, 2015). This reduced the accuracy of the flow over the geometry as it superimposed the actuator forces onto the mesh grid, however, the objective was to simulate the turbulence in the wake, which proved to be effective.

Having attained an insight into the flow and geometrical modelling, it is time to look at the flow characteristics induced in the wind turbine aerodynamics.

3.2.4 Validation of ALM for HAWT

The validation of the ALM for HAWT is carried out by Sarmast et al. (Sarmast et al., 2016) with respect to the MEXICO (Model Experiments in Controlled Conditions) experiment. An experimental rotor is tested in a $9.5 \times 9.5 m^2$ large-scale low-speed facility at the German-Dutch

Wind Tunnels (DNW). The model has a rotor diameter of $4.5m$ with 3 blades. The rotor blade has a cylindrical profile up to 4.4% span. The span from 11.8% to 40% has a DU91-W2-250 aerofoil profile, furthermore, the span from 50% to 62% has a RISO A1-21 aerofoil profile and the span from 72% to the tip has a NACA-64-418 aerofoil. The ALM model is created using the EllipSys3D Navier-Stokes solver. The smearing parameter is chosen to be $\epsilon = 2.5dr$ where dr is the local actuator resolution.The Navier Stokes equations are solved using LES computation. The computation is performed using two configurations, with and without the nacelle. Each blade is represented by 41 actuator points. The experimental data is recorded at $25\%, 35\%, 60\%, 82\%$ and 92% span.

The computations are carried out for inflow velocities of 10, 15 and 24 m/s with the rotational velocity of 425.1 rpm, and the pitch of the blade is set to $-2.3°$. The normal and tangential forces are computed on the blades for the three inflow conditions.

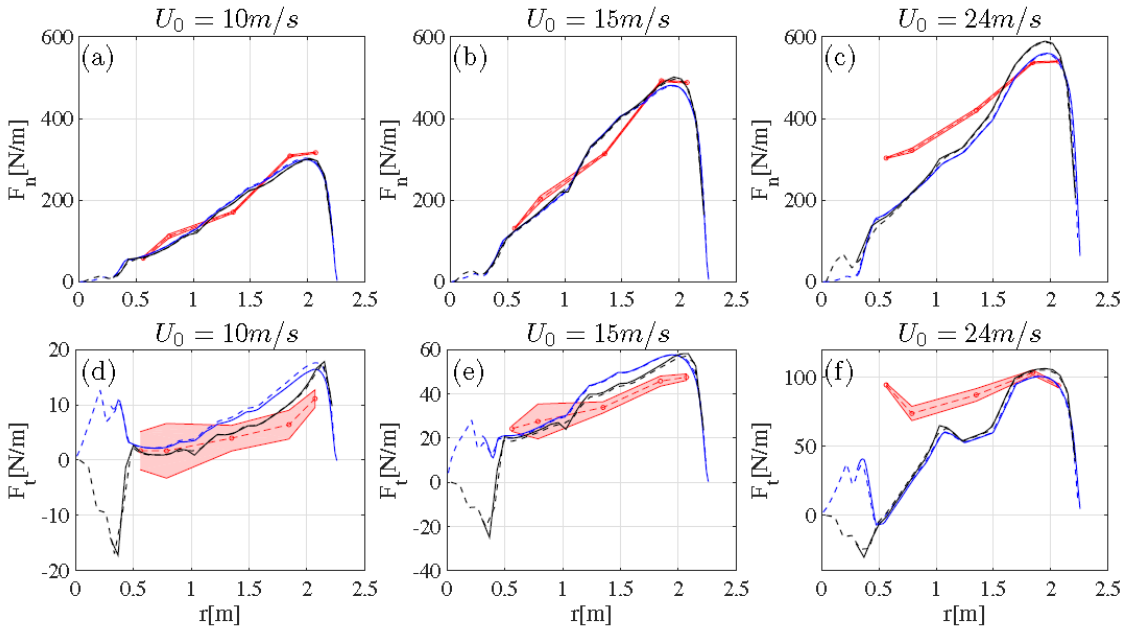

Figure 3.8: Normal force (F_n) and tangential force (F_t) distribution along the blade for inflow velocities of (a) $U_0 = 10m/s$, (b)$U_0 = 15m/s$ and (c) $U_0 = 24m/s$. The red dotted line represents results from the experiment. The red area shows the experimental uncertainty. The blue line represents the ALM in presence of hub and the dotted line represents the result in the absence of the hub. The black line represents the ADM in presence of the hub and the dotted line represents the result in absence of the hub (Sarmast et al., 2016).

Figure 3.8 shows that the model results are, in general, in agreement with the experimental results except for the measurements in the inboard part of the blade for higher inflow velocity. This disagreement is attributed to the under-prediction of stall due to the use of 2-D aerofoil data. It is also observed that the presence of the nacelle has a minimal effect on the loading on the inboard part of the blade. Figure 3.9 shows the wake developed by the ALM approach. The wake has the distinct root and tip vortices. It is shown that the vortical structures near

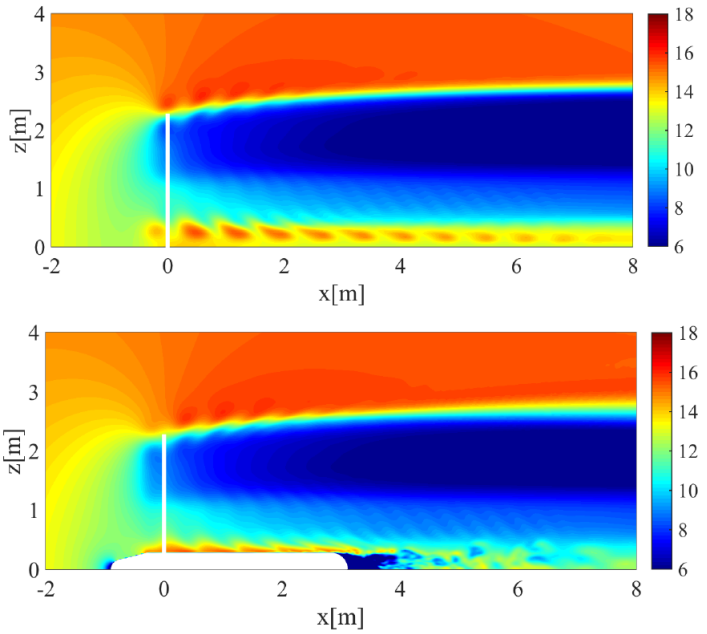

Figure 3.9: Contours of axial velocity for $U_0 = 15m/s$ inflow computed using the actuator line approach, (top) simulations in the absence of the nacelle and (bottom) simulation with the presence of the nacelle. The blade azimuthal position is set to be $\theta = 60°$ (Sarmast et al., 2016).

the root decay faster in presence of the nacelle due to their interaction with the hub.

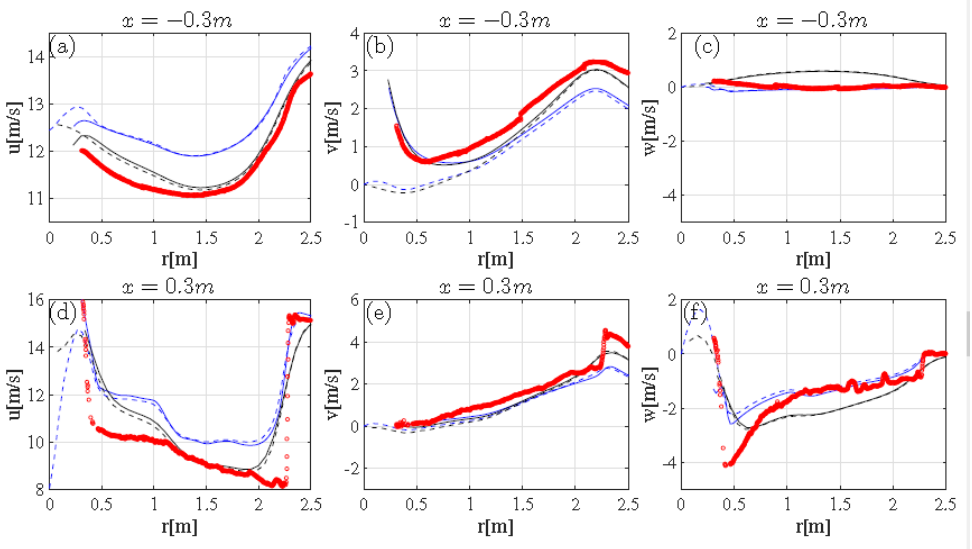

Figure 3.10: (a) Axial, (b) radial and (c) tangential velocities along the span at $x = -0.3m$ upstream and (d)-(f) represent the same components of velocities at $x = 0.3m$ downstream of the turbine at $U_0 = 15m/s$. The red dotted line represents results from the experiment. The blue line represents the ALM in presence of the hub and the dotted line represents the result in the absence of the hub. The black line represents the ADM in presence of the hub and the dotted line represents the result in the absence of the hub (Sarmast et al., 2016).

The ALM model overpredicts the axial velocities from PIV measurements upstream and downstream of the rotor. The velocities downstream of the rotor show three separate regions of induced velocities that correspond to the three different aerofoil profiles used. The tangential and the radial components are in agreement with the PIV measurements except in the inboard region. It is clear that including the hub in the computation improved the result.

Sarmast et al. conclude that the ALM computation, in general, agrees well with the experiments for the blade loading and the velocity components. They also conclude that the flow around the nacelle does not have an influence on the loading on the blade.

3.2.5 ALM for VAWT

The actuator line model, as discussed earlier, captures the effects of individual blade elements. Bachant et al. (Bachant et al., 2016a) developed an ALM model suited to vertical axis turbines. The turbine parameter definitions and orientation are shown in figure 3.11 and figure 3.12.

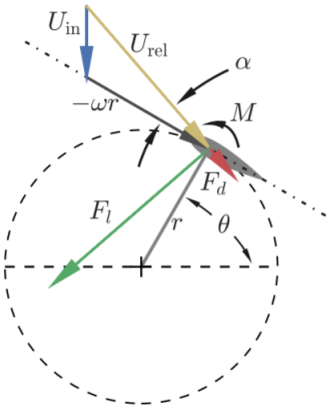

Figure 3.11: Representation of the incident velocities, and the forces acting on the blades of a vertical axis turbine (Bachant et al., 2016a).

The parameter that dictates the kinematics of a vertical axis turbine is the tip speed ratio,

$$\lambda = \frac{\omega R}{U_\infty} \tag{3.38}$$

where ω is the angular velocity of the turbine, R is the rotor offset from the axis of rotation and U_∞ is the free stream velocity incident on the turbine. The dynamic nature of the VAWT aerodynamics results in oscillations in the angle of attack as the blade rotates. The frequency of this unsteadiness can be represented as a dimensionless constant called the reduced frequency. The reduced frequency is linked to the tip speed ratio, as this parameter dictates the rate of oscillation.

$$k = \frac{\lambda c}{2R} \tag{3.39}$$

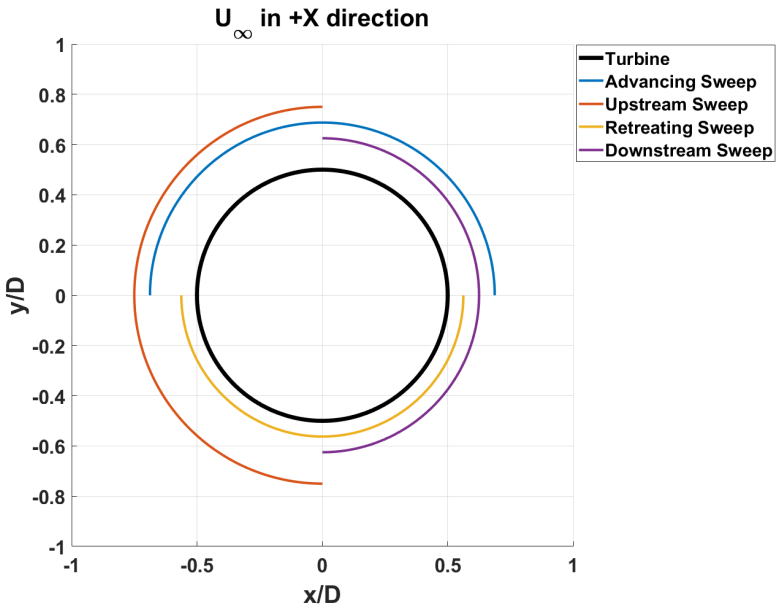

Figure 3.12: Blade sweep convention.

where, $\frac{c}{R}$ is the chord-to-radius ratio (solidity ratio). As a rule of thumb, the unsteady effects become significant when $k > 0.05$ (Bachant et al., 2016a).

Just as in the ALM model for the HAWT, this model requires aerofoil data. Bachant et al. suggested a database created by Sheldahl and Klimas (Sheldahl and Klimas, 1981). The database has a few limitations as some of the data is synthesised from other measurements (Bachant et al., 2016a). Having acquired the aerofoil data, it needs further corrections for dynamic stall, added mass, flow curvature correction and end effects.

Dynamic stall correction based on Mendoza et al. (Mendoza et al., 2016)

The dynamic stall corrections are implemented to account for the stall and partial separation induced due to the continuous oscillation of the angle of attack. In this case, the dynamic stall model considered is developed by Leishman and Beddoes in 1989 (Leishman and Beddoes, 1989). This model is later modified for low Mach number by Sheng et al. in 2008 (Sheng et al., 2008) and for VAWT by Dyachuk et al. in 2013 (Dyachuk et al., 2014). According to Mendoza et al. (Mendoza et al., 2016), the dynamic stall model is separated into three submodels: an attached flow model for unsteady linear loading, a separated flow model for non-linear loading and a dynamic stall model for loading induced by leading edge vortex. The first submodel, the unsteady attached model, takes circulatory and the impulsive loads into account. These loads depend on the time-dependent bound vortex. The coefficient of normal force due to circulations is represented as,

$$C_{N_n}^C = C_{N_\alpha} \alpha_{E_n} \tag{3.40}$$

where C_{N_α} is the slope of the static normal force coefficient and α_{E_n} is the equivalent angle

of attack. The equivalent angle of attack is then,

$$\alpha_{E_n} = \alpha_n + X_n + Y_n + Z_n \tag{3.41}$$

where α_n is the geometric angle of attack and X_n, Y_n and Z_n are the deficiency functions. The deficiency functions, X_n, Y_n, and Z_n, are derived empirically (Dyachuk et al., 2014). The n index denotes the time step. Due to the dynamic nature of the system, the pressure response lags behind the change in angle of attack, therefore the delayed angle of attack is,

$$\alpha'_n = \alpha_n - D_{\alpha_n} \tag{3.42}$$

The deficiency function D_{α_n} is given by,

$$D_{\alpha_n} = D_{\alpha_{n-1}} \exp\left(-\frac{\Delta s}{T_\alpha}\right) + (\alpha_n - \alpha_{n-1}) \exp\left(-\frac{\Delta s}{2T_\alpha}\right) \tag{3.43}$$

where T_α is an empirically derived time constant and Δs is the non-dimensional time-step.

$$\Delta s = 2\frac{|\vec{V_{rel}}|\Delta t}{c} \tag{3.44}$$

As the boundary layer separates, the flow reverses and a vortex is shed from the leading edge. The initiation of dynamic stall is determined by the critical angle of attack.

$$\alpha_{cr_n} = \begin{cases} \alpha_{ds_0} & |r_n| \geq r_0 \\ \alpha_{ss} + (\alpha_{ds_0} - \alpha_{ss})\frac{|r_n|}{r_0} & |r_n| < r_0 \end{cases} \tag{3.45}$$

where α_{ss} is the static stall onset angle, α_{ds_0} is the critical stall onset angle, r_0 is the reduced pitching rate and r_n is the reduced pitching rate and is defined as,

$$r_n = \frac{\dot{\alpha} c}{2|\vec{V_{rel}}|} \tag{3.46}$$

where α is the pitching rate of the aerofoil. The reduced pitching rate introduces the dynamic stall to the quasi-steady stall characteristic. The dynamic stall occurs when $|\alpha'| > \alpha_{cr}$.

As the flow separates, two effects come into play: trailing edge separation and leading-edge vortex convection (Mendoza et al., 2016). The separation at the trailing edge moves upstream towards the leading edge. There is a time-delay between the change in angle of attack and separation point moving upstream towards the leading edge, this is calculated by Kirchoffs approximation.

$$f'_n = \begin{cases} 1 - 0.4\exp\left(\frac{\alpha_1 - |\alpha'|}{S_2}\right) & |\alpha'| < \alpha_1 \\ 0.02 - 0.58\exp\left(\frac{\alpha_1 - |\alpha'|}{S_2}\right) & |\alpha'| \geq \alpha_1 \end{cases} \tag{3.47}$$

where f' is the delayed separation point, $_1$, S_1 and S_2 are constants found in (Dyachuk et al., 2014). Now superimposing the delay in pressure response and the response of boundary layer separation over the aerofoil, dynamic separation point, f'', is obtained.

$$f''_n = f'_n - D_{f_n} \tag{3.48}$$

where the deficiency function, D_{f_n} is defined as,

$$D_{f_n} = D_{f_{n-1}} \exp\left(-\frac{\Delta s}{T_f}\right) + (f_n - f_{n-1}) \exp\left(-\frac{\Delta s}{2T_f}\right) \tag{3.49}$$

Here T_f is an empirically derived time constant. The normal force coefficient before stall is

$$C^f_{N_n} = C_{N_\alpha} \alpha_{E_n} \left(\frac{1 - \sqrt{f''_n}}{2}\right)^2 \tag{3.50}$$

Once the aerofoil section has stalled, the leading edge vortex convects downstream, which increases the normal force as it moves towards the trailing edge. The normal force coefficient during dynamic stall is given as,

$$C^v_N = B_1(f''_n - f_n)V_x \tag{3.51}$$

Here B_1 and V_x are dependent on local Reynolds number and aerofoil. The total normal force is,

$$C_{n_{ds}} = C^f_{N_n} + C^v_N \tag{3.52}$$

The corresponding tangential force coefficient is given by Kirchoffs flow relation using the dynamic separation point (Mendoza et al., 2016).

$$C_{T_{ds}} = \eta C_{N_\alpha} \alpha^2_E (\sqrt{f''_n} - E_0) \tag{3.53}$$

where η and E_0 are obtained empirically. The validation for this model can be seen in (Mendoza et al., 2016).

Added Mass Correction

Added mass is the additional inertial added to the air due to acceleration of the blade through the air. Strickland et al. (Strickland et al., 1979) derived a correction for added mass by assuming a pitching flat plate in a potential flow. The normal and tangential force coefficients derived by Strickland et al. are,

$$C_{N_{AM}} = -\frac{\pi c \dot{U_N}}{8|\vec{U_{rel}}|^2} \tag{3.54}$$

$$C_{T_{AM}} = -\frac{\pi c \dot{\alpha} U_N}{8|\vec{U_{rel}}|^2} \tag{3.55}$$

These coefficients are added to the coefficients from the dynamic stall corrections to obtain the total, normal and tangential force coefficient.

$$C_N = C_{N_{AM}} + C_{N_{ds}} C_T = C_{T_{AM}} + C_{T_{ds}} \tag{3.56}$$

Now the obtained coefficients are used to compute the corresponding lift and drag coefficients.

$$C_l = C_N \cos\alpha + C_T \sin\alpha \tag{3.57}$$

$$C_d = C_N \cos\alpha - C_T \sin\alpha \tag{3.58}$$

Flow curvature corrections

As discussed earlier, a rotating blade in linear flow will have a varying angle of attack along its chord. Goude A., 2012 (Goude, 2012) derived a correction by assuming a flat plate revolving about an axis in potential flow. The resulting angle of attack of a blade section including the flow curvature effects is,

$$\alpha = \delta + \tan^{-1}\left(\frac{V_{abs}\cos(\theta-\beta)}{V_{abs}\sin(\theta-\beta)+\Omega R}\right) - \frac{\Omega x_0 c}{V_{ref}} - \frac{\Omega c}{4V_{ref}} \tag{3.59}$$

where δ is the blade section pitch angle, V_{abs} is the magnitude inflow velocity, θ is the azimuthal position of the blade, β is the direction of inflow velocity, x_0 is the chordwise position where the blade is attached with respect to quarter chord and V_{ref} is the reference flow velocity to compute the angle of attack.

Tip corrections

Just as the root and tip corrections are needed for the HAWT due to Helmholtz's 2^{nd} theorem, which states that the vortex line must form closed loops or they must extend to the boundaries, similar corrections for VAWT are required. According to the theorem, the lift distribution must drop to zero at the ends of the blade and it is a result of the bound vortex on the blade. Bachant et al. (Bachant et al., 2016a) uses Prandtl's lifting line theory to compute the angle of attack for an arbitrary circulation distribution as a function of the non-dimensional span, θ,

$$\alpha = \frac{2S}{\pi c(\theta)} \sum_{1}^{n} A_n \sin\theta + \sum_{1}^{n} n A_n \frac{\sin n\theta}{\sin\theta} + \alpha_0(\theta) \tag{3.60}$$

Here S is the total span, N is the number of blade elements and α_0 is the zero lift angle of attack. The Equation 3.60 is rearranged into a matrix form and unknown Fourier coefficients A_n are found. The resulting circulation distribution obtained is,

$$\Gamma(\theta) = 2SU_\infty \sum_{1}^{N} A_n \sin\theta \tag{3.61}$$

Using the Kutta-Joukowski theorem, the lift coefficient obtained is,

$$C_l(\theta) = -\frac{\Gamma(\theta)}{\frac{1}{2}cU_\infty} \tag{3.62}$$

The correction factor is obtained by normalising the obtained lift coefficient distribution.

$$F = \frac{C_l(\theta)}{C_l(\theta)_{max}} \tag{3.63}$$

Having understood the basic aerodynamic concepts for a wind turbine and the corresponding modelling techniques, it can be concluded that the best approach for studying the wake of a VAWT is using the combination of ALM with RANS and/or LES solver.

3.2.6 Validation of ALM for VAWT

The ALM model discussed in section 3.2.5 is validated by Bachant et. al. (Bachant et al., 2016a). For validation, the results from the ALM model, which is simulated using OpenFOAM with turbinesFoam library, are compared to those obtained from the UNH Reference Vertical Axis Turbine (UNH-RVAT) experiment (Bachant et al., 2016b).

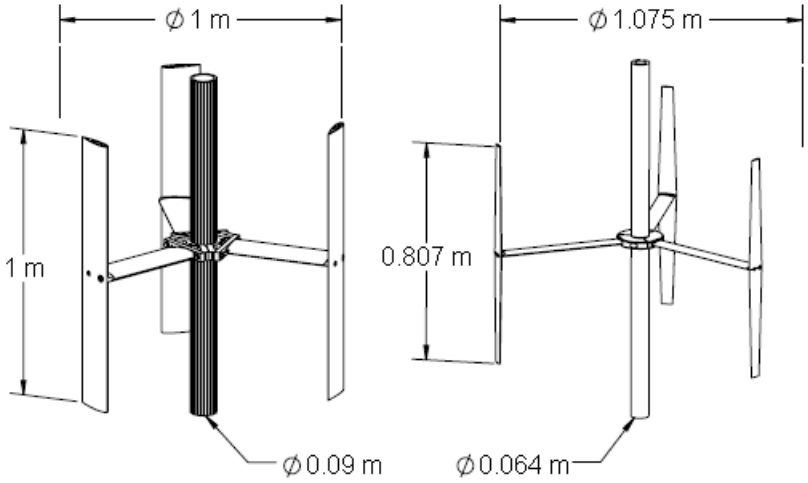

Figure 3.13: Turbines used for validation. (Left) UNH-RVAT and (right) RM2 (Bachant et al., 2016a).

The simulations are carried out using the ALM with RANS $k-\epsilon$ turbulence model. The flow domain is replicated to that of the tow tank experiment. The dimension of the experimental domain is: 3.66 m wide, 2.44 m tall, 1.52 m upstream and 2.16 m downstream with the inflow of 1 m/s (Bachant et al., 2016a). Temporal and spatial sensitivity studies are carried out for both the turbines at their optimal tip speed ratios.

The mesh is kept constant for the simulated cases. The resolution is scaled proportionally to the number of cells in x direction. Figure 3.14 shows that the models have a low temporal sensitivity, however, the spatial resolution dependence is crucial. The final spatial resolution chosen is $N_X = 48$ for the turbines. The time step selected for the UNH-RVAT simulation is 0.01 seconds.

The validation is carried out by comparing the power and the drag coefficient curves as a

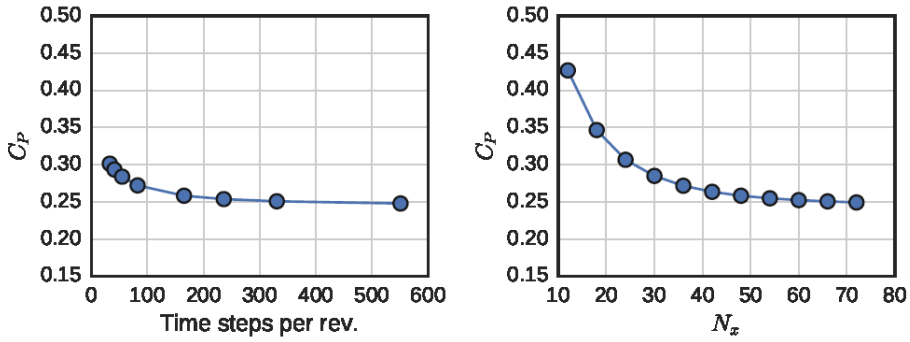

Figure 3.14: Temporal and Spatial sensitivity of the UNH-RVAT ALM-RANS model (Bachant et al., 2016a).

function of tip speed ratios from the simulations and the experiment. Figure 3.15 shows the C_P and C_D curves for the UNH RVAT RANS simulation compared to the experimental results.

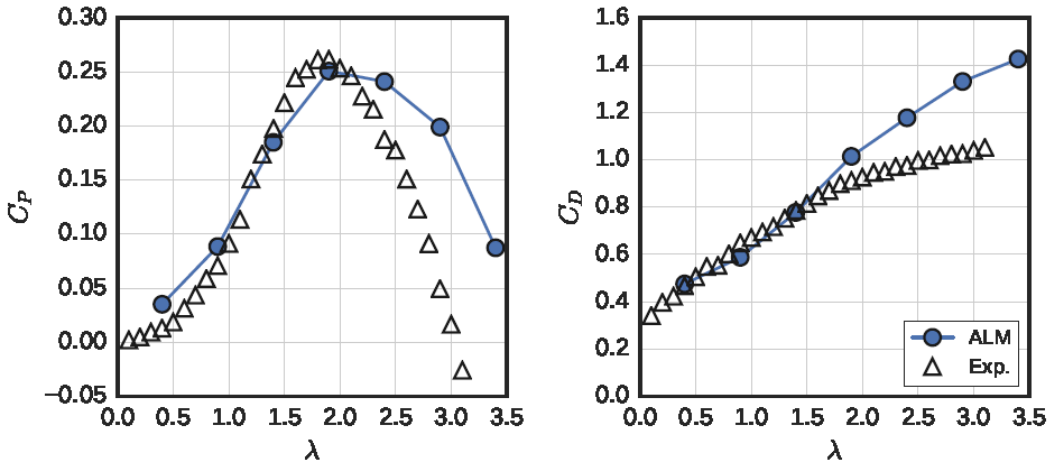

Figure 3.15: Power and drag coefficients for the UNH-RVAT using the ALM-RANS model compared to experimental results (Bachant et al., 2016a).

It is observed that the ALM successfully predicts the performance of the turbine up to the optimal tip speed ratio (peak of the curve), however at higher tip speed ratios, the performance is overpredicted. The over-prediction is attributed to a possible consequence of Leishman Beddoes dynamic stall model.

The averaged streamwise velocity and the turbulence kinetic energy along the centre plane

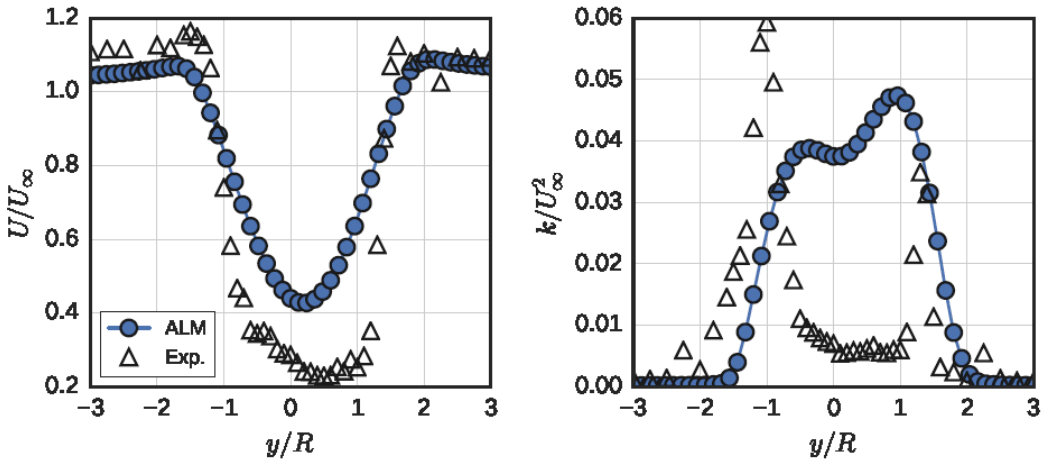

Figure 3.16: Averaged streamwise velocity and turbulence kinetic energy profiles for UNH-RVAT RANS compared to the experimental results (Bachant et al., 2016a).

of the turbine are plotted in comparison to the experiment in figure 3.16. Figure 3.16 shows that the turbulence kinetic energy profile does not agree closely with the experiment as the ALM dynamic stall model only projects force terms in the momentum equation and does not replicate the mechanism of shed vortices.

Bechant et al. also compares the performance of the two turbulence models. For an ALM LES simulation, the mesh resolution varies between 18-64 points per turbine diameter. The base mesh density is 16 points per meter with further refinement in the region of the turbine and the time step used is 0.002 seconds (Bachant et al., 2016a). The LES sub-grid scales are solved using Smagorinskys model. The averaged streamwise velocity and the turbulence kinetic energy along the turbine centreline are plotted.

By comparing the results from RANS and LES (figure 3.16 and figure 3.17), it is evident that the averaged streamwise velocity profile is captured more accurately by the LES model. However, the turbulence kinetic energy profile is not in good agreement with the experimental result, though the overall profile obtained is better than that by RANS. Bachant et al. concluded that the disagreement could be attributed to the sub-grid scale model and its effect on the stability of vortex structures. In conclusion, the ALM RANS model captured the performance of the UNH-RVAT turbine well at the tip speed ratios leading up to the optimal tip speed ratio. However, ALM LES model proved to be more accurate in capturing the wake characteristics. It is proposed that the subgrid-scale model is further developed (Bachant et al., 2016a).

Having understood the basic aerodynamic concepts for a wind turbine and the modelling techniques, it can be concluded that the best technique to study the wake deflection in VAWT is using the combination of ALM with RANS and/or LES solver. The initial simulations will be carried out using RANS as it is computationally less heavy. The simulations for this

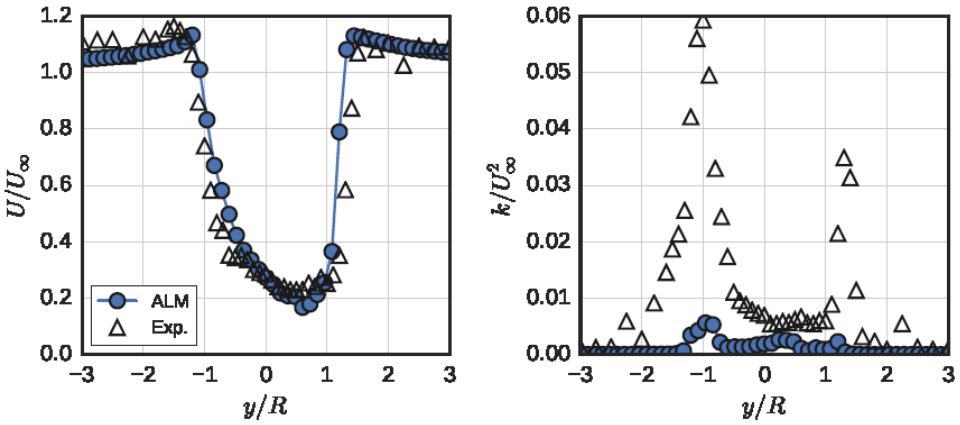

Figure 3.17: Averaged streamwise velocity and turbulence kinetic energy profiles for UNH-RVAT LES compared to the experimental results (Bachant et al., 2016a).

thesis will be carried out using the turbinesFoam library in OpenFOAM (see Appendix) by implementing the ALM with RANS/LES using finite volume discretization.

Chapter 4

Simulations and Results for Wake Deflection Study

In order to answer the research questions stated in section 1.2, simulations of the VAWT in various blade pitch angle configurations need to be carried out. In this section, the simulation parameters are discussed along with the results obtained from the simulations. As the prime objective of this thesis is to study the far wake of the VAWT and its deflection, it is indeed crucial to define a domain that incorporates the the far wake region. The simulation setup is discussed in the section below.

4.1 Simulation setup

The simulations are carried out using the turbinesFoam library in OpenFOAM version 4.1. The simulations use a 2-bladed H-rotor VAWT with a blade span of 20 m and a rotor diameter of 5 m. The aerofoil profile chosen for the blades is the NACA0015 with a chord of 0.25 m. The mast and struts of the turbine are not included in the simulations, though the turbinesFoam library provides the option to do so. To closely represent the results for a 2D case, the turbine has a high aspect ratio of $AR = \frac{h}{R} = 8$. The simulations are carried out with a time step of 0.01 seconds. The solution in the far wake converges under 110 seconds, however, the simulation results showcased here are that for 120 seconds of the simulation run. The check for convergence in the far wake is carried out by observing the velocity profile at the end of the domain over time.

The simulation domain has the dimension of $80 \times 50 \times 50$ metres. X-direction: -30 to 50 metres; Y-direction: -25 to 25 metres; Z-direction: -25 to 25 metres. The global mesh density is proportional to the chord length of the blade. This mesh is created by blockMeshDict on OpenFOAM. The entire working of the turbinesFoam and its coupling to OpenFOAM is described in Appendix A. On the global grid, the domain consists of 320 divisions along the

x direction, 200 division along the y direction, and 200 divisions along the z direction. In order to capture the details of the wake, the mesh is further refined in the wake region. This refinement is carried out using the snappyHexMeshDict. A local turbulence zone is defined in topoSetDict for refinement. The turbulence zone is refined to level = 2, therefore, each cell in this region is refined to 4^{level} (see figure 4.1). The refined grid extends from -3 m to 50 m in the x direction, -4 m to 4 m in the y direction, and -10 m to 10 m in the z direction.

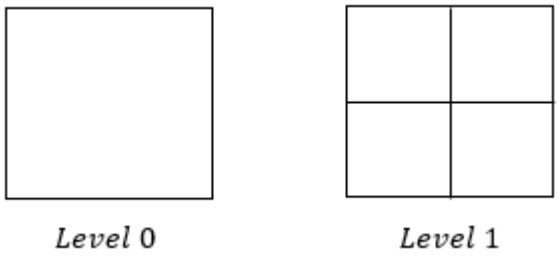

Figure 4.1: Mesh refinement levels for one mesh cell.

The flow direction is in the $+x$ direction. The turbine rotates counter-clockwise when viewed from the top ($+z$ axis). The domain has a uniform inflow of 1 m/s and the turbine has a tip speed ratio of 4.5. The results of the simulations are discussed in the sections that follow. The cases run in the scope of the thesis are simulated without the implementation of the dynamic stall model.

The hypothesis tested in this thesis is that the basic principle behind the wake deflection is the deflection of the thrust vector on the turbine by inducing a cross force component. In case of a HAWT, the wake deflection is attained by physically reorienting the turbine axis to divert the thrust vector. The relative angular deflection between the turbine axis and the incoming wind leads to deflection of the thrust vector. As the VAWT inherently has the advancing and retreating effects with the azimuthal position of the blades, the thrust vector is also deflected as a function of azimuthal position. Therefore, the wake is deflected if there exists a net unbalance of forces orthogonal to the wind direction. The results from the simulation will provide further clarity on this phenomenon. Before the simulations are carried out, the model is validated against other models. The comparison of ALM (turbinesFoam) with other models is discussed in section 4.2.

4.2 Comparison of ALM to existing models

The validity of the actuator line model used here is checked by its comparison to the existing models, which are used to compute the blade loading and the total turbine performance. The comparison is made as per the selected parameters in Ferreira et.al. (Ferreira et al., 2014) which compares six models using different approaches to the actuator and induction system. The models used for comparison are the Code for Axial and Crossflow TUrbine Simulation (CACTUS), Actuator Cylinder model (AC), Unsteady Two-dimensional Vorticity

Aerodynamics model (U2DiVA), (ARDEMA2D), Multiple Streamtube Model (MST), and Double-Multiple Streamtube Model (DMST).

CACTUS is a 3D free vortex code where the blades are modelled with a lifting line approximation. Blades are represented by a bound vortex over the individual elements. The wake is modelled by the vortex lattice method. The induced velocities are computed using the Biot-Savart law. The code is created by Murray and Barone, 2011 (Murary and Barone, 2011).

The ARDEMA2D is a free vortex particle code that uses a conformal mapping approach to simulate the blade elements. It is created by AREVA based on the works of Deglaire et al. (Deglaire, 2010) (Deglaire et al., 2008).

The Actuator Cylinder Model (ACM) is a derivation of the actuator disc method for VAWT where the actuator area coincides with the swept area of the turbine blades. The blade forces are added as body forces to the fluid solver. The model is developed by Madsen et al. (Madsen, 1982).

U2DiVA is a free wake code that uses the panel method to simulate the blade as a distribution of doublets and sources. This code is created by Ferreira, 2009(Ferreira, 2009) based on the formulation by Katz and Plotkin, 2000 (Katz and Plotkin, 2000).

The Multiple Streamtube Model is a BEM model where the turbine is discretized into multiple stream tubes in the crosswind direction. Each streamtube is considered to be independent of its neighbouring streamtubes. This model assumes a single induction value per streamtube, which is used to compute the time-averaged performance (Strickland, 1975). The double multiple streamtube model divides the aforementioned streamtube into upstream and downstream regions. It assumes this configuration as two actuators working in tandem (Laplin, 1975). The setup of the test is discussed in the next section and the comparison of the models is discussed in section 4.2.2.

4.2.1 Test case setup

The test case for the model comparison is carried out with a twin-blade H-Rotor profile. The aerofoil under consideration is the NACA0015. Parameters selected for variation are the solidity of the rotor and the blade pitch angle. The output parameters selected for comparison are the rotor power and the thrust coefficients, which require the rotor's streamwise and tangential induction factors, the angle of attack, and the force distribution for the individual blade sections.

Potential flow and steady Bernoulli's pressure equations are used to keep the flow conditions similar amongst the models. for this reason, the ALM model is executed without the coupling of the dynamic stall model. The polar data is set to the following definition (Ferreira et al., 2014),

$$c_l(\alpha) = 2\pi 1.11 \sin\alpha \tag{4.1}$$

$$c_d(\alpha) = 0 \tag{4.2}$$

The ALM model, being a 3D model is tested with a high aspect ratio. The high aspect ratio is required to reduce the effects of tip vortices on the central actuator line element to conform to a 2-D comparison. The turbine is operated at a tip speed ratio of $\lambda = 4.5$ and solidity ratios of $\sigma = 0.1, 0.14$ with the blade pitch angles of $\beta = 0°, -3°, 3°$. The variation of the solidity ratio is implemented by changing the blade chord.

Table 4.1: Test cases for comparing the models.

Cases	λ	σ	β	**Compared Parameters**
A	4.5	0.1, 0.14	$0°$	$C_P, C_T, a, a_\perp, \alpha, F_{tan}, F_{norm}, F_{st}$
B	4.5	0.1	$-3°, 0°, 3°$	$C_P, C_T, a, a_\perp, \alpha, F_{tan}, F_{norm}, F_{st}$

A brief description of each model is provided in Ferreira et al. (Ferreira et al., 2014). As for the comparison of the models, the performance of the turbine is under study, and not the resulting wake. Therefore, the mesh is scaled to the blade chord for the ALM at solidity ratio of $\sigma = 0.1$.

4.2.2 Comparison of results

In this section, the results of power performance and blade loading from the ALM model are compared to the existing models. First, the rotor performance coefficients comparison is done amongst different models for test case B. The comparison of the induction factors and blade forces is discussed later. The results compare the turbine thrust coefficient, turbine power coefficient, turbine thrust coefficient normalised by that of the $\beta = 0°$ case for $\beta = -3°, 3°$ and turbine power coefficient normalised by that of $\beta = 0°$ case for $\beta = -3°, 3°$.

Table 4.2: Comparison of the turbine performance parameters from the test case B.

Model	C_T			C_P			$\frac{C_T}{C_{T_{\beta=0°}}}$		$\frac{C_P}{C_{P_{\beta=0°}}}$	
$\beta[°]$	$-3°$	$0°$	$3°$	$-3°$	$0°$	$3°$	$-3°$	$3°$	$-3°$	$3°$
MST	0.92	0.92	0.92	0.55	0.55	0.55	1.00	1.00	1.00	1.00
DMST	1.02	0.87	0.63	0.70	0.60	0.50	1.017	0.73	1.18	0.84
AC	0.90	0.89	0.89	0.59	0.59	0.60	1.00	1.00	0.99	1.02
U2DiVA	0.87	0.89	0.90	0.55	0.56	0.57	0.98	1.02	1.01	0.98
CACTUS	0.86	0.86	0.87	0.58	0.57	0.56	1.00	1.02	1.01	0.98
ARDEMA2D	0.90	0.92	0.94	0.61	0.63	0.65	0.98	1.02	0.97	1.03
ALM	0.89	0.87	0.86	0.56	0.54	0.50	0.989	0.99	1.03	0.92

The effect of a change in fixed blade pitch angle on the turbine performance coefficients is small for all models except the DMST. This is attributed to the fact that the DMST model computes the actuation on the two halves of the azimuthal sweep in tandem, which does not consider the net effects between the actuators (the effect of the downstream actuator on the upstream one) due to the addition of forces caused by a change in blade pitch angle.

The ALM model underestimates the performance coefficients when compared to the other models. This is attributed to underestimation of the inflow velocity at the blade chord in the ALM (discussed in section 4.3). The graphs that are shown in figures 4.2, 4.3, 4.4, and 4.5, are the comparison between the models. The parameters compared are the same as the ones mentioned in table 4.1. The angle of attack, α, the lift coefficient, C_l, the drag coefficient, C_d, and the turbine thrust coefficient, C_T, distribution is obtained directly from the model. The remaining parameters are computed from the parameters obtained from the model. The streamwise induction factor is obtained as follows,

$$a = 1 - \frac{u_{st}}{U_\infty} \tag{4.3}$$

where u_{st} is the streamwise component of the inflow velocity. The tangential induction factor is computed as,

$$\omega T = (1 + a_\perp)\lambda; \omega R = |u_{in}| \cos\phi \tag{4.4}$$

$$a_\perp = \frac{u_{in_x} \cos\theta + u_{in_y} \sin\theta}{\omega R} \tag{4.5}$$

The angle of attack output from the ALM includes the flow curvature correction. However, this correction is only implemented to obtain the effective lift and drag coefficients. The corrected angle of attack, however, does not reflect the physical angle of attack of the blade element with respect to the inflow velocity. Therefore, in the comparison study, the angle of attack presented is obtained by simply negating the flow curvature correction from the output angle of attack from the ALM. The force components are obtained from the resulting lift and drag coefficients from the ALM. The lift and the drag forces are computed with respect to the inflow velocity.

$$L = C_l \frac{1}{2} \rho c L_{elem} |u_{rel}|^2 \tag{4.6}$$

$$D = C_d \frac{1}{2} \rho c L_{elem} |u_{rel}|^2 \tag{4.7}$$

However, the force coefficients presented in figures 4.2, 4.3, 4.4, and 4.5 are normalised by the factor,

$$\frac{1}{2} \rho \lambda^2 U_\infty^2 c \tag{4.8}$$

The factor in equation 4.8 corresponds to a unit blade length. The output lift and drag coefficients from the ALM are associated with a single actuator line element. Therefore, when different components of the forces are computed using the coefficients, the length of the actuator line element becomes irrelevant.

The force coefficients are then computed as,

$$C_{tan} = (C_l \sin\alpha - C_d \cos\alpha) \tag{4.9}$$

$$C_{norm} = (C_l \cos\alpha + C_d \sin\alpha) \tag{4.10}$$

$$C_x = (-C_{tan} \cos\theta + C_{norm} \sin\theta) \tag{4.11}$$

$$C_y = (C_{tan} \sin\theta + C_{norm} \cos\theta) \tag{4.12}$$

Here, C_x corresponds to the streamwise force coefficient, C_{norm}, corresponds to the normal force coefficient, and C_{tan}, to the tangential force coefficients.

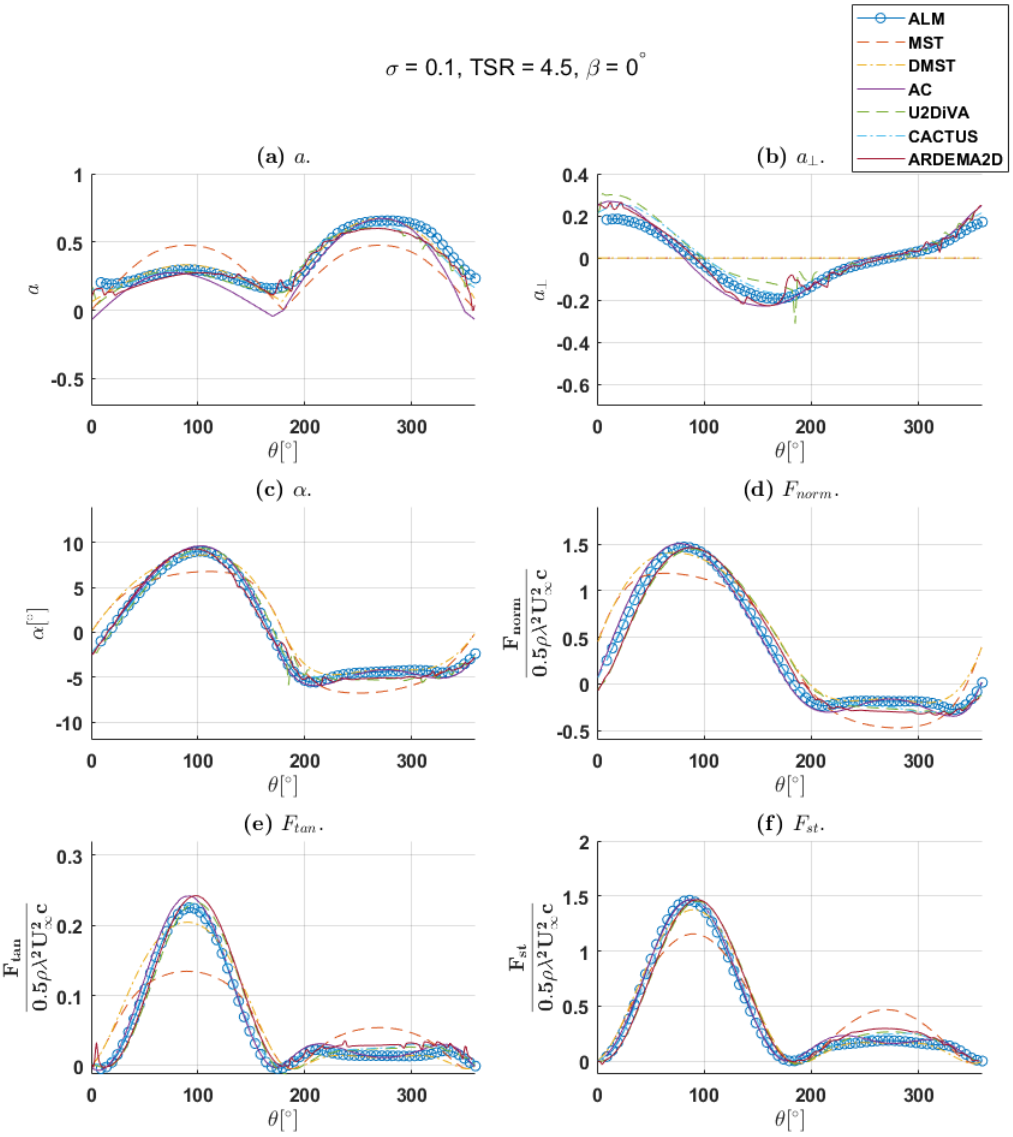

Figure 4.2: Results test case A, $\beta = 0°$,$\lambda = 4.5$,and $\sigma = 0.1$. Induction factors a and $a_\perp$, angle of attack, α, and loading on blade in normal direction F_{norm}, tangential direction F_{tan} and aligned with U_∞ (stream tube direction), F_{st}.

The results in figure 4.2, show that the ALM output using the turbinesFoam library is in good agreement with the other vortex based models for estimation of blade loadings and

induction of the velocity components. The major disagreements exist when the ALM results are compared to the MST and DMST models. As stated earlier, this difference lies in the fact that the MST models compute the averaged effects of the upstream and the downstream blade sweep, and the DMST model computes the effects for the upstream and downstream sweep separately, however, the effect of the downstream sweep on the upstream sweep is not considered. This can be noticed in the symmetric behaviour of the MST parameters. The DMST results show an improvement over MST results but tend to show a deviation from the other models. In the comparison of the tangential induction distribution, it is observed that the result from both stream tube models are firmly zero. This is consistent with the models' assumption of mutually independent stream tubes.

The results from figures 4.3 and 4.4 show that the data from the ALM is in good agreement with the other models. The main deviation noticed is in figure 4.4, with blade pitch angle of $\beta = 3°$. The tangential force coefficient computed by the ALM is shown to be slightly underestimated when compared to the other models. The reason for this deviation can be attributed to an error in the velocity sampling method and/or force projection kernel. The deviation from the stream tube models is as expected. The results from figure 4.5 show a good agreement between the ALM and the other models. In this case, the tangential force coefficient is slightly underestimated by the ALM when compared to the other models. It is clear that the actuator line model predicts the blade forces with reasonable accuracy, though improvements to velocity sampling technique is suggested. It is, therefore, a good tool to simulate the wake resulting from the turbine since the forces are projected as the body force term in the Navier-Stokes equations. In the next section, the reasons for the deviation of results for ALM are discussed.

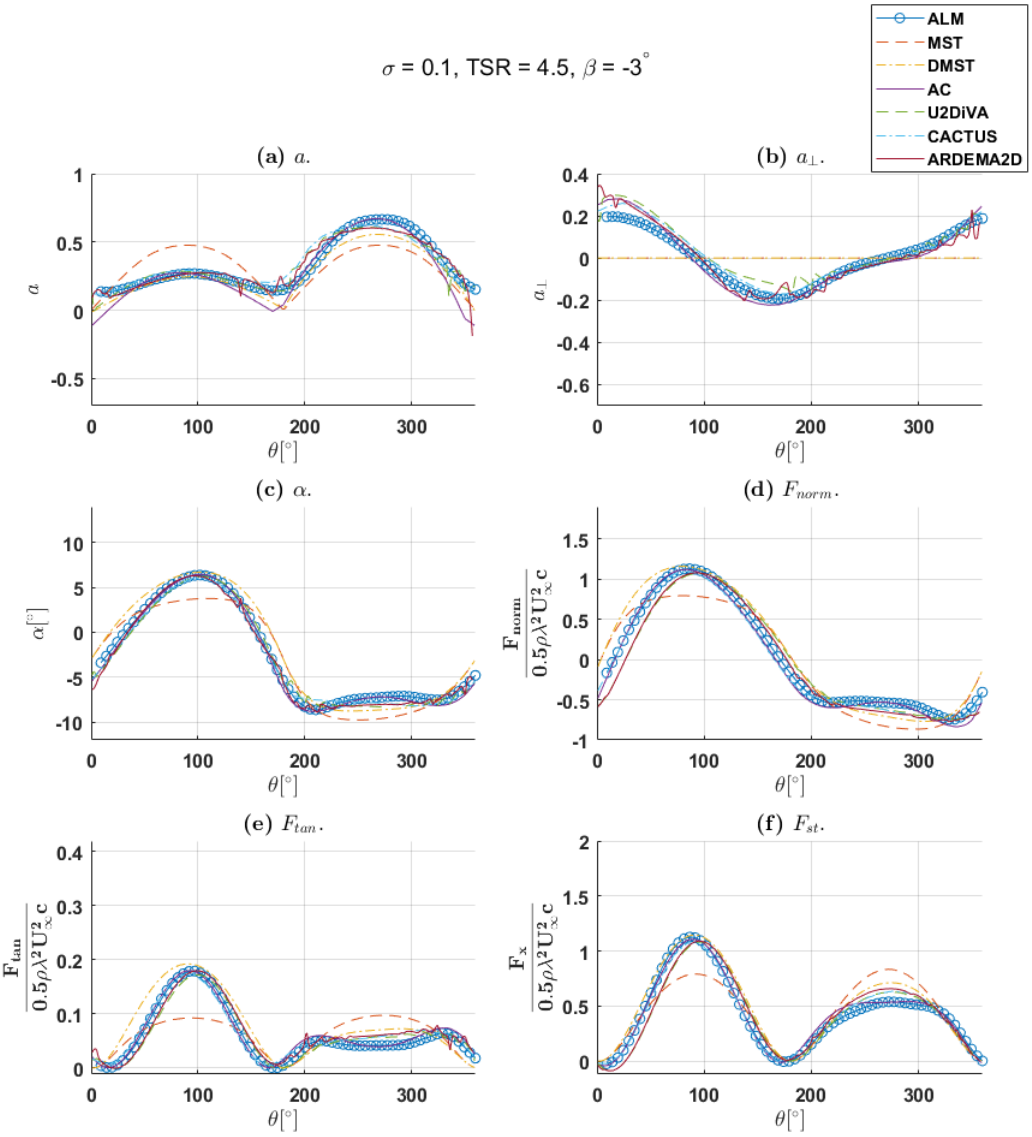

Figure 4.3: Results test case A, $\beta = -3°$,$\lambda = 4.5$,and $\sigma = 0.1$. Induction factors a and $a_\perp$, angle of attack, α, and loading on blade in normal direction F_{norm}, tangential direction F_{tan} and aligned with U_∞ (stream tube direction), F_{st}.

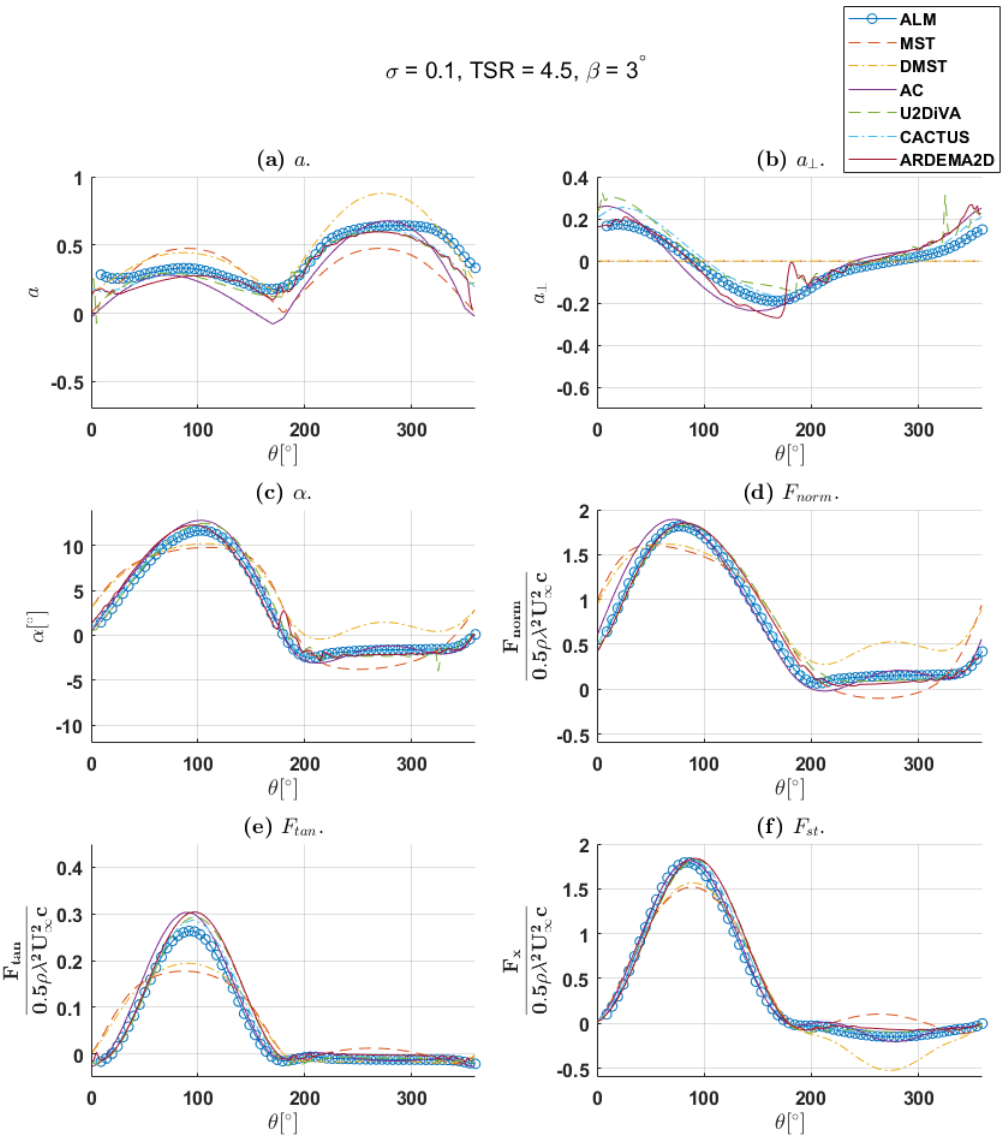

Figure 4.4: Results test case A, $\beta = 3°$,$\lambda = 4.5$,and $\sigma = 0.1$. Induction factors a and $a_\perp$, angle of attack, α, and loading on blade in normal direction F_{norm}, tangential direction F_{tan} and aligned with U_∞ (stream tube direction), F_{st}.

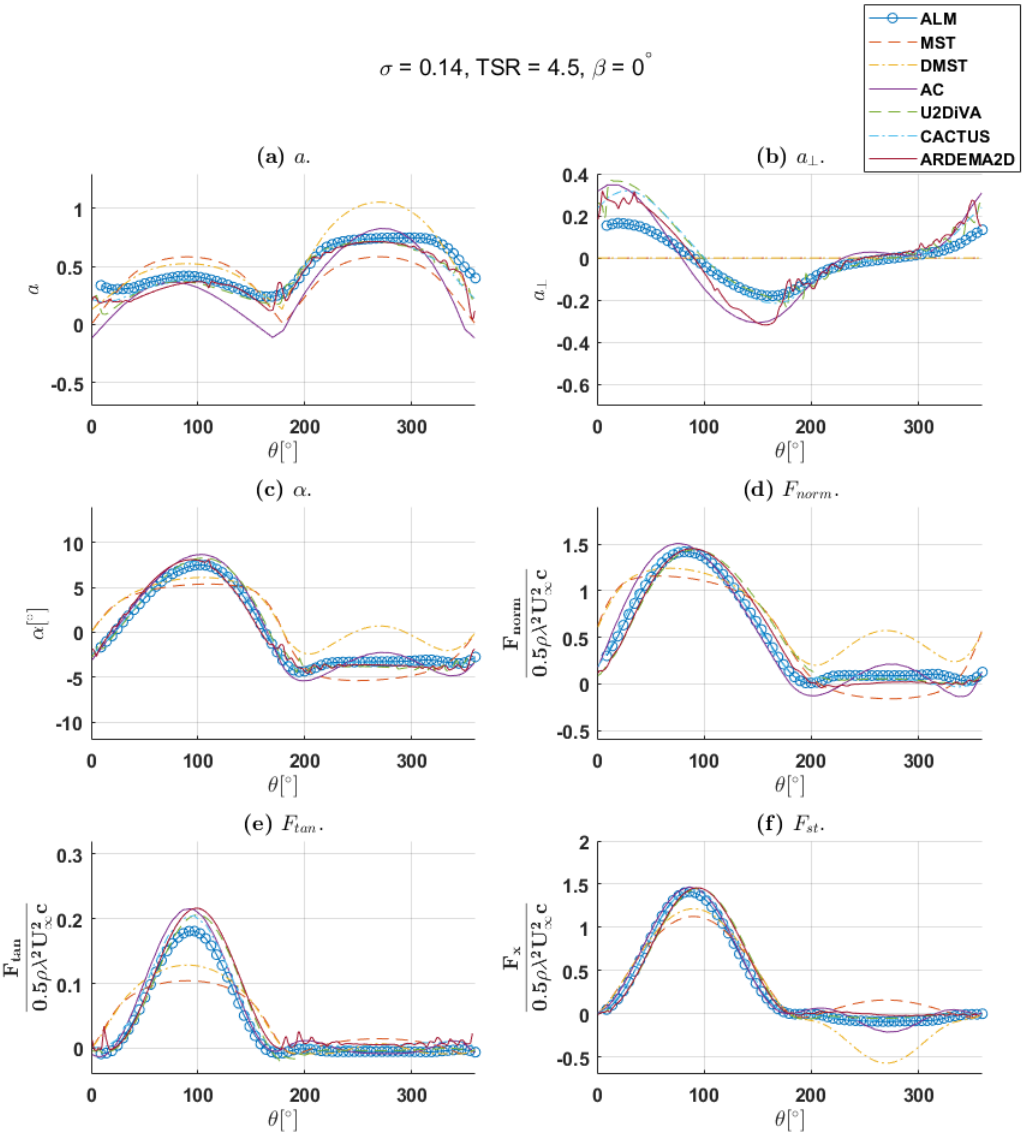

Figure 4.5: Results test case A, $\beta = 0°$,$\lambda = 4.5$,and $\sigma = 0.14$. Induction factors a and $a_\perp$, angle of attack, α, and loading on blade in normal direction F_{norm}, tangential direction F_{tan} and aligned with U_∞ (stream tube direction), F_{st}.

4.3 Deviation of results

As seen from figure 4.4 and figure 4.5, the results from the actuator line model show deviation in angle of attack and force estimations. The actuator line model also shows a drastic degradation in power coefficient with an increasing blade pitch angle as seen in table 4.2. This is, however inconsistent with the results from Ferreira and Scheurich, 2013 (Ferreira and Scheurich, 2013). Ferreira et al., 2013 inferred that changing the blade pitch angle does not significantly influence the power coefficient. In this section, the reasons for the aforementioned deviations will be discussed.

The actuator line model works in tandem with the Navier-Stokes equations. The flow field is computed by the Navier-Stokes equations. The velocity near the actuator line elements is sampled and put into the actuator line model as the inflow velocity. The inflow velocity vector along with the geometrical parameters are used to compute the angle of attack. The angle of attack estimation is the prime parameter in the ALM. The angle of attack is used to determine the forces imparted by the actuator line elements on the flow using the airfoil's polar data corresponding to the angle of attack at every time step. Therefore, it is of paramount importance that the inflow velocity vector and hence the angle of attack be computed accurately. The sensitivity of the ALM to the accuracy of the inflow velocity vector often results in amplification of error with time. This is due to the fact that any error in the inflow velocity vector would reflect on the forces imparted by the actuator line elements and in turn the error in the forces projected on the flow would further change the velocities in the flow field. This results in amplification of error with time.

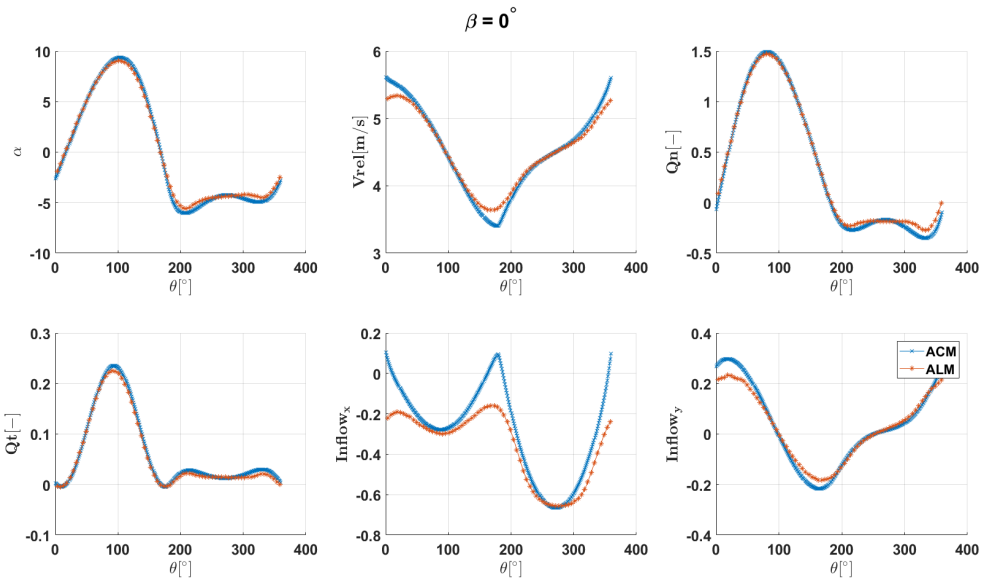

Figure 4.6: Comparison of results from the ACM and the ALM.

The deviation in the inflow velocity noticed in figure 4.6 where the inflow velocity is sampled from the ALM and the ACM, results in the deviation in angle of attack, and hence, the forces. It is also important to keep in mind the differences in the modelling techniques. The ACM is a 2D vorticity model, whereas the ALM is a 3D momentum model. The momentum is conserved in the 2D plane of the ACM; however, this is not true for the 2D plane extracted from the ALM for comparison. In the case of ACM, the wake is created by the shedding trailing edge vortices and vortical induction on the flow field, whereas the wake in the ALM is generated by the Navier-Stokes equation. However, the difference in the output from the two models should be comparable. The significant deviation in the inflow velocity distribution for the ALM when compared to the ACM suggests an error in the velocity sampling technique and/or the force projection.

The inflow velocity for the ALM is obtained by sampling the velocity in the velocity field near the actuator line element. It is difficult to point at a single sampling position to attain the inflow velocity since the node of the mesh may not be present at the exact location of the inflow velocity. The inflow velocity is, therefore, interpolated to approximate the correct inflow position. This leads to an error in the inflow velocity sampled.

Due to the interdependency of the inflow velocity and the force projection, an error in either will contribute to the error in the other. As the forces computed by ALM are required to be projected over a number of mesh cells, the force distribution is guided by the projection kernel,

$$\eta = \frac{1}{\epsilon^3 \pi^{\frac{3}{2}}} \exp\left[-\left(\frac{|\vec{r}|}{\epsilon}\right)^2\right] \tag{4.13}$$

The kernel in Equation 4.13 is dependent on the Gaussian function with the Gaussian width, ϵ, and the distance from the projection point at the quarter chord, $|\vec{r}|$ (Bachant et al., 2016a). The Gaussian width, ϵ, can be computed with respect to the mesh resolution, chord length, and/or the momentum thickness (Bachant et al., 2016a). The maximum of the three values is chosen as the Gaussian width. For the simulations carried out in the scope of this thesis, the Gaussian width is computed with the mesh resolution. The forces projected on the flow are therefore dependent on the mesh resolution rather than the blade dimensions. It is difficult to satisfy the meshing and temporal resolution conditions mentioned in (Jha et al., 2014) as well as maintaining a constant relation between the number of actuator line elements and the mesh cells while keeping the computation time feasible. This results in a slight deviation from the force projected in the case of the real turbine blade. The errors in force projection will reflect in the induced velocities, which in turn will change the inflow velocity. As seen in the validation results, these errors accumulate and result in a net error of approximately 1° angle of attack.

The forces computed by the ALM, therefore, deviate from those obtained from the ACM. The deviation in the computed tangential forces results in a reduction in coefficient of power as the blade pitch angle is increased. This, however, is inconsistent with the case of potential flow in (Ferreira and Scheurich, 2013). It is therefore crucial that the study of wake deflection, with pitching blades, be carried out with blade pitch angles of $|\beta| \leq 3^\circ$. This error can, however, be reduced by further advancements in inflow velocity sampling techniques and force projection kernels.

4.4 Improved Velocity Sampling

In order to improve the accuracy of the results, Dr. Anders Goude (Senior Lecturer at Dept. of Engineering Sciences, Division of Electricity, Uppsala Univerity) implemented a new sampling technique in the turbinesFoam library. He considered the inflow velocity vector as an average of the velocity at a number of axisymmetric points surrounding the quarter chord position at a certain radial distance.

Two new factors are introduced to determine the vector of the sampling points, i.e. the number of sampling points and the radial distance between the sampling points and the quarter chord position. The sampling radius is linearly proportional to the width of the Gaussian function, ϵ, used for force projection.

$$R = N \times \epsilon \tag{4.14}$$

where, R is the sampling radius, N is an arbitrary constant, and ϵ is the width of the Gaussian function used in the force projection kernel. Since the radius is dependent on ϵ, it depends on the same three factors that define the Gaussian width for force projection. The three factors are the momentum thickness, chord length and the mesh size. The maximum of these three factors is attributed to ϵ (Mendoza et al., 2016). Equation 4.15 shows the dependency.

$$\epsilon = max\left[\frac{cC_D}{2}, 4\sqrt[3]{V_{cell}}, \frac{c}{4}\right] \tag{4.15}$$

where, c is the chord, C_D is the drag coefficient, and V_{cell} is the volume of the cell.

Dr Anders Goude carried out a further study into the sensitivity of sampling radius and the number of sampling points. The suitable combination for this thesis is a sampling radius of 2ϵ and 20 sampling points.

The simulations for blade pitch angle of $\beta = 0°$ and $\beta = 3°$ are carried out again with the new sampling techniques. The results are compared again with those from other models. Figure 4.7 and figure 4.8 show the comparison for blade pitch angles of $\beta = 0°$ and $\beta = 3°$.

On comparing figure 4.2 vs figure 4.7, and figure 4.4 vs figure 4.8 it is observed that the angle of attack distribution is in good agreement with the other models when the new sampling technique is used. The force coefficients also show a good agreement with the other model. The deviation is seen in the induction fields. The axial induction shows maximum deviation from the other models.

However, as this thesis deals with creating a cross force component for wake deflection, the deviation in the induction field result is not considered. The new results also show an improvement in the power coefficient predictions as higher blade pitch angles no longer show a rapid degradation in power coefficient. This is observed in table 4.3.

Now that the improved velocity sampling technique is implemented, a study can be carried out to gain an insight into wake deflection in VAWT. Before focussing the behaviour of the

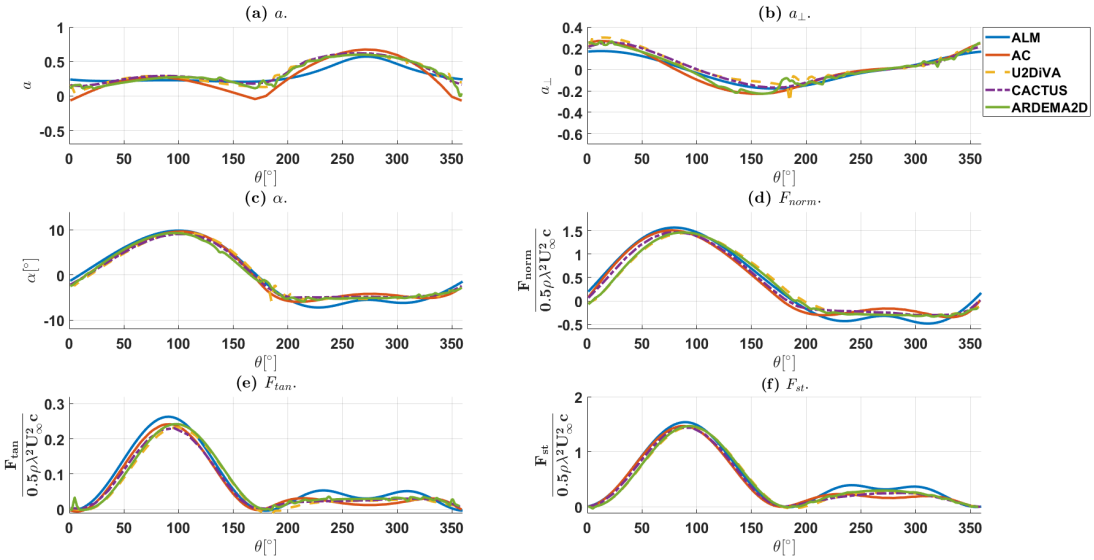

Figure 4.7: Results test case A with new sampling technique, $\beta = 0°$,$\lambda = 4.5$,and $\sigma = 0.1$. Induction factors a and $a_\perp$, angle of attack, α, and loading on blade in normal direction F_{norm}, tangential direction F_{tan} and aligned with U_∞ (stream tube direction), F_{st}.

Table 4.3: Comparison of turbine performance parameters from test case B with new sampling technique.

Model	C_T			C_P			$\frac{C_T}{C_{T_{\beta=0°}}}$		$\frac{C_P}{C_{P_{\beta=0°}}}$	
	$-3°$	$0°$	$3°$	$-3°$	$0°$	$3°$	$-3°$	$3°$	$-3°$	$3°$
MST	0.92	0.92	0.92	0.55	0.55	0.55	1.00	1.00	1.00	1.00
DMST	1.02	0.87	0.63	0.70	0.60	0.50	1.017	0.73	1.18	0.84
AC	0.90	0.89	0.89	0.59	0.59	0.60	1.00	1.00	0.99	1.02
U2DiVA	0.87	0.89	0.90	0.55	0.56	0.57	0.98	1.02	1.01	0.98
CACTUS	0.86	0.86	0.87	0.58	0.57	0.56	1.00	1.02	1.01	0.98
ARDEMA2D	0.90	0.92	0.94	0.61	0.63	0.65	0.98	1.02	0.97	1.03
ALM	0.0	0.85	0.85	0.0	0.59	0.589	0.0	0.99	1.00	0.99

wake and hence its deflection, it is crucial to clearly define the terms wake and wake deflection. This is discussed in the following section.

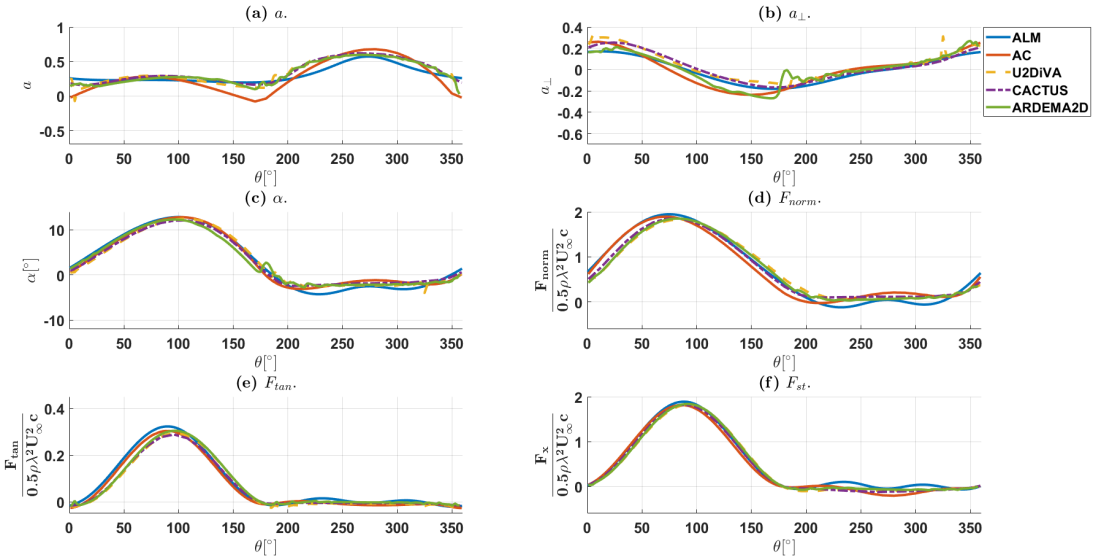

Figure 4.8: Results test case A with new sampling technique, $\beta = 3°$,$\lambda = 4.5$,and $\sigma = 0.1$. Induction factors a and $a_\perp$, angle of attack, α, and loading on blade in normal direction F_{norm}, tangential direction F_{tan} and aligned with U_∞ (stream tube direction), F_{st}.

4.5 Wake Deflection

The wake is defined as the region of momentum deficit behind a body in a flow. It is, therefore, clear that the wake consists of lower velocity downstream of the turbine when compared to the freestream. Thus, one way to define wake deflection would be *the locus of points of maximum velocity deficit downstream of the turbine.*

As seen from section 4.2.2, the induction over blade sweep is not symmetric. This can lead to an asymmetric wake. It is, therefore, important to create a definition of wake deflection that considers not only the position of the maximum velocity to determine the extent of deflection, but also the takes the wake expansion into account. This is important as even though the point of maximum velocity deficit may be sufficiently deflected, the resulting wake expansion could undermine the overall wake deflection.

The wake deflects and expands downstream of the turbine, therefore in order to consider the velocity deficit as well as the wake expansion, a new definition of wake deflection is created. The new wake deflection is defined as *the locus of the points of averaged velocity deficit at a distance downstream.*

According to this definition, the average velocity of the wake is considered for wake deflection. Assume a velocity profile at a certain distance downstream as shown in figure 4.9. The point of maximum velocity deficit is positioned at Y. The velocity at point Y is U_{PMVD}, where PMVD stands for the Point of Maximum Velocity Deficit. Now in order to consider the Point

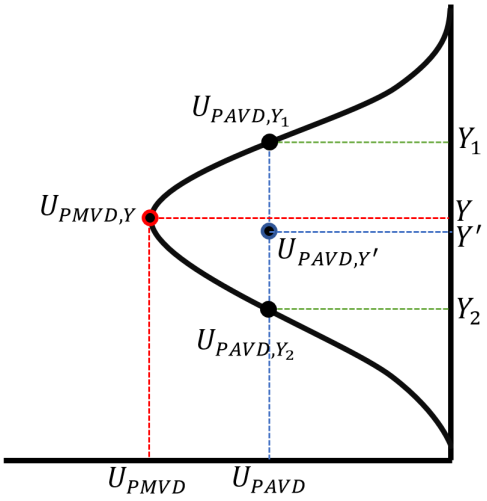

Figure 4.9: Point of averaged velocity deficit.

of Averaged Velocity Deficit (PAVD), the averaged velocity deficit is computed as follows.

$$U_{PAVD} = \frac{1}{N}\sum_{1}^{N} U(y) \tag{4.16}$$

where N are the number of sampled points on the velocity profile and $U(y)$ is the velocity distribution along the y axis. It is clear that the point of averaged velocity deficit will appear in two y positions on the velocity profile. One point will appear above Y and the other, below. The y positions for the following point are considered to be Y_1 and Y_2 respectively. The deflection of the averaged velocity deficit point is taken to be the mean y position between Y_1 and Y_2.

$$Y' = \frac{Y_1 + Y_2}{2} \tag{4.17}$$

where Y' is the deflection for the point of averaged velocity deficit. This definition takes the wake expansion into account with the U_{PAVD} term which depends on the averaged value of the velocity profile. A wider wake for a particular maximum velocity deficit will have a lower averaged velocity deficit when compared to that of a narrow wake. The position of Y' will also depend on the shape of the velocity profile. If the wake expansion occurs unevenly, then the position of Y' will have a bias towards the side of higher averaged velocity deficit with respect to the y position of the maximum velocity deficit. This point is especially important since the velocity profiles along the y axis are asymmetrical for a VAWT.

In the next section, the results using the improved velocity sampling technique are discussed. First, a base case is established with a $\beta = 0°$ blade pitch angle configuration. Thereafter, further cases with increasing blade pitch angles are simulated to see the corresponding effects in the wake and the wake deflection.

4.6 Results for a VAWT with a blade pitch angle $\beta = 0°$

Before trying to achieve wake deflection, it is important to first set a reference case and observe the behaviour of the corresponding wake. A simulation with constant 0° pitch angle is carried out and its wake is observed alongside the blade loadings as a function of its azimuthal position.

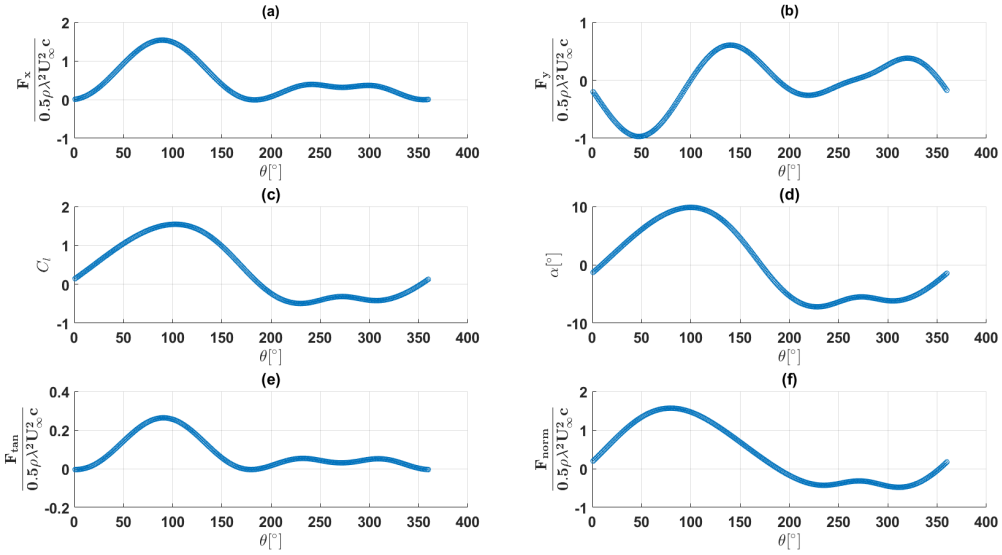

Figure 4.10: Blade loadings on VAWT blade with a 0° pitch angle.

Figure 4.10 shows the blade loading on a VAWT blade with 0° pitch angle. The cyclic loading of a VAWT is clearly evident. The forces experienced in the x direction is concurrent with the advancing and retreating effects expected. However, the y direction force distribution is very interesting and important. It is seen that there exists an asymmetry in the forces. According to the hypothesis, the asymmetric force distribution along y direction should result in the deflection.

It can be noticed in figure 4.11 and figure 4.12 that the wake of the VAWT, though ever so slightly displaced, remains centred. At various distances downstream, the wake expands as expected. The small displacement observed is due to the asymmetric force distribution along the y direction that results in a very small net force in the y direction. The force projections along streamwise and crossflow direction are shown in figure 4.13.

The force projections provide a clearer picture of the forces acting on the actuator line along its azimuthal sweep. It also provides a relative comparison between the scale of the corresponding force components along the azimuthal sweep. Figure 4.13 shows that the VAWT inherently has an asymmetry in the crossflow forces (y direction). This asymmetry, however, is very

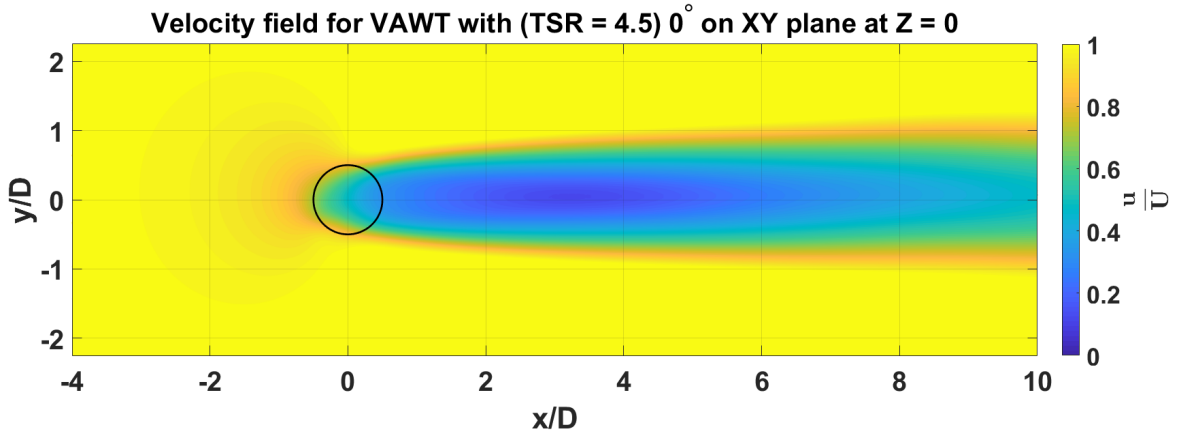

Figure 4.11: Velocity field for a VAWT with 0° pitch angle on the XY plane at Z =0.

small to clearly reflect in the far wake of the turbine. The near wake, however, shows a slight deflection from its origin as seen in figure 4.12. A clearer representation of the effect of the force projection on the wake can be attained through the velocity profiles at various distances, downstream of the turbine. A centrally aligned wake will have the maximum velocity deficit along the centreline of the turbine. A deflection will be reflected through the displacement of the maximum velocity deficit along the crossflow direction, as well as the displacement of the averaged velocity deficit.

The velocity profiles along the y axis shown in figure 4.14 clearly displays the slight deflection in the wake and its expansion as the wake progresses downstream. The velocity profile in the near wake region is almost symmetric as the near wake is strongly influenced by the blade loading. In the mid-wake section, the velocity profiles are almost symmetric (evident by the overlapping of PMVD and PAVD) as the wake is far enough from the blades to have any direct effect on the velocity profile. The far wake region shows an asymmetry in the velocity profile, this is attributed to the fact that in the far wake region the vorticity domain is diffusing, which leads to the wake becoming unstable due to an increase in momentum exchange with the freestream.

Figure 4.15 shows that the turbulence profile is quite axisymmetric. The near wake position shows a lower turbulence kinetic energy, as the near wake is dominantly influenced by the blade motion. In the far wake, the wake is guided by viscous diffusion, which is concurrent with the increase in the turbulence level. The turbulence intensity reduces further downstream as the wake begins to recover the momentum deficit, from the freestream. The trailing vortices from the two blades are evident from the streaks in the turbulence KE field, marking the diffusion of the vortices as those progress downstream.

Figure 4.16 highlights the trailing vortices from the turbine. An interesting observation is that the strength of the vorticity is asymmetric. The advancing blade faces a higher velocity. It, therefore, generates greater lift and sheds vortices with circulation proportional to change in its bound vortex, adhering to the Kutta-Joukowski theorem. This asymmetry in the net

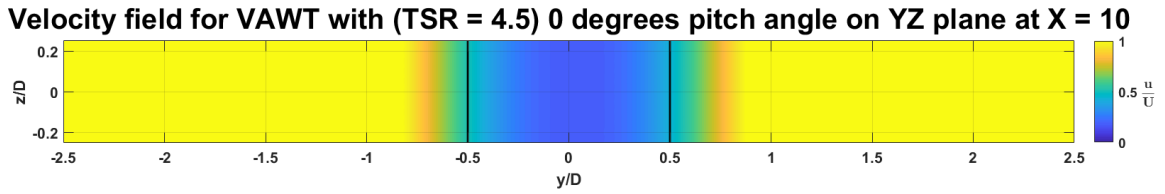

(a)

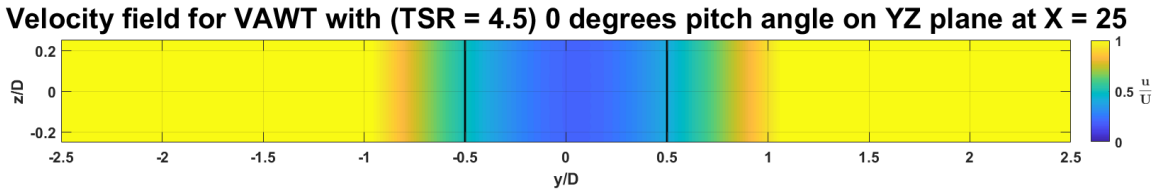

(b)

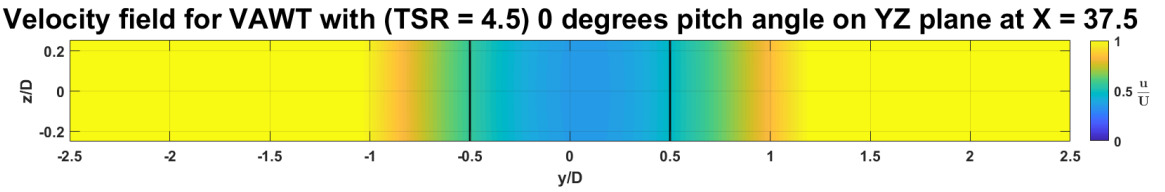

(c)

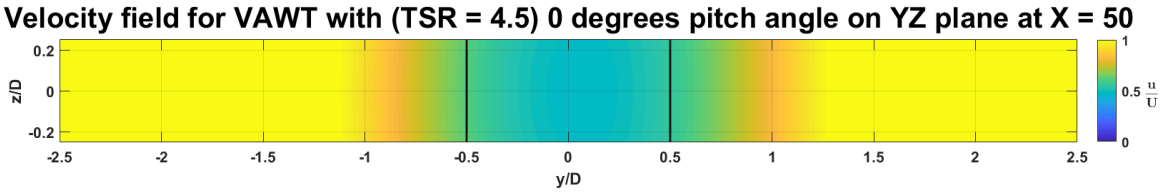

(d)

Figure 4.12: Velocity fields for a VAWT with 0^circ pitch angle on the YZ plane at (top to bottom) x/D = 2, 5, 7.5, 10.

bound circulation on the blade for one rotation contributes to the slight wake deflection observed in figure 4.11. The vorticity continues to diffuse downstream, leading to momentum recovery in the wake. The vorticity field helps visualise the wake domain in the flow, as the momentum deficit is contained within. The simulations carried out with increasing pitch angles show more prominent deflection in the wake as seen in section 4.7.

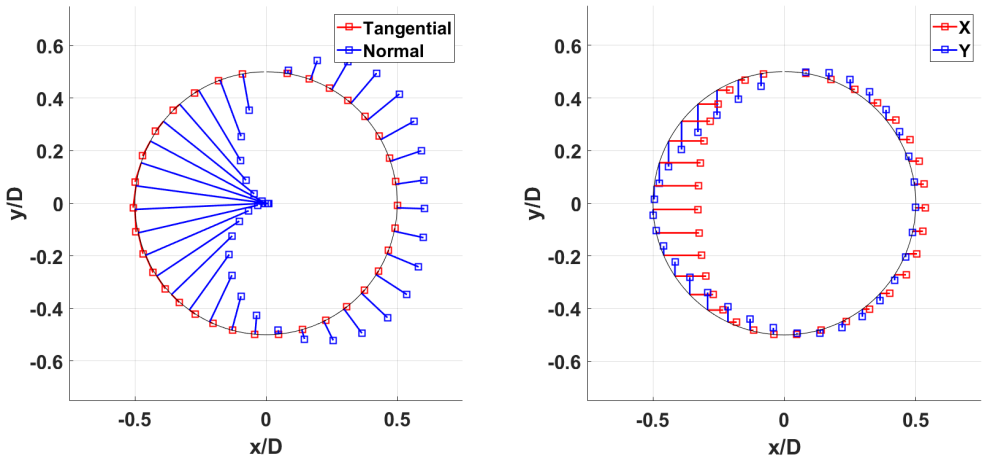

Figure 4.13: Force projection along the azimuthal sweep for a VAWT with the blade pitch configuration of $\beta = 0°$.

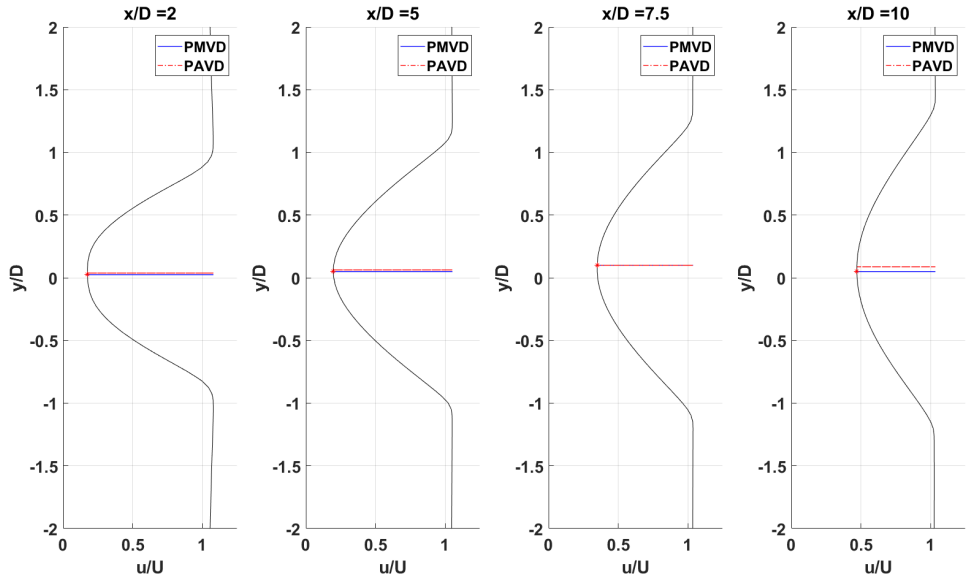

Figure 4.14: Wake velocity profiles at various distances downstream of a VAWT with a $0°$ pitch angle.

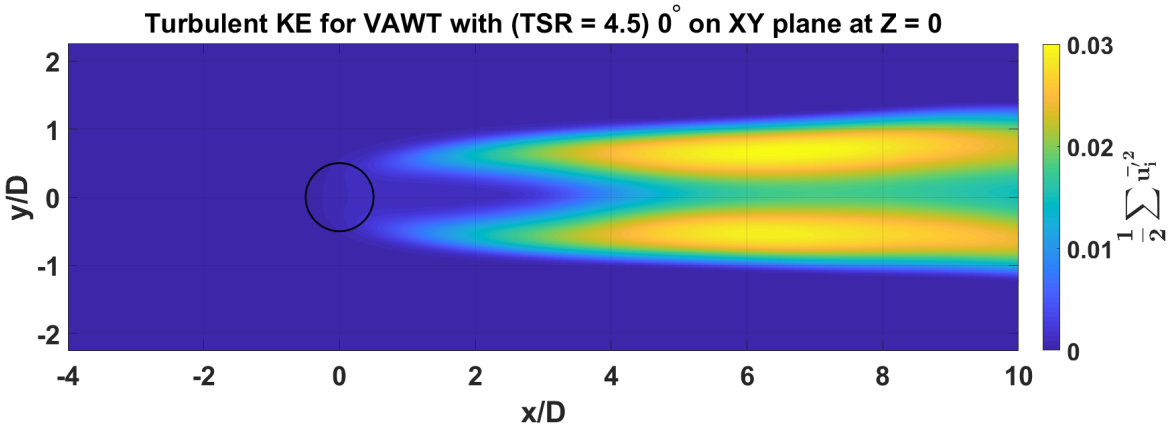

Figure 4.15: Turbulent KE field for a VAWT with a $0°$ pitch angle on the XY plane at Z = 0.

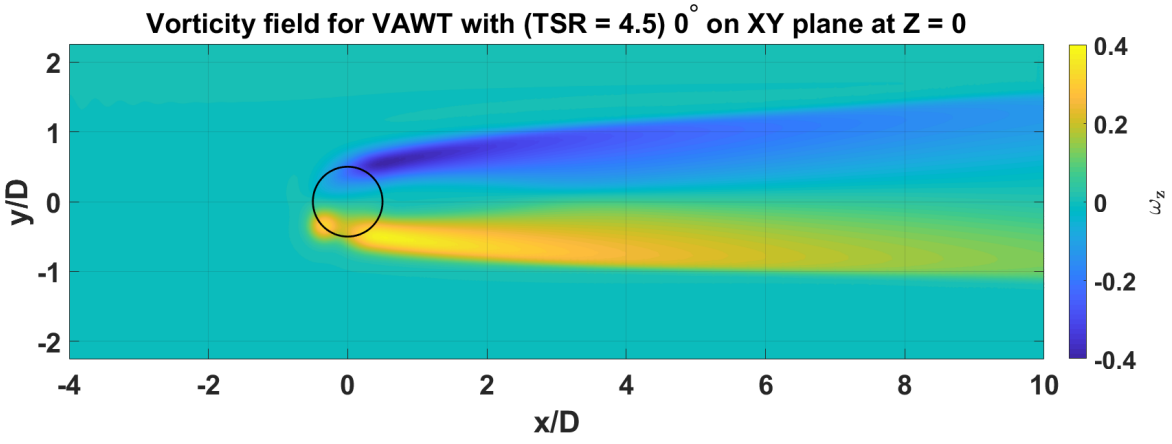

Figure 4.16: Vorticity field for a VAWT with a $0°$ pitch angle on the XY plane at Z = 0.

4.7 Results for a VAWT with a blade pitch angle $\beta = 3°$

As the reference case is established with $\beta = 0°$, a simulation for an increased blade pitch angle is carried out for $\beta = 3°$. This case is simulated with the same mesh, flow, and turbine parameters as the reference case with the only difference in the fixed pitch angle of the blades. The pitching convention is defined as positive when the leading edge of the blade is pitched towards the radial centre. The results from this simulation are compared to the reference case.

First, the blade loading and angle of attack distribution of the two cases are compared, as seen in 4.17.

It is interesting to see in figure 4.17, that the angle of attack distribution as has merely shifted higher in the magnitude, proportional to the fixed blade pitch angle. The same is reflected in the lift coefficient distribution. The blade loading in the normal direction experiences an increase in the force along the entire azimuthal sweep. However, the force distribution in the tangential direction highlights and interesting behaviour. In the tangential direction, there is an increase in loading in the upstream sweep of the turbine, however, during the downstream sweep, the blade loading recovery is reduced. The blade loading results are consistent with Ferreira and Scheurich, 2014 (Ferreira and Scheurich, 2013). As a result of the tangential loading recovery in the downstream sweep of the turbine, the power coefficient of the turbine sees a negligible deviation from that of the reference case (see figures 4.13 and 4.18).

The forces in the x and y direction are compared to study the net force imparted on the flow in the streamwise and cross flow direction. The behaviour of the force coefficient in the x direction is similar to that of the tangential force coefficient, which is evident from table 4.4.

Table 4.4: Relative force and power coefficient for a VAWT for $0°$ and $3°$ blade pitch angles.

Pitch angle, $\beta[°]$	$\frac{C_x}{C_{x_0}}$	$\frac{C_y}{C_{x_0}}$	$\frac{C_P}{C_{P_0}}$
0	1.00	0.129	1.00
3	1.002	0.293	0.996

Since the total force has to be conserved from moving from the blade's reference frame (tangential-normal) to freestream reference frame ($x - y$), the net force coefficient in the y direction should show an increase in the case of higher blade pitch angle as the net normal force coefficient increases for the case of higher blade pitch angle. The net increase in the cross force contributes to deflecting the wake. The force distribution can be seen in both frames of reference in figure 4.18

The net cross force provided causes the wake to deflect in the $+y$ direction. Figure 4.19 shows the velocity profiles at increasing distance downstream of the turbine when compared to the reference case.

According to Ferreira and Scheurich 2014 (Ferreira et al., 2014), the near wake is governed

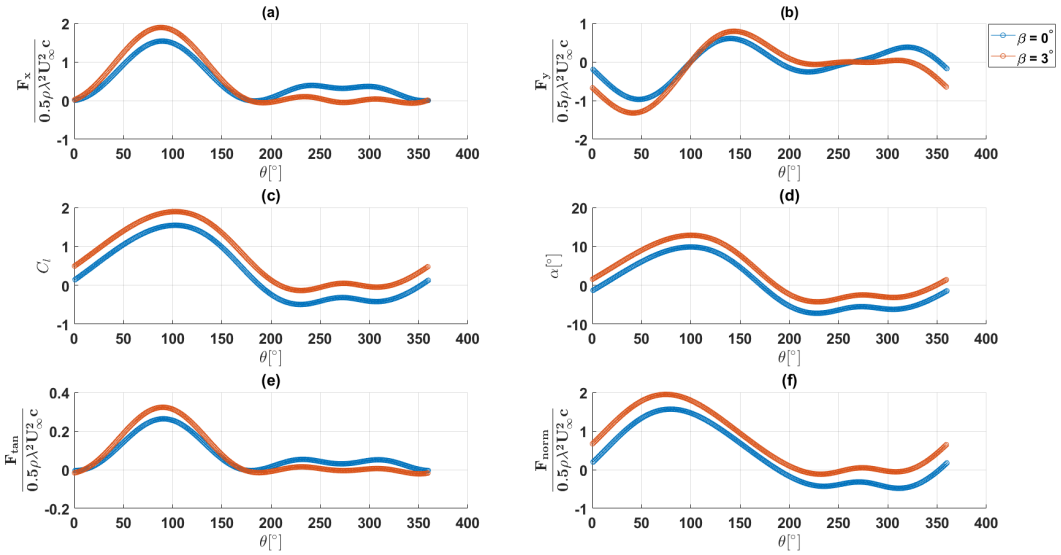

Figure 4.17: Blade loading comparison for a VAWT with blade pitch configurations of $\beta = 0°$ and $\beta = 3°$.

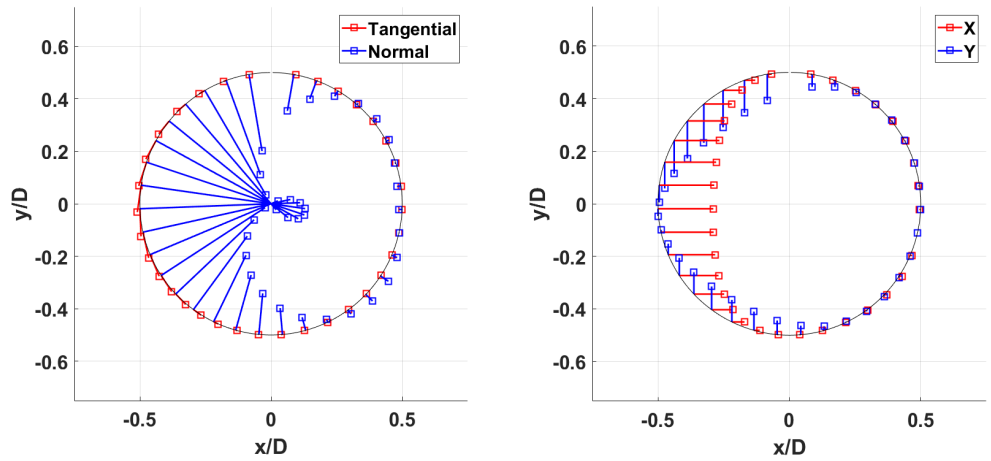

Figure 4.18: Force projection along the azimuthal sweep for a VAWT with blade pitch configuration of $\beta = 3°$.

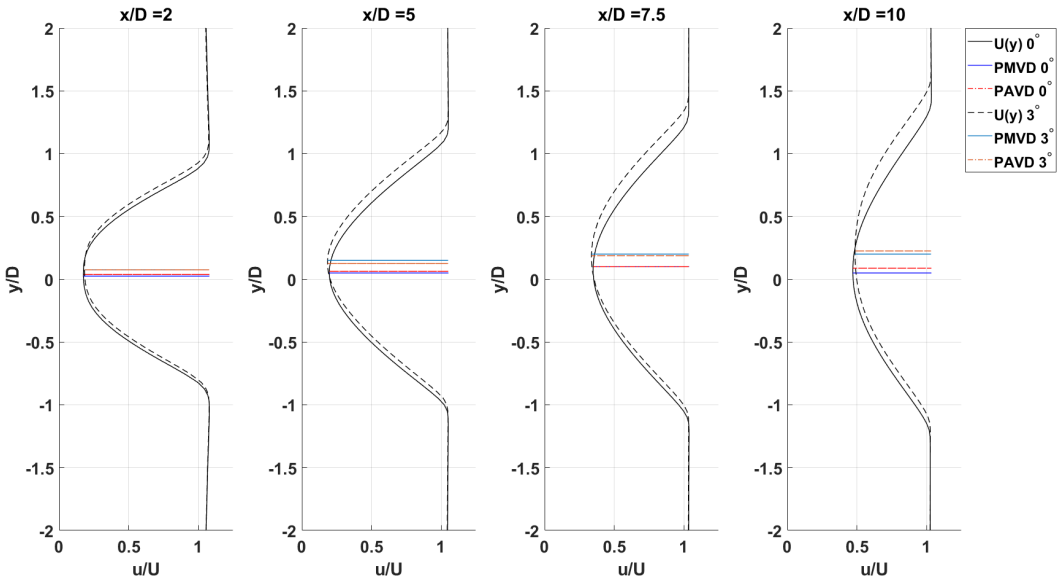

Figure 4.19: Wake velocity profile at various distances downstream of a VAWT with 0° and 3° pitch angles.

by vortices shed by the airfoil due to the change in its bound circulation $\Delta\Gamma$, for potential flow. From the Kutta-Joukowski theorem

$$\Gamma = \frac{L}{-\rho U_{rel}} \tag{4.18}$$

where L is the sectional lift, c is the chord, ρ is the density, and U_{rel} is the relative velocity at the blade section. As seen in figure 4.17, the angle of attack is displaced for $\beta = 3°$ configuration proportion to the blade pitch angle when compared to the reference case, and so is the lift coefficient. As the entire distribution is displaced by almost a constant factor, the net change in circulation shows a rather small variation in change of circulation $\Delta\Gamma$. The difference in the vorticity shed from the blade section is rather small as seen in figure 4.20. Therefore, the velocity profile in the near wake does not show significant difference between the two cases.

However, as the flow progresses farther downstream, the velocity profile shows a greater deviation. This is due to the fact that the far wake is governed by viscous diffusion. Therefore, the slight difference in the circulation distribution between the two cases is amplified. This is proved by the comparison of the wakes from the ACM (inviscid model) and the ALM (viscous model). The ACM model is the one used in De Tavernier et al (De Tavernier et al., Under Review), and is currently being peer-reviewed. The wake from ACM shows inherent deflection for $\beta = 0°$ and $\beta = 3°$ (see figure 4.21 and figure 4.22). However, the net increase in deflection between the cases of $\beta = 0°$ and $\beta = 3°$ is negligible. This is due to the inviscid nature of the ACM model. The wake is modelled by vortical induction in the flow field. As there is little difference in the circulation distribution for the two cases, the wakes in both cases are very similar. This is evident from figure 4.21.

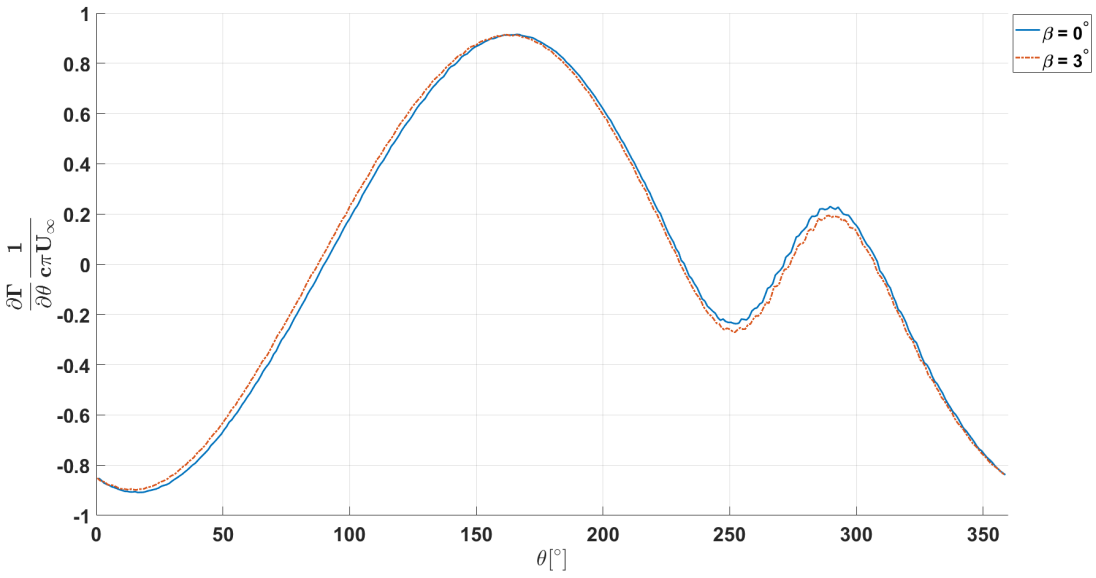

Figure 4.20: Change in bound circulation over the airfoil over one rotation for a VAWT with blade pitch configurations of $\beta = 0°$ and $\beta = 3°$.

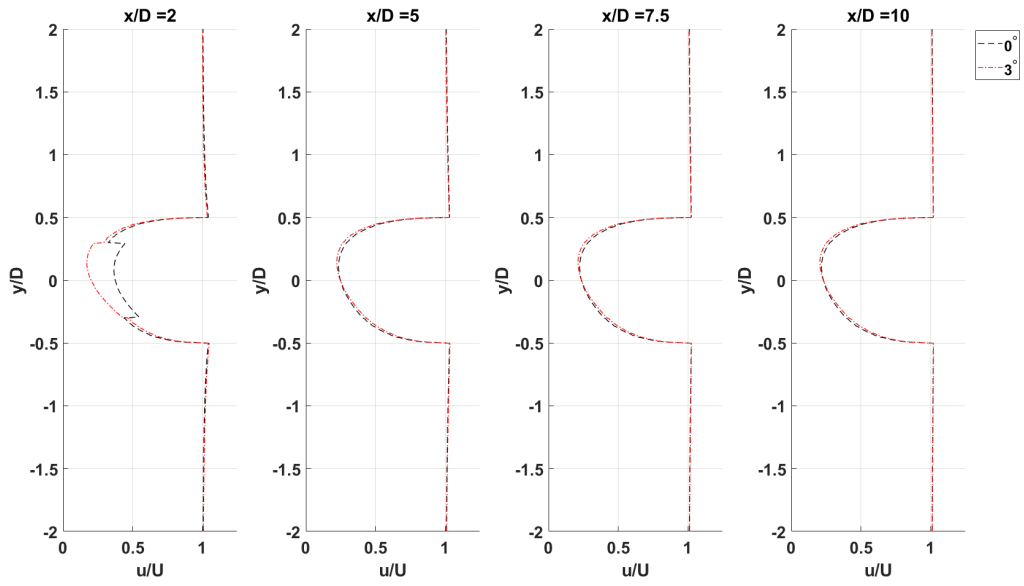

Figure 4.21: Wake velocity profile at various distances downstream of a VAWT with $0°$ and $3°$ pitch angles using the ACM.

The velocity field in figure 4.24 shows the wake deflection and expansion behind the turbine for the ALM with a constant blade pitch angle configuration of $\beta = 3°$. The increased deflection throughout the wake domain in the ALM, compared to the ACM, is attributed to

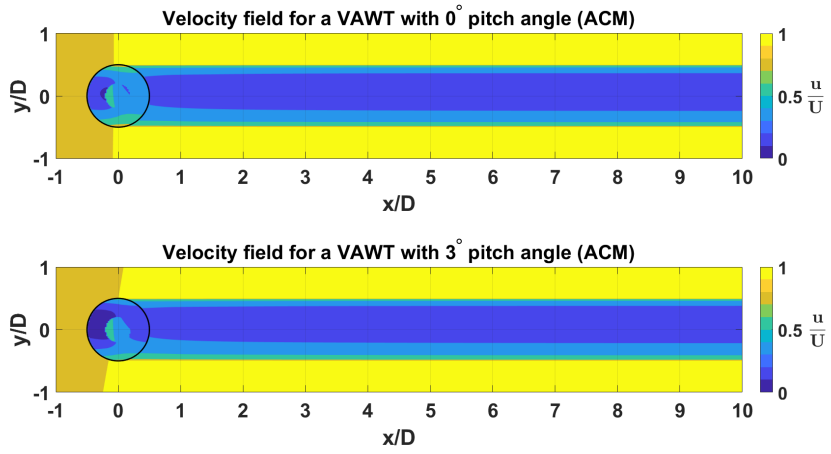

Figure 4.22: Comparison of velocity field behind a VAWT modelled with the ACM with the same turbine configurations as that for the ALM.

two factors; the viscous diffusion of the wake, and the tip vortices. The ACM does not model the tip vortices of the blades due to its 2-D nature. The asymmetry in the tip vortices shed in the wake induces a net cross velocity component that contributes to the wake deflection. Figure 4.23 shows the contribution of tip vortices on the wake expansion and deflection of the wake.

The velocity induced by the tip vortices of the retreating blade is in the $-y$ direction, whereas the velocity induced by the tip vortex from the advancing blade is in the $+y$ direction. However, it is clear that the strength of the tip vortices shed from the advancing blade is greater than that from the retreating blade, as seen in figure 4.23. This induces a net velocity component in the $+y$ direction, which contributes to the wake deflection. However, the opposite directions of induced velocity from the advancing and the retreating blade also contribute to the wake expansion.

Figure 4.25 shows the turbulence KE field. The field shows an asymmetry in the turbulence KE distribution along the centreline. The region behind advancing sweep of the turbine shows a greater area of turbulence when compared to the region behind the retreating sweep. This is due to the increased forcing in the $+y$ direction which increases mixing of the wake in the same direction. Figure 4.26 shows the vorticity field within which the wake is contained. The vorticity field clearly highlights the boundaries of the wake, which makes the extent of wake deflection more evident. It also highlights the increase in wake expansion when compared to figure 4.16.

It is clear that the blade loading distribution and the velocities induced by the tip vortices are responsible for the net cross force which deflects the wake. Using these findings, a loading distribution can be prescribed to increase the net wake deflection. The loading distribution can be input as blade pitch angle distribution. This is implemented with active pitch control and its corresponding results are discussed in section 4.8.

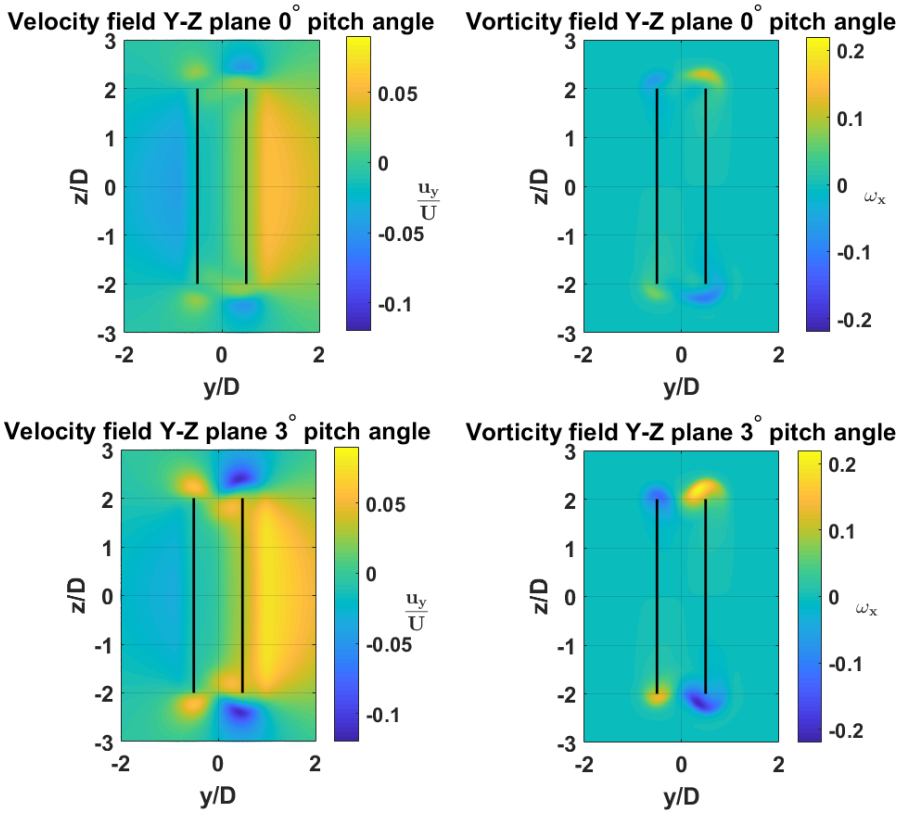

Figure 4.23: Velocity fields ($\frac{u_y}{U}$) and vorticity fields for a VAWT with $0°$ and $3°$ pitch angle on the YZ plane downstream of the turbine.

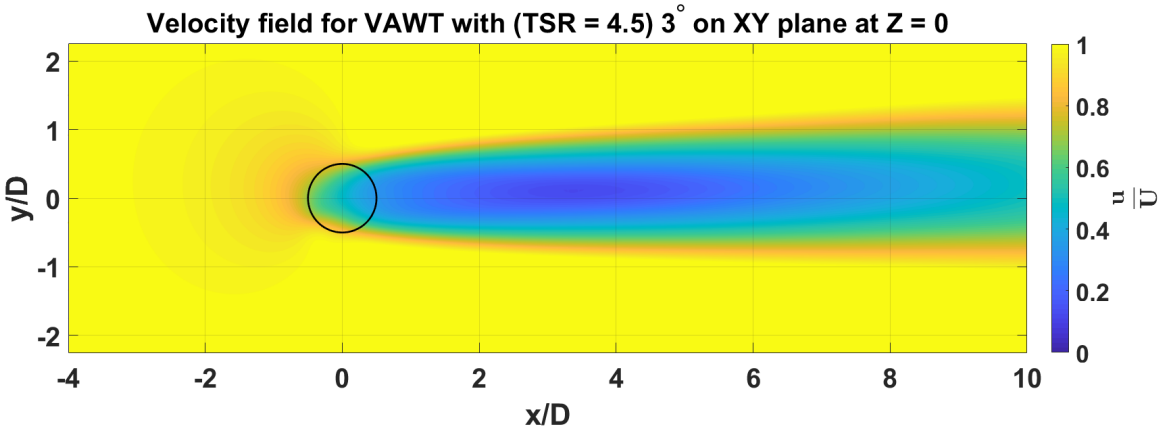

Figure 4.24: Velocity field for a VAWT with $3°$ pitch angle on the XY plane at Z = 0.

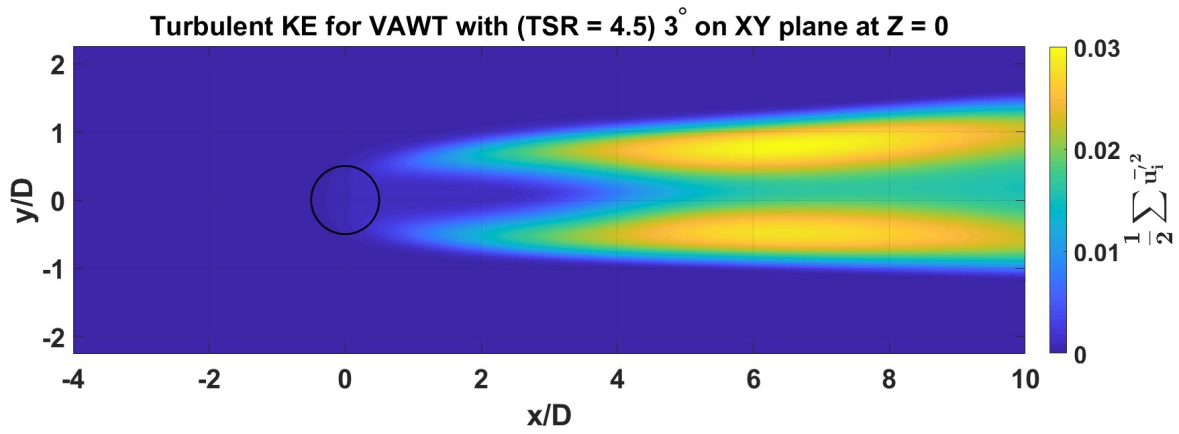

Figure 4.25: Turbulence KE field for a VAWT with 3° pitch angle on the XY plane at Z = 0.

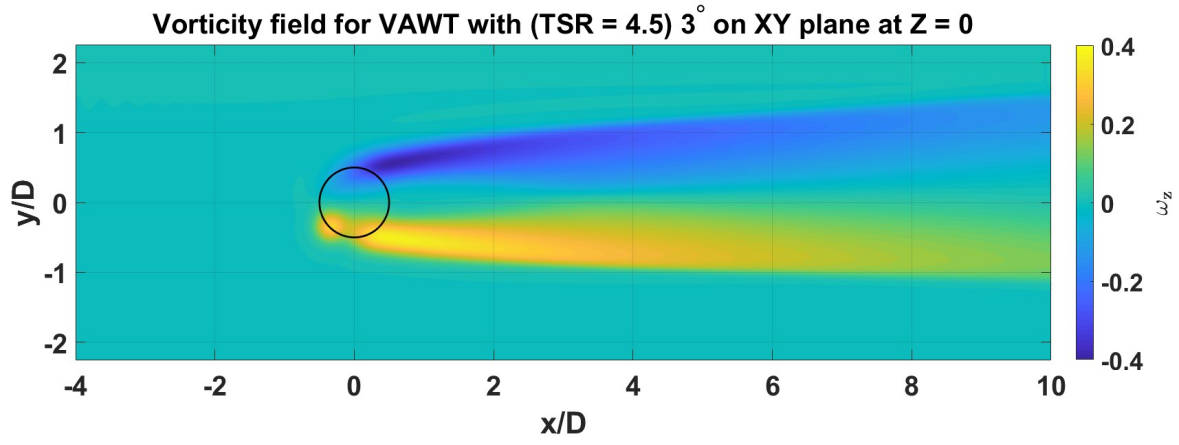

Figure 4.26: Vorticity field for a VAWT with 3° pitch angle on the XY plane at Z = 0.

4.8 Active Pitch Control

Active pitch control is the change in the pitch of individual blades as a function of its azimuthal position. Actively changing the pitch of the blade gives the control of the blade loading within the blades stall margin. In the scope of this thesis, active pitch control is used to control the forces in the x direction for thrust, and in the y direction to control the wake deflection.

As discussed in the previous section, the power performance of the turbine shows negligible change with an increase in pitch angle. At 3° blade pitch angle configuration, the net turbine performance through one complete rotation is almost the same as that at 0° while providing wake deflection. This outcome is favourable as it shows that wake can be deflected without affecting the power performance. In this case, active pitch control is used to further create asymmetry in load distribution on the blade to increase wake deflection.

Active pitch control, for this case, implements a cyclic pitch change between 0° and 3° once during every rotation of a blade. The pitch change is implemented in a single step increment. The increment rate bares negligible effect on the results, so long as it is carried out in a single time step, since the dynamic effects are neglected. The pitch change is as shown in figure 4.27. The prescribed pitch distribution maximises the force asymmetry in the y direction to increase the wake deflection.

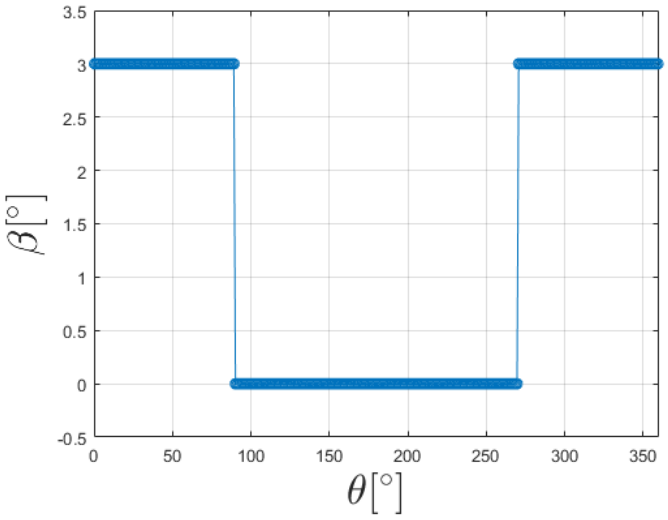

Figure 4.27: Prescribed pitch angle distribution for APC.

Figure 4.30 provides a clearer picture at the blade loading distributions as a function of azimuthal positions. In general, the force exerted on the blade along y direction has a higher magnitude in the $-y$ direction for the advancing sweep of the turbine when compared to that of the retreating sweep. The comparison of the forces in the y direction show that with the increase in the pitch angle of the blade, the y direction forces increase in magnitude for the advancing and retreating sweep. However, the magnitude of the forces in the $-y$ direction is

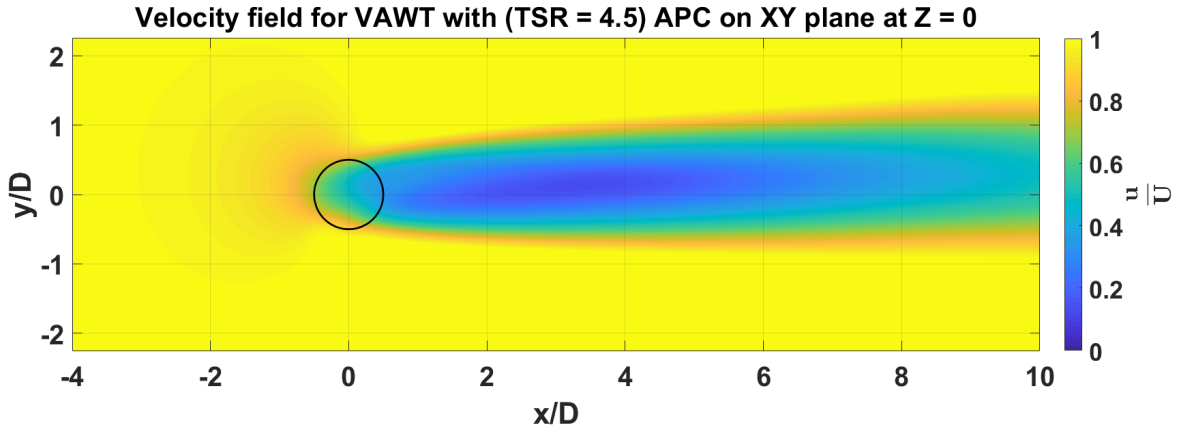

Figure 4.28: Velocity field for a VAWT with APC on the XY plane at Z = 0.

substantially higher than that of the magnitude peak in the $+y$ direction, since the advancing sweep experiences higher velocities. Figure 4.29 shows the force vector projection from the blades frame of reference and freestream frame of reference.

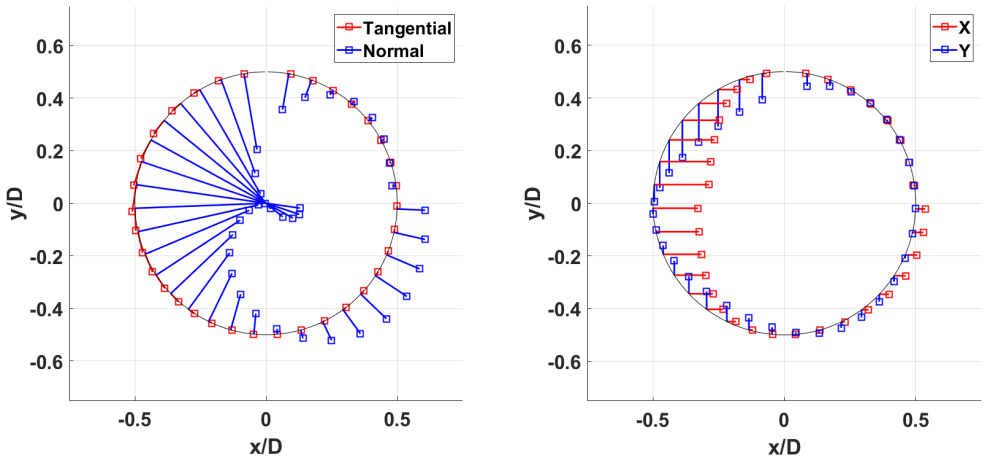

Figure 4.29: Force projection along the azimuthal sweep for a VAWT with active pitch control.

The oscillation in the magnitude of force along y direction during the downstream sweep is dominated by higher pitch configurations. This is beneficial as the asymmetry in the loading along y direction during the advancing and retreating sweep results in a net force along y direction which is responsible for the deflection of the wake.

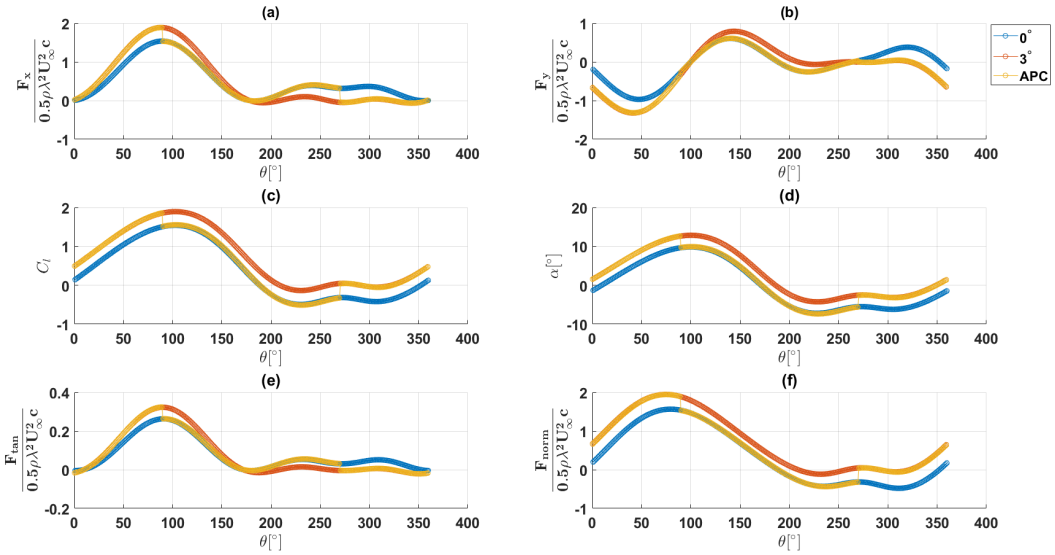

Figure 4.30: Forces comparison for blade pitch configurations of $\beta = 0°$, $\beta = 3°$ and APC.

The improvement in the wake deflection with APC can be clearly seen in the velocity profiles at set distances downstream of the turbine in comparison to the fixed pitch angle configuration, shown in figure 4.31. Increasing the blade pitch angle increases the wake deflection, however, with simple active pitch control, the wake deflection is further improved within the same pitch angle margin.

As seen in the case of a fixed 3° pitch angle, the contribution of the tip vortices' asymmetry contributes to wake deflection by providing a velocity component in the $+y$ direction. Figure 4.32 compares the contribution of the tip vortices to the wake deflection for the cases of active pitch control and the 3° pitch angle. The tip vortices shed in the retreating sweep of the turbine ($\beta = 0°$) are significantly weaker than the tip vortices shed by the advancing sweep ($\beta = 3°$). This results in a higher magnitude of induced velocity in the $+y$ direction. Subsequently, due to the smaller opposing velocities induced, the wake expansion is less when compared to the case of a fixed 3° blade pitch angle, as seen in figure 4.31.

A greater wake deflection is therefore achieved by actively controlling the blade loading through the azimuthal sweep, with negligible influence on the performance of the turbine. A more complex pitch control can be implemented to optimise the loading for various tip speed ratios.

A quantitative representation of the wake deflection and performance is provided in table 4.5 and table 4.6.

Figures 4.34 and 4.35 show the turbulence KE field and vorticity field in the wake of the turbine respectively. The asymmetry in the turbulence KE field is very distinct. The vorticity

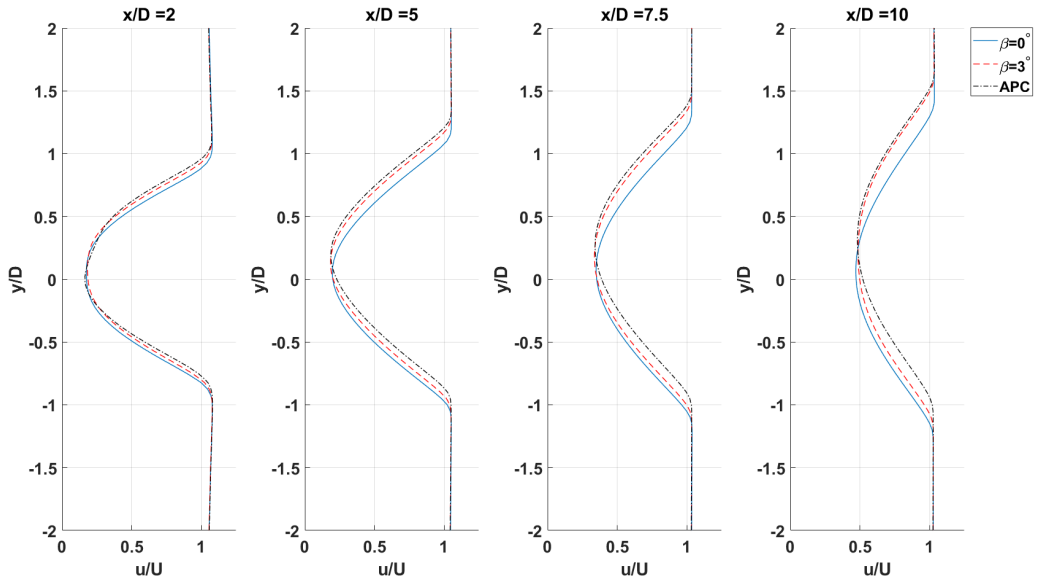

Figure 4.31: Comparison of the velocity profiles for blade configurations of $\beta = 0°$, $\beta = 3°$ and APC.

Table 4.5: Wake deflection for a VAWT with blade pitch angle configuration of $\beta = 0°$, $\beta = 3°$, and APC

$\beta[°]$	$\frac{x}{D} = 2$		$\frac{x}{D} = 5$		$\frac{x}{D} = 7.5$		$\frac{x}{D} = 10$	
$\frac{y}{D}$	**PMVD**	**PAVD**	**PMVD**	**PAVD**	**PMVD**	**PAVD**	**PMVD**	**PAVD**
0	0.0250	0.0375	0.0500	0.0625	0.1000	0.1000	0.0500	0.0875
3	0.0750	0.0750	0.1500	0.1375	0.1500	0.1750	0.1000	0.2000
APC	0.0250	0.1083	0.2000	0.1875	0.2500	0.2625	0.3000	0.3125

Table 4.6: Relative force and power coefficient for a VAWT for different blade pitch angles and APC.

Pitch angle, $\beta[°]$	$\frac{C_x}{C_{x_0}}$	$\frac{C_y}{C_{x_0}}$	$\frac{C_P}{C_{P_0}}$
0	1	0.129	1
3	0.99	0.293	0.99
APC	1	0.4351	0.99

field shows the extent of wake expansion, which is similar to that in case of $\beta = 3°$, however, the wake deflection has increased in the $+y$ direction.

It is interesting to notice that the magnitude of the vorticity shed by actuator lines in all the three cases is very similar since the net change in the bound circulation distribution over the azimuthal sweep is nearly the same, as observed in figure 4.36. The points of deviation are noticed at the locations of active pitching, at which the vortices shed are proportional to the amplitude of change in the bound vortex due to active pitching function. However, at the

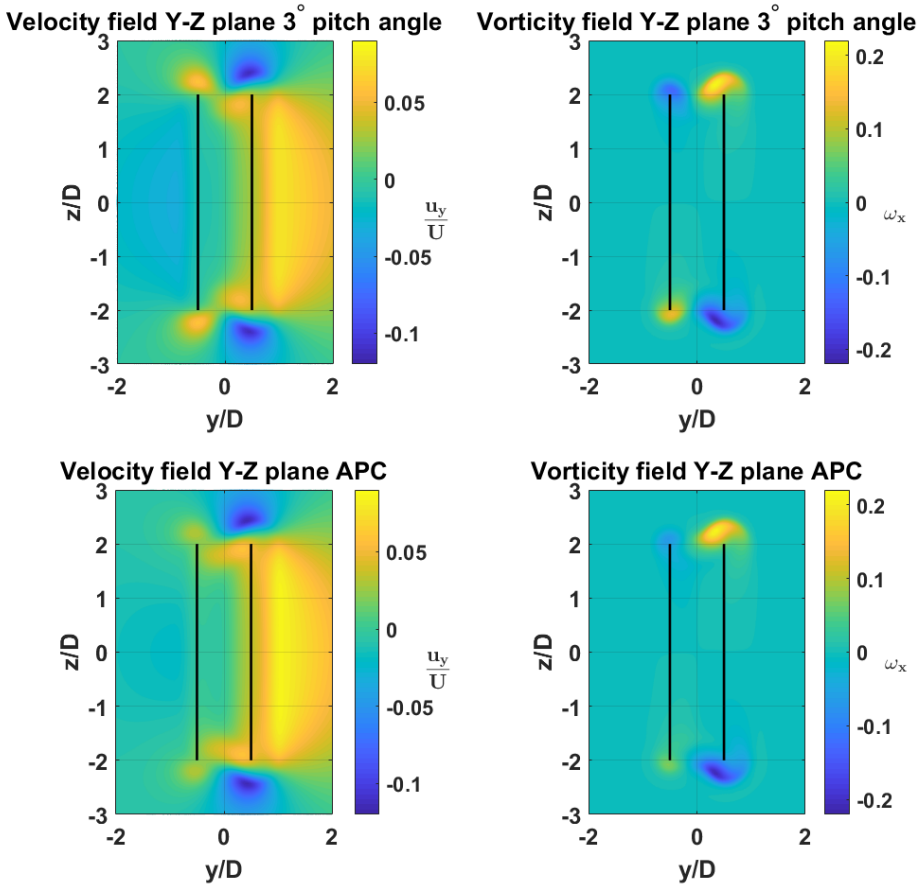

Figure 4.32: Velocity fields ($\frac{u_y}{U}$) and vorticity fields for a VAWT with $3°$ and APC on the YZ plane downstream of the turbine.

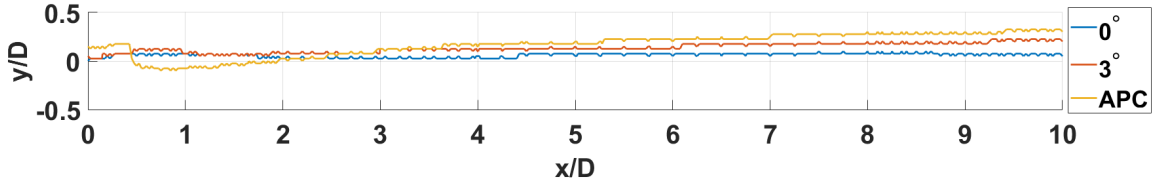

Figure 4.33: Comparison of points of maximum velocity deficits for blade configurations of $\beta = 0°$, $\beta = 3°$ and APC.

two points of active pitching, the vortices shed have opposite orientation, which reduce any major deviation in the near wake profile as seen in figure 4.31. The far wake profile deviation is attributed to viscous diffusion which amplifies the small difference in the shed vortices.

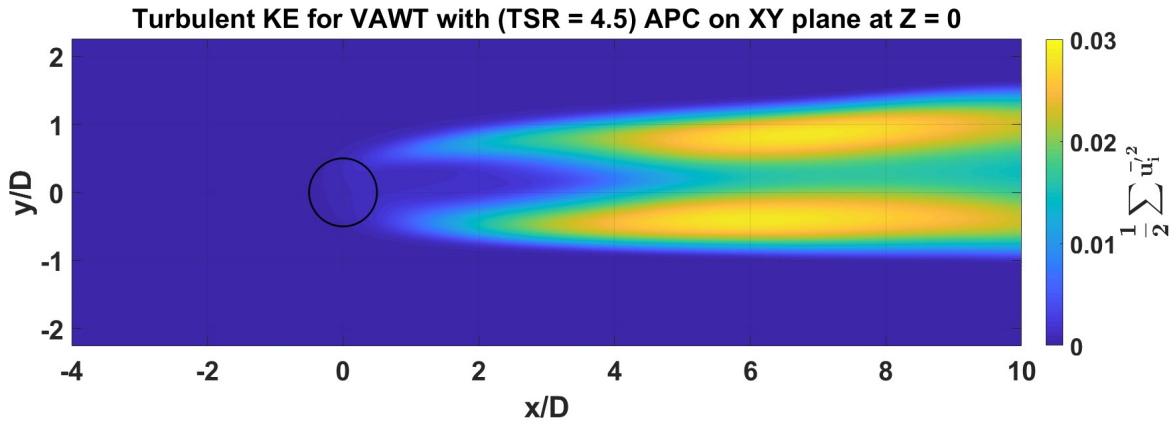

Figure 4.34: Turbulence KE field for a VAWT with APC on the XY plane at Z = 0.

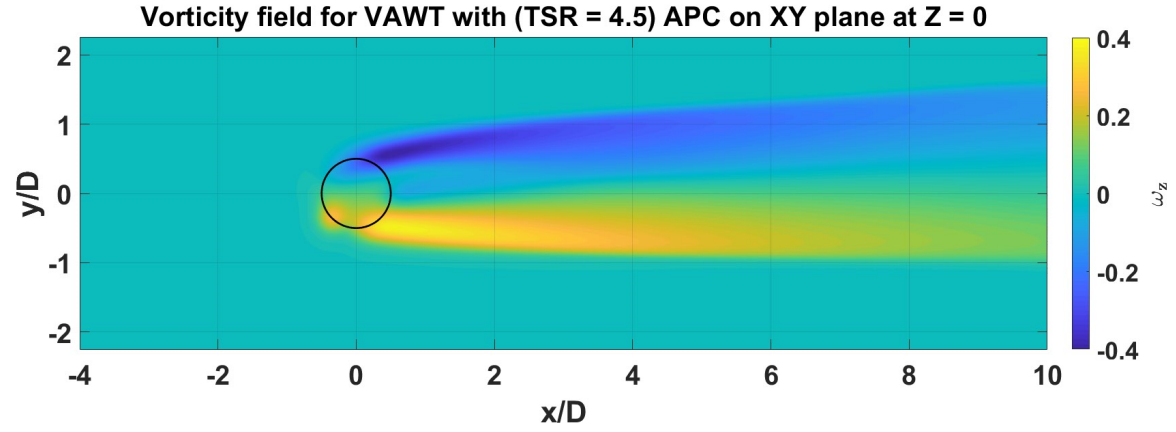

Figure 4.35: Vorticity field for a VAWT with APC on the XY plane at Z = 0.

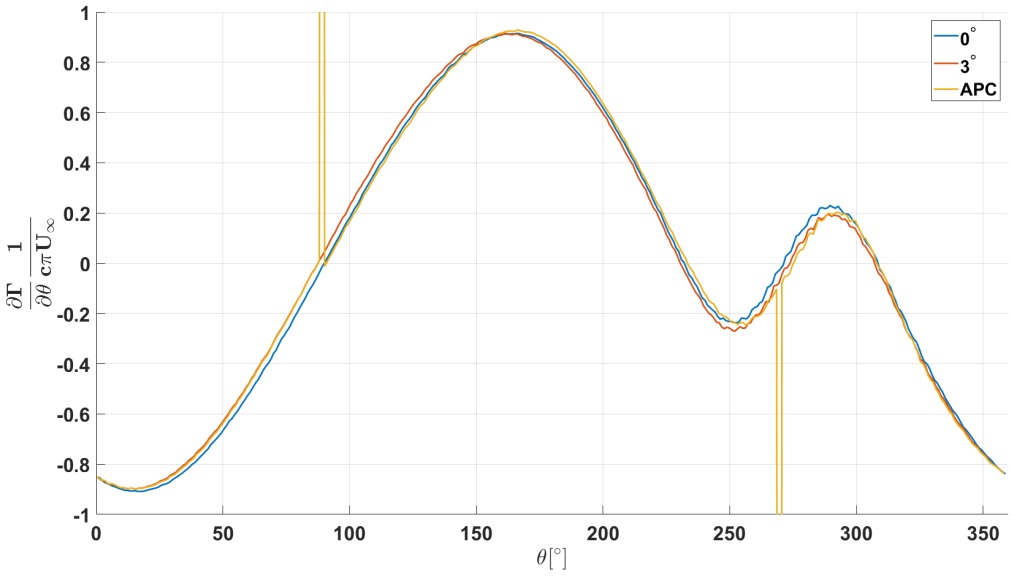

Figure 4.36: Change in the bound circulation over the airfoil over one rotation for a VAWT with blade pitch configurations of $\beta = 0°$, $\beta = 3°$, and APC.

4.9 Comparison of blade loading for VAWT and HAWT in yaw

The final objective of this thesis is to compare the blade loading during wake deflection between the HAWT and the VAWT. For this study, the blade loading data is taken from Martinez et al (Martinez et al., 2015). The data provided is for the case of two HAWT turbines, one in the far wake of the other, however, for comparison, only the data from the upstream turbine is considered. The simulation is carried out with an ALM-LES solver. The HAWT is simulated for a yawing turbine at $\gamma = 0°$, $14.67°$, and $27.64°$ (Martinez et al., 2015). The data is recorded once the forces on the blade have stabilized. The parameters compared are the force coefficients in the x,y direction, and the power coefficient. As it is difficult to compare the parameters quantitatively for HAWT and VAWT, the study is carried out in a qualitative manner.

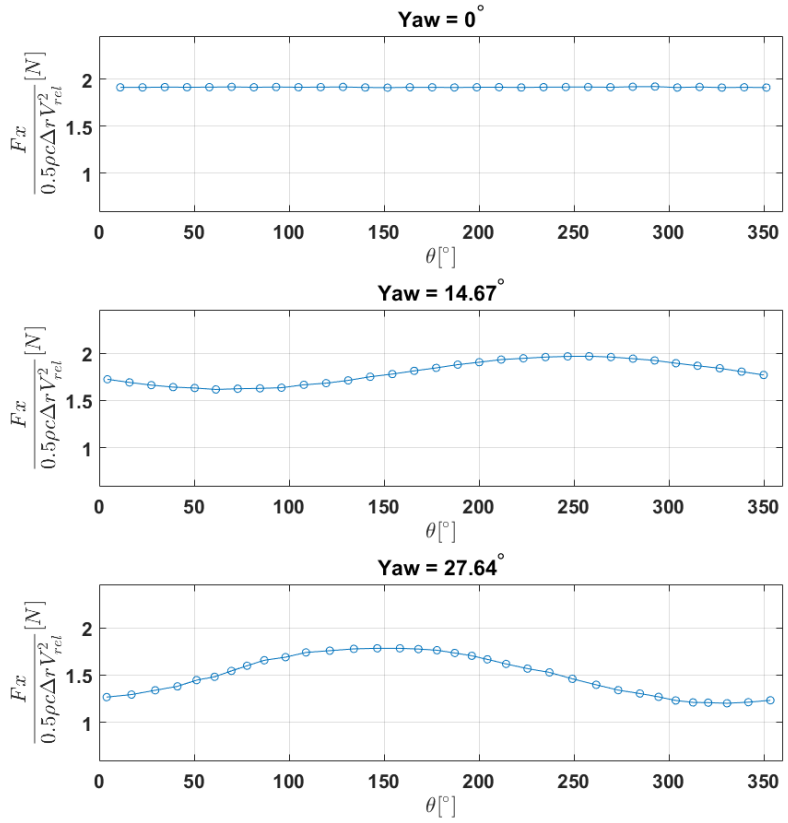

Figure 4.37: Streamwise force component for a HAWT in various yawed configurations, $\gamma = 0°$, $\gamma = 14.67°$, $\gamma = 27.64°$.

As discussed in section 2.2, it is possible to deflect the wake with a HAWT in a yawed configuration. Forces on the blade, ideally, do not vary when the HAWT is aligned with the

flow since the angle of attack experienced by the blade section is the same throughout its azimuthal sweep. As the HAWT is subjected to skewed inflow and/or the turbine is yawed with respect to the inflow velocity vector, the blades begin to experience the advancing and retreating effects as the blade section traverses the azimuthal sweep. This causes the angle of attack to vary throughout the azimuthal sweep, and in turn, create an unsteady loading on the blade. The unsteady blade loading is also accompanied by a phase shift in the loading peak caused by the increase in advancing and retreating displacement of blade sections from the axis of rotation of the un-yawed turbine. This is evident in figure 4.37.

Also, as the turbine is yawed, the net thrust vector is deflected which provides a force component in the cross-flow direction. This force is responsible for the deflection of the wake. This can be observed in figure 4.38.

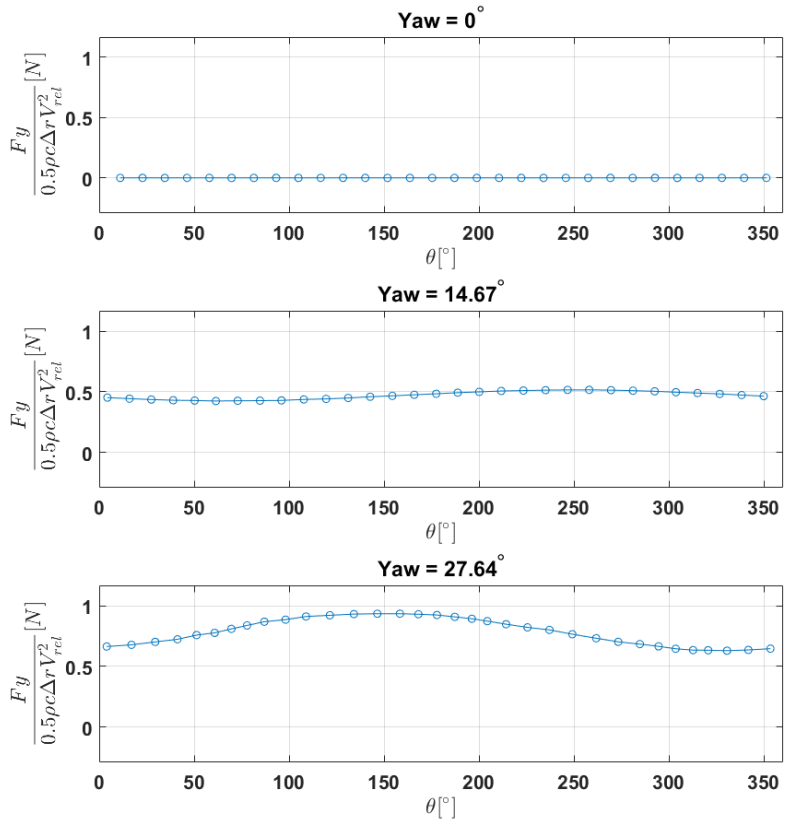

Figure 4.38: Cross force component for a HAWT in yawed configurations, $\gamma = 0°$, $\gamma = 14.67°$, $\gamma = 27.64°$.

In the case of the un-yawed turbine, the net cross force component is zero as the thrust vector is in line with the freestream. As the turbine is yawed, the thrust vector is deflected along its new axis vector, and a cross force component is evident. The cross force component oscillates through the azimuthal sweep due to the advancing and the retreating effects on the blade.

The magnitude of the cross force increases with an increase in yaw angle. An important observation to be made is that the blade loading in the cross-flow direction does not change signs as the blade only provides forces in one direction. The oscillation in the cross force component also experiences a phase shift in its peak loading with the increase in yaw angle of the turbine.

As the VAWTs inherently experience unsteady loading, the blades provide components of force in both, the freestream, and the cross flow direction. Increasing the blade pitch angle increases wake deflection, however, since the extent of advancing and retreating magnitude for blade displacement is fixed by the radius, the force distribution does not experience phase shift.

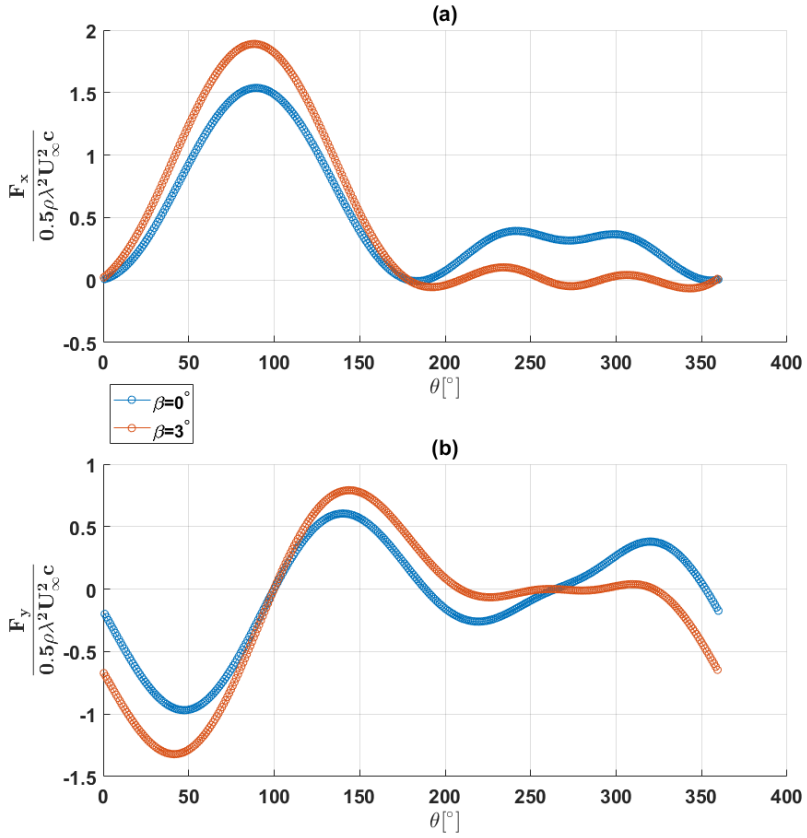

Figure 4.39: Streamwise and cross force components for a VAWT with blade pitch angle of $\beta = 0°$ and $\beta = 3°$.

The streamwise force component distribution witnesses the shift in magnitude of the curve, however, the cross force component witnesses an amplification of the peaks, as seen in figure 4.39. Another important observation is that in the case of a VAWT, the force component tend to change signs as the blade follows the azimuthal path. This is due to the complete reversal of the direction of the blade motion through one rotation.

Finally, the difference in the effects of blade loading on the power performance is considered. In the case of a HAWT, as the turbine is yawed, the forcing on the blade section changes which reduces the blade loading over a portion of the rotation. The loss of blade loading results in a reduction in performance of the turbine. This is due to the fact that the loading lost due to skewed inflow is not recovered in the same rotation. Table 4.7 shows that with an increase in yaw angle of the turbine the cross force component increases but results in a loss of performance of the turbine. Since the base case of a HAWT does not provide cross-flow force, the cross-flow force coefficients are not normalised, however, the qualitative inference from the presented data is that with an increase in the cross force component, the performance of the turbine reduces.

Table 4.7: Relative force and power coefficient for a HAWT in yawed configuration.

Yaw angle, $\gamma[^\circ]$	$\frac{C_x}{C_{x_0}}$	$\frac{C_y}{C_{x_0}}$	$\frac{C_P}{C_{P_0}}$
0	1	0	1
14.67	0.92	0.24	0.92
27.64	0.72	0.52	0.73

In the case of a VAWT, a change in the blade pitch angle results in the shift of the blade loading from the upstream sweep to the downstream sweep of the turbine. Therefore, over a complete rotation, the change in blade loading is negligible and the performance is retained as seen in table 4.8. This provides another advantage of a VAWT over a HAWT, as the VAWT manages wake deflection with negligible influence on the performance of the turbine.

Table 4.8: Relative force and power coefficient for a VAWT for different blade pitch angles.

Pitch angle, $\beta[^\circ]$	$\frac{C_x}{C_{x_0}}$	$\frac{C_y}{C_{x_0}}$	$\frac{C_P}{C_{P_0}}$
0	1	0.129	1
3	0.99	0.293	0.99

Visualisation of the wake deflection gives a better understanding of the difference in wake deflection between a HAWT and a VAWT. The visualisation is carried out on the juxtaposition of the velocity fields in the wake of the turbines, in the case of the centred wake and deflected wake. The velocity field of the HAWT considered is the one discussed in section 2.2.1.

The velocity profiles shown in figure 4.40 highlights the extent of wake deflection in the far wake of the turbine for a HAWT. Comparing the velocity profiles of a HAWT to those from the wake of a VAWT (figure 4.19) reflects the wake expansion and the wake deflection.

Figure 4.41 shows the velocity of the centred wake in juxtaposition. It is noticed that the wake of a VAWT expands considerably more than that of the HAWT. This is due to the increased turbulence in the wake of the VAWT resulting from blade-wake interactions. The increased turbulence diffuses over a larger area. Another aspect to notice is that even in the case of the centred wake, the VAWT inherently shows a slight deflection in the far wake region.

Now considering the case of the deflected wake, the velocity fields from the HAWT yawed

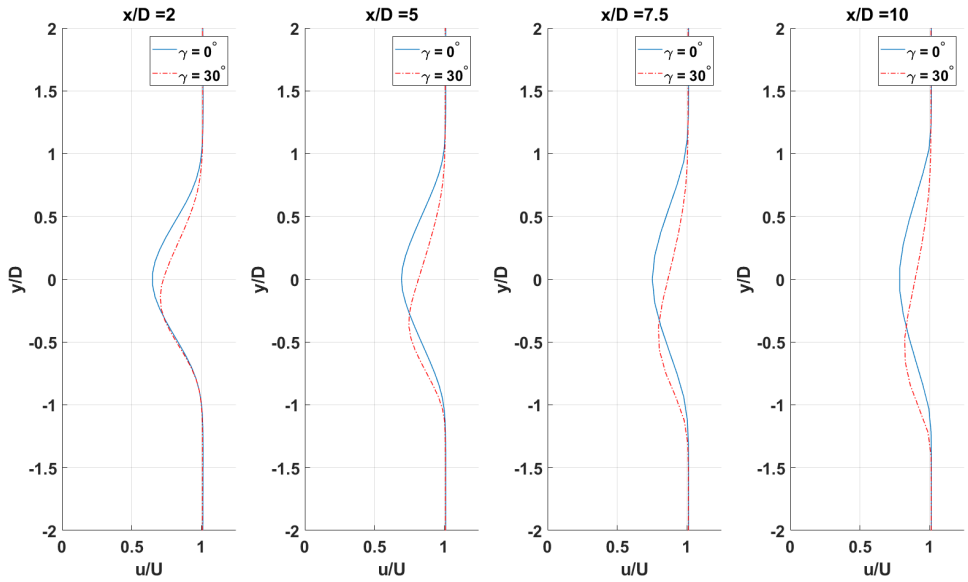

Figure 4.40: Velocity profiles in the wake of a HAWT with $0°$ and $30°$ yaw angle configurations.

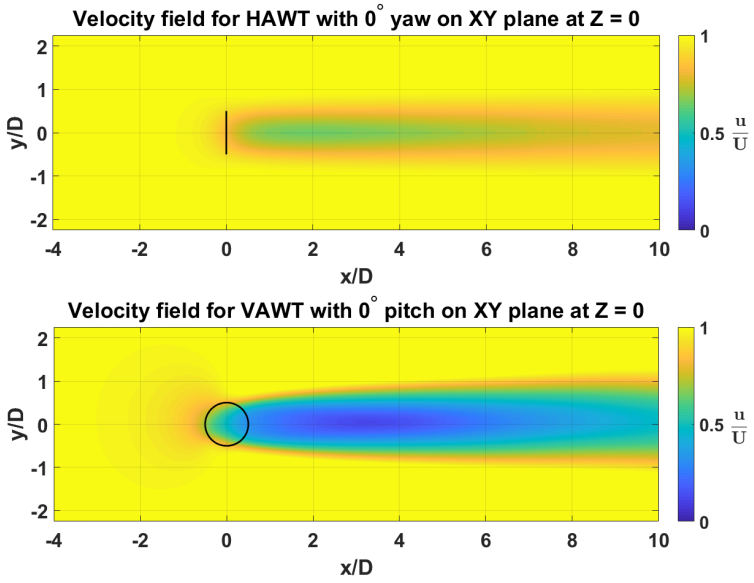

Figure 4.41: Comparison of centred wake behind a HAWT and a VAWT.

at $30°$ is compared to the velocity field of VAWT with constant blade pitch angle of $3°$. A qualitative comparison will be made.

Figure 4.42 shows the velocity of the deflected wake in juxtaposition. The velocity fields in figure 4.42 show that the wake deflection is more prominent for a HAWT than its VAWT

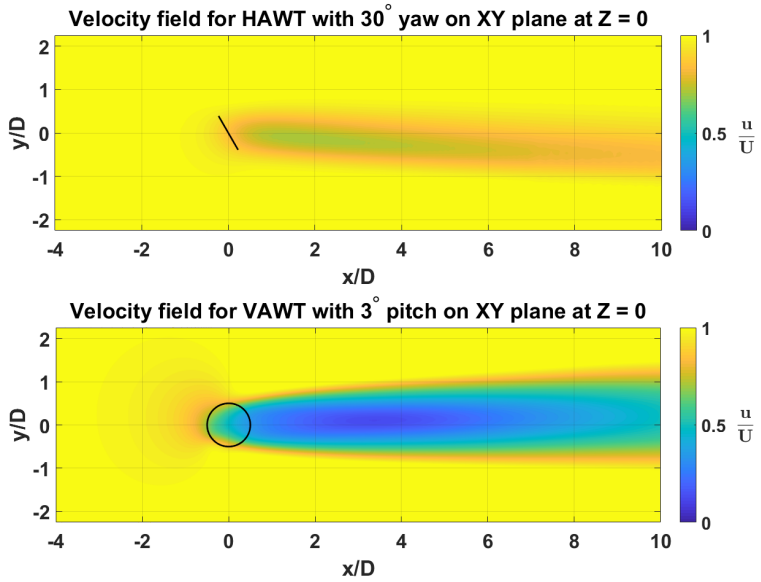

Figure 4.42: Comparison of the deflected wake behind a HAWT and a VAWT.

counterpart. This can be attributed to two effects, the difference in geometric parameters between the turbines and the aspect ratios. Firstly, in the case of a HAWT, the turbine is yawed at 30°, which according to (Bastankhah and Porte-Agle, 2016), is the maximum yaw angle to attain a compromise between the power loss and wake deflection. However, in the case of a VAWT, the blade pitch angle of 3° is taken for the purpose of understanding the behaviour of the wake. It is not optimised for maximum wake deflection. The wake deflection can be further increased with APC or higher blade pitch angles since the change in blade loading has little effect on the power performance of the turbine. Secondly, the VAWT is simulated at very high aspect ratios, to reduce the effects of tip vortices as this provides a clearer understanding of the dependence of wake deflection on the loading distribution. The increased aspect ratio reduces any effects of the tip vortices on the wake study since only the central section is considered. However, in the case of a HAWT, the influence of tip vortices is not mitigated. The vortices shed from the tip of the blade contributes to the dynamics of the wake structure.

Chapter 5

Conclusions

The concept of wake deflection is very useful in designing the wind farm layout as it allows for a more compact wind farm. The wake deflection aft of the HAWT is done by yawing rotor with respect to the inflow to deflect the thrust vector. The deflected thrust vector creates a cross force component which is responsible for the wake deflection. However, this results in loss of power with an increase in the wake deflection In the case of a VAWT, the wake deflection is guided by three important factors i.e. the cross force component, tip vortical contributions, and viscous diffusion. Due to the omnidirectional design of VAWTs, 'yawing' simply does not apply. The deflection of net thrust vector is created by the asymmetric blade loading over the rotation across the freestream direction. The VAWTs inherently produce a small cross force component, as seen in the case of $\beta = 0°$. When the blade loading is incremented over all the azimuthal positions by changing its fixed blade pitch angle to $\beta = 3°$, a fraction of the tangential force component is lost during the upstream sweep of the turbine. However, since the blade pitch angle is fixed, the increased loading in the downstream sweep of the turbine recovers most of the lost loading. The normal force on the blade experiences a net increment through one rotation. When the frame of reference is changed from blade reference to freestream directions, the streamwise loading shows similar behaviour to that of the tangential loading and cross loading shows a net increment through one rotation. This ensures that while a cross force component is created for wake deflection, the net turbine power coefficient shows negligible change. Due to VAWTs inherent unsteady loading through an azimuthal sweep, it is possible to create an additional cross force component for same blade pitch amplitude (3°) by actively changing the blade pitch angle so as to increase the asymmetry in the blade loading between advancing and retreating sweep, as shown in section 4.8.

The asymmetric loading is also responsible for a difference in the strength of tip vortices shed during the advancing and the retreating sweep. The increased loading on the advancing sweep sheds a stronger vortex which contributes positively to the wake deflection. The asymmetry in the cross force component can be increased by actively controlling the blade pitch angle, within the same pitch amplitude domain. In the far wake, the diffusion of the counter-rotating

vortices from the advancing and the retreating sweep results in a significant expansion of the wake as well as amplification of the wake deflection. The expansion of the wake is not favourable as the region of momentum deficiency is greater. However, the amplification of the wake deflection due to asymmetric diffusion of the wake results in an additional deflection in the far wake region.

Comparing the wake deflection between the HAWTs and the VAWTs, it is observed that the extent of wake deflection in the HAWTs is greater since the orientation of the turbine is changed to physically provide a cross force component when compared to the asymmetric loading in the VAWTs. However, as the HAWT is yawed, it loses a fraction of the streamwise component of the inflow velocity which results in a loss of power. Thus, yawing the turbine over a certain angle does not result in significant increase in wake deflection, while the power loss is increasingly unfavourable. As the VAWTs have a passive mechanism of loading recovery in the downstream region, the extent to which the wake deflection can be increased, while having minimal effect on its power performance, is greater. This is further enhanced by the active pitch control technique. However, as the plane of rotation is perpendicular to the freestream flow, the HAWTs can change the direction of deflection by simply yawing the turbine in the opposite direction. As the plane of rotation is aligned with the freestream flow, the VAWTs are designed to rotate in only one direction which in turn limits the wake deflection to just one direction in reference to the freestream flow direction.

Considering the results of this thesis, it is safe to conclude that the VAWTs have an inherent tendency to deflect the wake, and optimisation of the wake deflection can be carried out more efficiently when compared to the HAWTs. However, the design of the VAWT wind farms utilising wake deflection to optimise the farm power output will have to consider the limitations in the directionality of wake deflection from the VAWTs.

Chapter 6

Recommendations

The conclusions drawn at the end of this thesis raise new questions that need a further investigation. In this chapter, a few recommendations are stated that should be researched to gain a clearer understanding of the wake deflection, and its advantages and disadvantages.

- Having acknowledged the contribution of the tip vortices in deflecting the wake, it is interesting to understand the extent of its contribution when compared to the cross force component from the blade. A suggested method for the same would be to compute the induced velocity in the $+y$ direction due to the tip vortices and the velocity resulting from the direct blade loading. The contribution from each should be quantitatively compared for the cases with various aspect ratios of the turbine.

- As the opposing velocities along the $\pm y$ direction, induced by the tip vortices, contribute to the wake expansion, it is crucial to investigate the possibility of directional expansion of the wake using active pitch control. This question becomes very important for application of wake deflection in wind farms because if the core of the wake is deflected and the deflection is also accompanied by a significant expansion which would overshadow the subsequent turbines, then this will negate the benefits of wake deflection.

- For quantitative comparison of wake deflection between the HAWT and the VAWT, certain dimensionless turbine parameters must be established between the two along which it would be sensible to carry out the wake deflection, the wake expansion, and the wake recovery comparisons.

- The simulations carried out in the scope of this thesis are done so without considering the unsteady effects of the partial and complete stall of the blade. However, as the reduced frequency increases, the unsteady effects become significant, especially in the case of active pitch control. The wake solutions will change significantly due to a loss of lift and a delayed loading response on the blades.

- The VAWTs are omnidirectional in accepting the inflow, however, its wake deflection

characteristics are unidirectional. This opens a new scope of research into the wind farm design for VAWTs utilising the wake deflection technique.

Bibliography

P.H. Alfredsson and J.A Dahlberg. *A Preliminary Wind Tunnel Study of Windmill Wake Dispersion in Various Flow Conditions, Part 7.* Aeronautical Research Inst. of Sweden and NASA, 1979.

H. Arabian-Hoseynabadi, H. Oraee, and P.J. Tavner. Failure Modes and Effects Analysis (FMEA) for wind turbines. 2010.

Z.N. Ashrafi, M. Ghaderi, and A. Sedaghat. Parametric study on off-design aerodynamic performance of a horizontal axis wind turbine blade and proposed pitch control. *Energy Conversion and Management*, 93(349), 2015.

P. Bachant. Turbinesfoam. v0.0.7.

P. Bachant, A. Goude, and M. Wosnik. Actuator line modeling of vertical-axis turbines. *Wind Energy*, 2016a.

P. Bachant, M. Wosnik, B. Gunawan, and V.S. Neary. Experimental Study of a Reference Model Vertical-Axis Cross-Flow Turbine. *PLoS ONE*, 11(9), 2016b.

M. Bastankhah and F. Porte-Agle. Experimental and theoretical study of wind turbine wakes in yawed conditions. *Journal of Fluid Mechanics*, 806(506), 2016.

A. Betz. "Schraubenpropeller mit geringstem Energieverlust. Mit einem Zusatz von l. Prandtl. *Nachrichten von der Gesellschaft der Wissenschaften zu Gttingen, Mathematisch-Physikalische Klasse*, 1919.

J. Boussinesq. Thorie de l'coulement tourbillant. *Acadmia des Sciences de l'Institut de France*, 1(23), 1877.

T. Burton, N. Jenkins, D. Sharpe, and E. Bossanyl. *Wind Energy Handbook.* John Wileyand Sons Ltd., 2011.

M.C. Claessens. The Design and Testing of Airfoils for Application in Small Vertical Axis Wind Turbines. TU Delft, 9 January 2006. Master Thesis.

D. De Tavernier, C. Ferreira, G. van Bussel. Airfoil optimisatoin for vertical-axis wind turbines with variable pitch. *Wind Energy*, Under Review.

P. Deglaire. ntry"¿Deglaire, P. (2010). ¡i¿Analytical Aerodynamic Simulation Tools for Vertical Axis Wind Turbines. Digital Comprehensive Summaries of Uppsala Dissertations from the Faculty of Science and Technology, November 2010. PhD dissertation.

P. Deglaire, S. Engblom, O. Agren, and H. Bernhoff. Analytical solutions for a single blade in vertical axis turbine motion in two-dimensions. *European Journal of Mechanics - B/Fluids*, 28(4), 2008.

E. Dyachuk. Aerodynamics of Vertical Axis Wind Turbines: Development of Simulation Tools and Experiments. Uppsala University, 9 October 2015. Doctoral Thesis.

E. Dyachuk, A. Goude, and H. Bernhoff. Dynamic Stall Modeling for the Conditions of Vertical Axis Wind Turbines. *AIAA Journal*, 52(1), 2014.

D.M. Eggleston and K. Starcher. A Comparative Study of the Aerodynamics of Several Wind Turbines Using Flow Visualization. *Journal of Solar Energy Engineering*, 112(4), 1990.

C.S. Ferreira. The near wake of the vawt: 2d and 3d views of the vawt aerodynamics. TU Delft Faculty of Aerospace engineering, October 2009. PhD dissertation.

C.S. Ferreira and F. Scheurich. Demonstrating that power and instantaneous loads are decoupled in a vertical-axis wind turbine. *Wind Energy*, 17(3), 2013.

C.S. Ferreira, C. Hofemann, K. Dixon, G.A.M. Van Kulk, and G.J.W. Van Bussel. 3D wake dynamics of the VAWT: Experimental and numerical investigation. *48th AIAA Aerospace Sciences Meeting including the New Horizons Forum and Aerospace Expoition*, 2010.

C.S. Ferreira, H.A. Madsen, M. Barone, B. Roscher, P. Deglaire, and I. Arduin. Comparison of aerodynamic models for Vertical Axis Wind Turbines. *Journal of Physics: Conference Series*, 524(1), 2014.

P. Fraunie, C. Beguier, I. Paraschivoiu, and G. Brochier. Water channel experiments of dynamic stall on Darrieus wind turbine blades. *Journal of Propulsion and Power*, 2(5), 1986.

A. Goude. Fluid Mechanics of Vertical Axis Turbines: Simulations and Model Development. Digital Comprehensive Summaries of Uppsala Dissertations from the Faculty of Science and Technology, March 2012. Dissertation.

M.M. Hand, D.A. Simms, L.J. Fingersh, D.W. Jager, J.R. Cotrell, S. Schreck, and S.M. Larwood. Unsteady Aerodynamics Experiment Phase VI: Wind Tunnet Test Configuration and Available Data Campaigns. NREL, December 2001. Technical Report 500-29955.

S.H. Hezaveh, E. Bou-Zeid, M.W. Lohry, and L. Martinelli. Simulation and wake analysis of a single vertical axis wind turbine. *Wind Energy*, 20(4), 2016.

M.F. Howland, J. Bossuyt, L.A. Martinez-Tossas, J. Meyer, and C. Meneveau. Wake Structure of Wind Turbines in Yaw under Uniform Inflow Conditions. *Renewable and Sustainable Energy*, 8(043301), 2016.

P.K. Jha, M.J. Churchfield, and S. Moriarty, P.J. Schmitz. Guidelines for Volume Force Distributions Within Actuator Line Modeling of Wind Turbines on Large-Eddy Simulation-Type Grids. *Journal of Solar Energy Engineering*, 136(3), 2014.

A. Jimenez, A. Crespo, E. Migoya, and J. Garcia. Advances in large-eddy simulation of a wind turbine wake. *Journal of Physics: Conference Series*, 75, 2007.

A. Jimenez, A. Crespo, E. Migoya, and J. Garcia. Large-eddy simulation of spectral coherence in a wind turbine wake. *Environmental Research Letters*, 3(1), 2008.

A. Jimenez, A. Crespo, and E. Migoya. Application of a LES technique to characterize the wake deflection of a wind turbine in yaw. *Wind Energy*, 6(13), 2009.

A. Katz and J. Plotkin. *Low-Speed Aerodynamics - 2nd Edition*. Cambridge University Press, 2000.

E.E. Laplin. Theoretical performance of vertical axis wind turbines. American Society of Mechanical Engineers, Winter Annual Meeting, November 1975. Technical Report.

B.E. Launder and D.B. Spalding. The numerical computation of turbulent flows. *Computer Methods in Applied Mechanics and Engineering*, 3(2), 1974.

J.G. Leishman and T.S. Beddoes. A SemiEmpirical Model for Dynamic Stall. *Journal of the American Helicopter*, 34(3), 1989.

A.H. Madsen, N.N. Sorensen, and S. Schreck. Yaw Aerodynamics Analyzed With Three Codes in Comparison With Experiment. *ASME 2003 Wind Energy Symposium*, 2003.

H.A. Madsen. The actuator cylinder - a flow model for vertical axis wind turbines. Institute of Industrial Construction and Energy Technology, January 1982. PhD dissertation.

L. Martinez, M. Howland, and C. Meneveau. Large eddy simulation of wind turbine wakes with yaw effects. 68TH ANNUAL MEETING OF THE APS DIVISION OF FLUID DYNAMICS, November 2015.

V. Mendoza, P. Bachant, M. Wosnik, and A. Goude. Validation of an Actuator Line Model Coupled to a Dynamic Stall Model for Pitching Motions Characteristic to Vertical Axis Turbines. *Journal of Physics: Conference Series*, 753, 2016.

D. Micallef. A Review of Wind Turbine Yaw Aerodynamics. *Wind Turbines- Design, Control and Applications*, 2015.

P.G. Migliore, W.P. Wolfe, and J.B Fanucci. Failure Modes and Effects Analysis (FMEA) for wind turbinesFlow Curvature Effects on Darrieus Turbine Blade Aerodynamics. *Journal of Energy*, 4(2), 1980.

R.F. Mikkelsen. Actuator Disc Methods Applied to Wind Turbines. Technical University of Denmark, June 2003. Doctoral Thesis.

R.F. Mikkelsen, J.N Sørensen, and N. Troldborg. Prescribed wind shear modelling with the actuator line technique. Milan, Italy, 7-10 August 2007. 2007 European Wind Energy Conference and Exhibition.

J.C. Murary and M. Barone. The Development of CACTUS, a Wind and Marine Turbine Performance Simulation Code. *49th AIAA Aerospace Scienced Meeting including the New Horizons Forum and Aerospace Exposition*, 2011.

OpenFOAM. Openfoam, the open source cfd toolbox user guide. OpenFOAM Foundation Limited, June 2013. Guide.

L. Prandtl. Applications of Modern Hydrodynamics to Aeronautics. National Advisory Committee for Aeronautics, 1 January 1923. NASA Ames Research Center Classical Aerodynamics Theory.

J.C. Puig, P.J Gamez, and G. Raush. Openfoam guide for begineers. The FOAM House, Barcelona, June 2014. Guide.

B. Sanderse, S.P. van der Pijl, and B. Koren. Review of computational fluid dynamics for wind turbine wake aerodynamics. *Wind Energy*, 14(7), 2011.

S. Sarmast, W.Z. Shen, W.J. Zhu, R.F. Mikkelsen, S.P. Breton, and S. Ivanell. Validation of the actuator line and disc techniques using the New MEXICO measurements. *Journal of Physics: Conference Series*, 753, 2016.

J.g. Schepers and S. Schreck. The importance of aerodynamics and the role of aerodynamic measurements . *The Science of making Torque*, 2013.

F.G. Schmitt. A propos de l'hypothse de viscosit turbulente de Boussinesq : rappels historiques et valuation directe. *Comptes Rendus Mcanique*, 335(9), 2007.

S. Schmitz and P.K. Jha. Modeling the Wakes of Wind Turbines and Rotorcraft Using the Actuator-Line Method in an OpenFOAM -LES Solver. *69th AHS Forum*, 2015.

R.E. Sheldahl and P.C. Klimas. Aerodynamic Characteristics of Seven Symmetrical Airfoil Sections Through 180-Degree Angle of Attack for Use in Aerodynamic Analysis of Vertical Axis Wind Turbines. Sandia National Laboratories, March 1981. Energy Report.

W. Sheng, R.A. Galbraith, and F.N Coton. A Modified Dynamic Stall Model for Low Mach Numbers. *Journal of Solar Energy Engineering*, 130(3), 2008.

J. Smagorinsky. General Circulation Experiments with the Primitive Equations. *Monthly Weather Review*, 91(3), 1963.

J.N. Sørensen and W.Z. Shen. Numerical Modeling of Wind Turbine Wakes. *Journal of Fluids Engineering*, 124(2), 2002.

J. Strickland. The darrieus turbine - a performance prediction model using multiple streamtube. Sandia National Laboratories, October 1975. Technical Report SAND75-0431.

J.H. Strickland, B.T. Webster, and Nguyen. A Vortex Model of the Darrieus Turbine: An Analytical and Experimental Study. *Journal of Fluids Engineering*, 101(4), 1979.

L.J. Vermeer, J.N. Sorensen, and A. Crespo. Wind Turbine Wake Aerodynamics. *Progress in Aerospace Sciences*, 39(6), 2003.

Z. Yang, H. Igarashi, M. Martin, and H. Hu. An Experimental Investigation on Aerodynamic Hysteresis of a Low-Reynolds Number Airfoil. *46th AIAA Aerospace Sciences Meeting and Exhibit*, 2008.

Appendix A

OpenFOAM and TurbinesFoam

The simulations discussed in this report will be run on OpenFOAM. OpenFOAM stands for Open Source Field Operation And Manipulation. Open FOAM is a C++ library used to create solvers and utilities (Puig et al., 2014). Solvers are designed to solve partial differential equations such as the Navier-Stokes equations for fluid flow, and utilities are used for data manipulation. The software has two distinct environments for pre-processing and post-processing. The overall structure of OpenFOAM is shown in figure A.1.

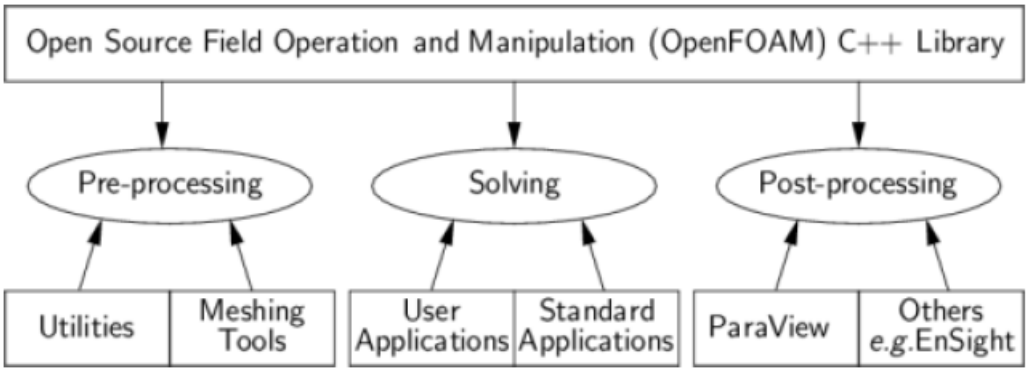

Figure A.1: OpenFOAM structure (OpenFOAM, 2013).

A guide developed by Jordi Casacubertal Puig (Puig et al., 2014) gives a great insight into the workings of the software.

turbinesFOAM is a library created by Bachant et al. (Bachant) for the simulation of vertical and horizontal axis turbines using an ALM approach which uses finite volume discretization. turbinesFoam simulates the wind and marine hydrokinetic turbines in OpenFOAM (2.3.x). The turbinesFoam library structure is quite user friendly. Figure A.2 shows the flowchart of the turbinesFoam library.

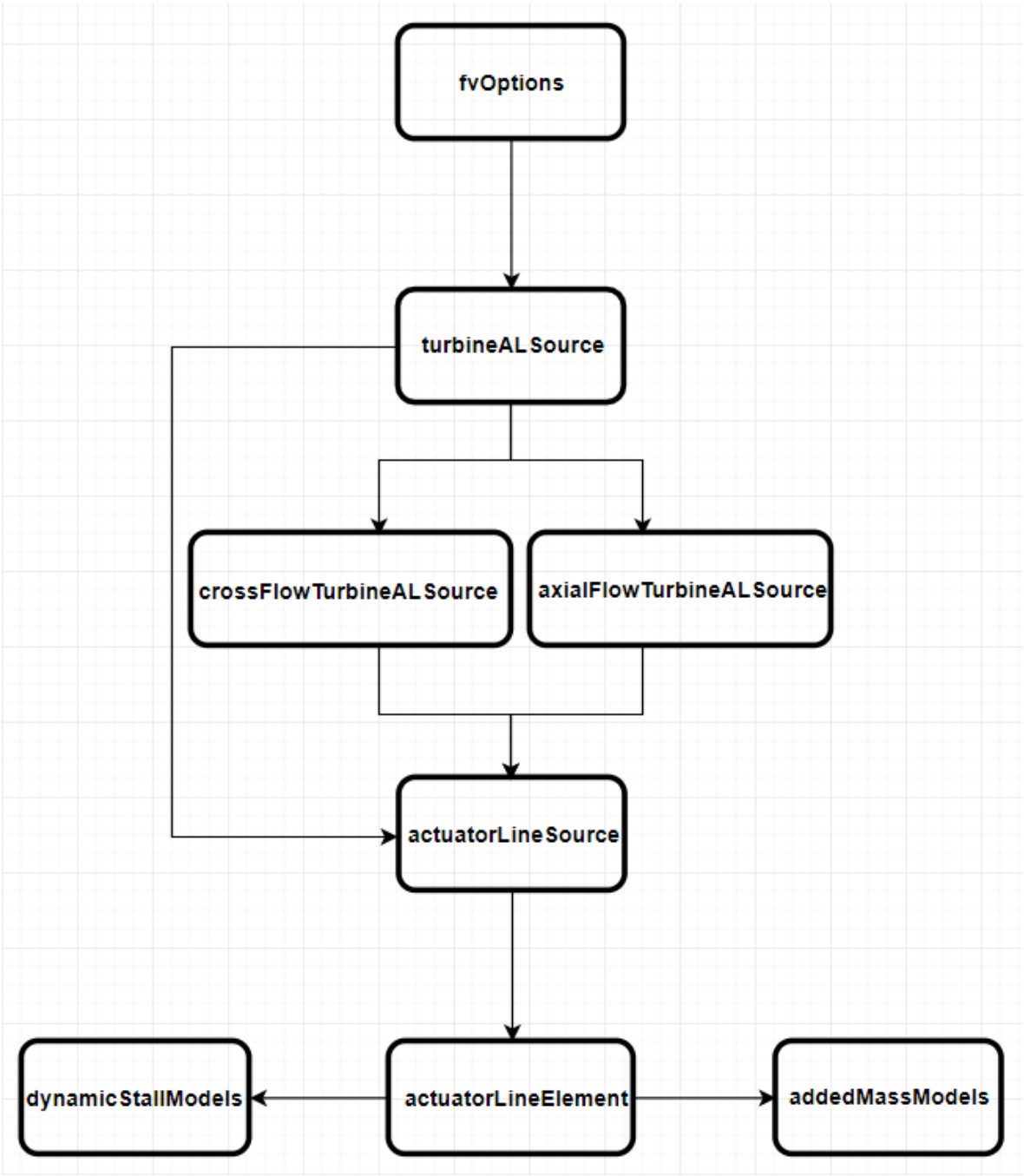

Figure A.2: Flowchart of the turbinesFoam library.

The fvOptions file in the OpenFOAM directory is used to specify the turbine geometry and the dynamic parameters. The input from fvOption is accessed by the turbineALSource files to establish the general turbine parameters, i.e. the tip speed ratio, inflow velocity, turbine axis, corrections, etc. The turbine is then categorised into one of the two types, axial flow turbine or cross flow turbine. The corresponding files (crossFlowTurbineALSource or axi-

alFlowTurbineALSource) establish the rotation matrices for the turbine and breaks down the turbine into various actuator lines. The actuatorLineSource files discretize the actuator lines into actuator elements along the lines. These files can also be run directly and turbinesFoam allows for simulation of individual actuator element, i.e. a blade cross-section. The position data of each actuator line is passed to actuatorLineElement files for computation of the inflow velocities and the projected force. The dynamic effects, flow curvature correction and added mass effect are added here. The data is then passed back upstream for integration.